

American University in Cairo

AUC Knowledge Fountain

Theses and Dissertations

Student Research

Fall 1-1-2022

Influence of Annealing and Compaction on Enhancing the Temperature and Strain Sensitivities of Multi-Walled Carbon Nanotube (MWCNT) Films

Rufaydah Hassan

rufaydah.ahmed@aucegypt.edu

Follow this and additional works at: <https://fount.aucegypt.edu/etds>



Part of the [Engineering Commons](#)

Recommended Citation

APA Citation

Hassan, R. (2022). *Influence of Annealing and Compaction on Enhancing the Temperature and Strain Sensitivities of Multi-Walled Carbon Nanotube (MWCNT) Films* [Master's Thesis, the American University in Cairo]. AUC Knowledge Fountain.

<https://fount.aucegypt.edu/etds/1681>

MLA Citation

Hassan, Rufaydah. *Influence of Annealing and Compaction on Enhancing the Temperature and Strain Sensitivities of Multi-Walled Carbon Nanotube (MWCNT) Films*. 2022. American University in Cairo, Master's Thesis. *AUC Knowledge Fountain*.

<https://fount.aucegypt.edu/etds/1681>

This Master's Thesis is brought to you for free and open access by the Student Research at AUC Knowledge Fountain. It has been accepted for inclusion in Theses and Dissertations by an authorized administrator of AUC Knowledge Fountain. For more information, please contact mark.muehlhaeusler@aucegypt.edu.



THE AMERICAN UNIVERSITY IN CAIRO
SCHOOL OF SCIENCES AND ENGINEERING

Influence of Annealing and Compaction on Enhancing the Temperature and Strain Sensitivities of Multi-Walled Carbon Nanotube (MWCNT) Films

BY

Rufaydah Ahmed Hassan

A thesis submitted in partial fulfillment of the requirements for the degree

of

Master of Science in Mechanical Engineering

Under the supervision of:

Dr. Amal Esawi

Professor, Department of Mechanical Engineering

The American University in Cairo

Dr. Mustafa Arafa

Professor, Department of Mechanical Engineering

The American University in Cairo

August 2021

Keywords

CNT; MWCNTs; strain sensing; buckypaper; strain sensitivity; temperature sensitivity; tunneling effect; piezoresistivity; annealing; compaction; boiling solvents; cyclic loading.

Dedication

This thesis is proudly dedicated to

All my beloved family

Father, Mother, Grandmother, Husband, Rania, Reham, Nouran, Yehia, and the most
precious one Sophia

Thanks for always nourishing me with love, care, and support

Acknowledgments

This thesis has become a reality with the kind support of many people. I would like to thank all of them genuinely.

First and foremost, I am very grateful to God Almighty for always giving me strength. Without his graces and blessings, this work would not have been possible.

I also would like to express my gratitude towards all my understanding family members for being by my side in the most challenging times.

I would like to genuinely thank **Dr. Amal Esawi** for her continuous support, guidance, and following up with me tirelessly. I owe **Dr. Amal** my devotion, attention to detail, and, most importantly, my passion for research and innovation. I am thankful to Dr. Amal for granting me the opportunity of working under her umbrella. I was lucky enough to start my academic journey with such a knowledgeable/visionary professor. This work has never been accomplished without her guidance.

I am always grateful to **Dr. Mustafa Arafa** for his support, professionalism, and helping me through my research journey. I would like to express my gratitude to **Dr. Mustafa** for paying attention to the smallest details and constantly tracking my progress through action plans. I have learned to be consistent and organized through Dr. Mustafa. Completing this work could not have been possible without his expertise, guidance, vision, patience, and mentoring.

A special thank you note for **Dr. Adham Ramadan** for financially supporting all the graduate students, including me, during the tough pandemic time.

I also would like to extend my special thanks to **Ruaa Elnur** for patiently helping me in the fabrication processes.

I would like to thank **Dr. Yassin Rady** for helping me performing the statistical analysis in this study.

I would like to thank my colleagues **Nouran El-Badawi** and **Amr Tayel** for providing me a good research environment while working in the chemistry research lab.

I would like to thank **Mr. Mohamed Hussein** and **Engineer Moataz Hammouda** for always facilitating my work at the vibration measurements lab.

I would like to thank **Engineer Ahmed ElBeltagy** for his professionalism in helping me in the SEM imaging of the samples.

I would like to thank my best friend **Passant Elwy** for always being by my side.

Abstract

Carbon nanotubes (CNTs) possess superior thermal, electrical, and mechanical properties. When CNTs undergo particular fabrication procedures, they transform from a nanoscale form into macroscopic thin sheets referred to as buckypapers (BPs). The main idea behind using BP is to facilitate the handling of CNTs without losing their exceptional properties. Additionally, BPs showed potential for being the used material in strain and temperature applications thanks to their thermal stability, flexibility, high sensitivity, and the ability to conform to any complex structure.

In the current study, the multi-walled carbon nanotube (MWCNT) thin films were prepared using the vacuum filtration technique. Following the fabrication procedure, BPs were subjected to a combination of different treatments involving annealing, exposure to a boiling solvent, and compaction. A series of experimental tests, including loading/unloading, heating/cooling, and combining strain and temperature effects at the same time, were carried out to assess the piezoresistivity as well as the temperature sensitivity of the BP. The morphology of the BPs was examined using Scanning Electron Microscopy (SEM). Moreover, the fracture morphology of the BP was obtained by the tensile stage.

The results indicate that BPs are highly sensitive to temperature and mechanical strain. Moreover, CNT thin films can exhibit a higher sensitivity when subjected to specific treatments, such as annealing and compaction. The improvement was confirmed by the obtained microstructure by SEM and quantified by the obtained empirical gauge factor (GF) values and the temperature coefficient of resistance (TCR) values.

Table of Contents

Chapter 1: Introduction.....	1
1.1 Background and Motivation	1
1.1.1 Strain sensors	2
1.1.2 Temperature Sensors.....	4
1.2 Carbon Nanotubes	5
1.2.1 Electrical Properties	8
1.2.2 CNTs Mechanical Properties	9
1.2.3 CNT Thermal Properties.....	11
1.2.4 CNTs Synthesis Processes	12
1.3 Carbon Nanotubes Thin Films (Buckypaper).....	13
1.3.1 BPs Synthesis Processes	14
1.4 Drawbacks of the existing strain sensors	15
1.5 Why CNT-based sensors?	15
1.6 Objectives.....	17
1.7 Statement of Novelty.....	18
Chapter 2: Literature review	19
2.1 Carbon Nanotube Thin Films	19
2.1.1 Latest Efforts in Preparation the CNT Thin Film and the CNT-based Composites.....	19
2.1.2 Buckypaper Surface Morphology	21
2.2 Buckypaper-based Strain Sensor	22

2.2.1	Testing Setup.....	23
2.2.3	The Tensile Response of Buckypaper.....	27
2.2.4	Previous Efforts to Improve GF.....	28
2.3	BP-based Temperature Sensor	29
2.3.1	Fabrication Technique.....	29
2.3.2	Temperature Sensitivity	32
2.3.3	Resistance Vs. Temperature Relation	33
2.4	Summary of Literature Review	34
Chapter 3: Materials and Experimental Methods		35
3.1	Materials	35
3.1.1	Elicarb CNT Powder.....	35
3.1.2	Isopropyl Alcohol (IPA)	36
3.2	Processing & Fabrication Techniques.....	36
3.2.1	BP Fabrication.....	36
3.2.2	Filtration Process.....	39
3.3	Applied Treatments Before Testing (A, B, and C).....	42
3.3.1	BP Conditioning.....	42
3.3.2	Annealing	43
3.3.3	Exposure to Boiling Solvent	44
3.3.4	Compaction	44
3.4	Characterization.....	46
3.4.1	BP morphology using Scanning Electron Microscopy (SEM)	46
3.4.2	Fracture Morphology Using the Tensile Stage	46

3.5	BP-based Strain Sensor	48
3.5.1	Strain Sensor Testing Setup	48
3.5.2	Strain Calculations	49
3.6	Buckypaper-based Temperature Sensor	51
3.6.1	Temperature Testing Setup	51
3.7	Factors to be studied	52
Chapter 4: Results and Discussion.....		53
4.1	Design-Expert Results.....	53
4.1.1	Half-Normal Plot Results	57
4.2	Buckypaper-based Strain Sensor	59
4.2.1	Loading/Unloading results	59
4.3	Buckypaper-based temperature sensor	62
4.3.1	Heating/Cooling Results	62
4.4	Strain/Temperature combination results.....	65
4.5	SEM Results.....	68
4.6	Tensile Stage Results.....	68
4.6.1	Force-Displacement Graphs.....	68
4.6.2	Quasi-static Loading/Unloading Graphs.....	70
4.6.3	Fracture Morphology	71
Chapter 5: Conclusions and Recommendations		73
5.1	Summary and Conclusions.....	73
5.2	Recommendations	74

References.....	75
APPENDICES.....	89
Appendix A: Graphical representation of GF values.....	89
Appendix B: All loading/unloading graphs.....	94

List of Tables

Table 2.1: Summary of BP different testing setups.	26
Table 2.2: Summary of some of the GF values found in the previous studies.....	29
Table 2.3: Summary of TCR values as found in the previous studies.	33
Table 3.1: Different conditions applied to the BP samples with different levels.	42
Table 3.2: Dimensions of the apparatus components.....	50
Table 4.1: ANOVA model results generated by Design-Expert software.	54
Table 4.2: All numeric gauge factors.	55

List of Figures

Figure 1.1: Schematic diagram of the Wheatstone bridge circuit [1].	2
Figure 1.2: Schematic illustration diagram of the configuration of the resistors in the Wheatstone bridge [2].	3
Figure 1.3: Different types of temperature sensors. (a) Thermostat, (b) Thermistor, (c) RTD, and (d) Thermocouple [4].	5
Figure 1.4: Structure of Carbon Nanotubes. (a) Single-walled Nanotube (SWCNT) and (b) Multi-walled Carbon Nanotubes (MWCNT) [8], [9].	6
Figure 1.5: Research trends in CNT (A) the annually produced patents using CNT. (B-E) different commercial CNT applications [12].	7
Figure 1.6: Schematic illustration of different types of chirality of Carbon Nanotubes [12].	9
Figure 1.7: SEM image of vertically aligned CNTs [28].	10
Figure 1.8: CNT vertical alignment in the Y direction.	11
Figure 1.9: Schematic structure of carbon-carbon covalent bond [34].	12
Figure 1.10: The currently used methods for fabricating CNTs [39].	13
Figure 1.11: Schematic illustration of the fabrication procedure steps of the buckypaper [43].	14
Figure 2.1: BP fabrication techniques. (a) Vacuum filtration method, (b) tape casting [51].	19
Figure 2.2: The morphology of the in-situ cross-linked BP [54].	21

Figure 2.3: AFM analysis of the spray deposited CNT film [64].	22
Figure 2.4: Schematic diagram of bending test setup [67].	23
Figure 2.5: Schematic illustration of the cantilever beam strain testing setup[62].	24
Figure 2.6: Schematic diagram of the bending test setup [68].	25
Figure 2.7: Resistance change as a function of the applied strain [53].	27
Figure 2.8: Schematic diagram of using the four-probe method to measure the resistance of CNTs [73].	30
Figure 2.9: Schematic diagram of BP temperature sensor testing setup [71].	30
Figure 2.10: Schematic illustration represents the spray deposition fabrication technique [64].	31
Figure 2.11: Schematic diagram illustrates CNTs grown on Ni film [74].	31
Figure 2.12: Temperature Vs. resistance relationship in heating/cooling process [57].	33
Figure 2.13: Resistance change as a function in temperature [64].	34
Figure 3.1: As received dry powder form of Elicarb MWCNTs supplied by Thomas Swan [79].	36
Figure 3.2: The magnetic stirrer used for sample dispersion; image was taken at AUC chemistry lab.	38

Figure 3.3: The sonication process. (a) The sonication bath after placing the two samples was divided into four beakers and (b) The sonication bath prior to placing the ice and the samples. The images were taken at AUC chemistry research lab.	39
Figure 3.4: The vacuum filtration setup. (a) The experimental setup at AUC chemistry research lab, (b) a schematic illustration of the filtration process.....	40
Figure 3.5: Summary of the fabrication processes. (a) Schematic representation of the buckypaper fabrication procedure and (b) The BP sensor after preparation step and prior to testing.	41
Figure 3.6: The used boiling setup. The image was taken at AUC chemistry research lab.....	44
Figure 3.8: A universal testing machine used for compacting CNT samples. The image was taken at AUC materials testing lab.	45
Figure 3.8: Tensile stage external view [90].....	47
Figure 3.9: SEM using tensile stage setup. (a) the prepared CNT tensile specimen prior to testing and (b) The sample fixation inside the tensile stage.....	48
Figure 3.10: Strain sensor testing setup (a) schematic representation of the setup and (b) the actual testing setup captured at AUC vibration lab.	49
Figure 3.11: Schematic illustration for the cantilever beam.	51

Figure 3.12: Temperature sensor testing setup (a) schematic representation of the setup and (b) the actual testing setup captured at AUC vibration lab.	50
Figure 4.1: Design expert half-normal probability graph result.	58
Figure 4.2: Cyclic loading of BP-based strain sensor. Three loading/unloading cycles of (a) control sample and (b) A100, C10. The experiment was carried out on a plastic beam.	61
Figure 4.3: Thermal Cyclic of BP. Red lines represent the heating and blue lines represent the cooling. (a) Control sample (A0, C0) and (b) (A100, C10).....	64
Figure 4.4: Effect of cyclic loading at different temperature points going up from room temperature up to 80°C. (a) represents (A0, C0) and (b) represents (A100, C10). The test was done on a stainless-steel beam. The Solid line represents the loading cycle, and the dotted line represents the unloading cycle.	66
Figure 4.5: Effect of thermal cycling on BP-based temperature sensor with adding constant loads: 25g, 50g, and 75g. (a) the control sample (A0, C0) and (b) the treated sample (A100, C10).....	67
Figure 4.6: BP morphology using SEM. (a) (A0, C0) at 20 KX magnification scale, (b) (A100, C10).....	68
Figure 4.7: The force-displacement graphs generated from the tensile stage software plot of (a) (A0, C0) and (b) (A100, C10).....	69

Figure 4.8: Cyclic loading - 5 loading/unloading cycles of the control sample. 70

Figure 4.9: Fracture morphology of the control sample and the treated sample. (a) A0, C0 at 5 kX magnification scale, (b) A100, C10, (c) A0, C0 at higher magnification scale, and (d) A100, C10. 72

ACRONYMS

SHM	Structural Health Monitoring
CNT	Carbon Nanotube
SWCNT	Single-walled Carbon Nanotube
MWCNT	Multi-walled Carbon Nanotube
BP	Buckypaper
DMF	Dimethylformamide
VA-CNT	Vertically Aligned Carbon Nanotube
PMMA	Polymethyl Methacrylate
SDS	Sodium Dodecyl Sulfate
IPA	Isopropyl Alcohol
CVD	Chemical Vapor Deposition
Ag	Silver
PP	Polypropylene
GFRP	Glass Fiber Reinforced Polymer
ATM	Atmospheric pressure
FESEM	Field Emission Scanning Electron Microscopy
SEM	Scanning Electron Microscopy
FCCVD	Floating Catalytic Chemical Vapor Deposition
VER	Vinyl Ester Resin
AFM	Atomic Force Microscopy
ASTM	American Society for Testing and Materials
PVC	Polyvinyl Chloride
TGA	Thermogravimetric Analysis

ACRONYMS

Si	Silicon
Ni	Nickel
GF	Gauge Factor
TCR	Temperature Coefficient of Resistance
WD	Working Distance
A	Annealing
B	Boiling
C	Compaction

NOMENCLATURE

E	Young's modulus
(n,m)	Chirality indices
ε	Strain
R_1	Ratio arm
R_2	Ratio arm
R_3	Standard known resistance
R_4	Variable resistance
R_o	Initial resistance
L_o	Initial length
V_o	Output voltage
V	Excitation voltage

NOMENCLATURE

σ	Bending stress
M	Bending moment
Y	Thickness of the beam
I	Moment of Inertia
L	Length of the BP sample
W	Width of the BP sample
H	Thickness of the BP sample
ℓ	Length of the beam
h_p	Depth of the plastic beam
h_s	Depth of the stainless-steel beam
b_p	Width of the plastic beam
b_s	Width of the stainless-steel beam

CHAPTER 1: INTRODUCTION

This thesis investigates the use of carbon nanotubes (CNTs) as strain and temperature sensors. Therefore, studies on the piezoresistivity of the CNTs were conducted by applying loading/unloading cycles. Moreover, another series of thermal experiments were made to assess the change induced in the CNTs resistance in response to the change in temperature.

This Chapter provides an overview of the requirements of strain and temperature sensors and introduces the use of carbon nanotubes owing to their superior capabilities in this context. The Chapter presents some of the essential terms and will subsequently provide the objective of the study, followed by the scope of work and statement of novelty.

1.1 Background and Motivation

Nanomaterials are materials with at least one dimension less than 100 nm. They have drawn significant attention owing to their exceptional properties, including mechanical, electrical, and thermal properties, compared to their bulk-form materials. One of the main advantages of nanomaterials is the ability to tailor them according to the desired application requirements.

Nanomaterials can be used in various industries. However, some challenges are still encountered with these materials, such as inhalation exposure and waste management issues. Besides, CNTs cannot be adequately handled in the nanoscale, requiring sophisticated fabrication techniques to transform them into the macroscale.

Another challenge that can be addressed with transformation to the macroscale is maintaining the outstanding properties of the CNTs. Furthermore, the behavior of nanomaterials under environmental conditions is still debatable.

1.1.1 Strain sensors

Strain sensors are sensors that convert an imposed strain into a measurable quantity, such as a change in electrical resistance [1]. A common application for strain sensors is structural health monitoring (SHM). Strain sensors can be piezoelectric, capacitive, or piezoresistive. Piezoresistive strain gauges are the most used type.

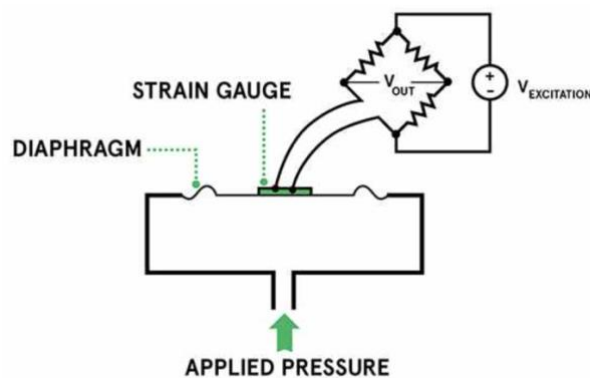


Figure 1.1: Schematic diagram of the Wheatstone bridge circuit [1].

A Wheatstone bridge circuit converts the small changes in resistance into an output voltage. As illustrated in Figure 1.1, the basic working principle of the Wheatstone bridge is providing the bridge with an excitation voltage when there is no applied strain. Furthermore, all the resistors must be balanced, as described in Figure 1.2.

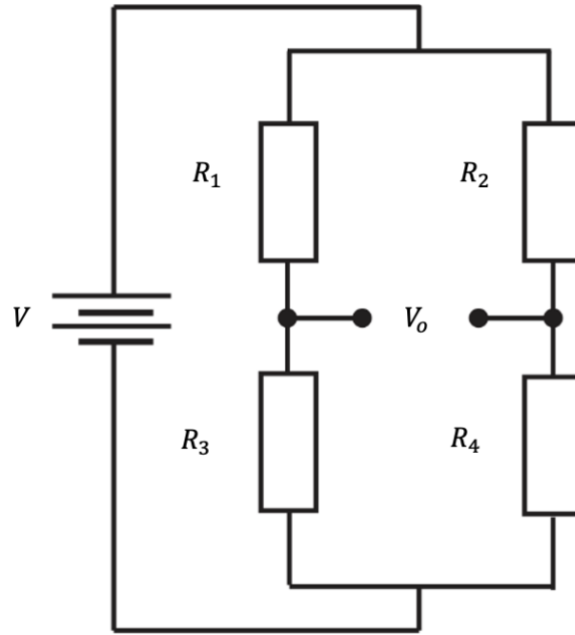


Figure 1.2: Schematic illustration diagram of the configuration of the resistors in the Wheatstone bridge [2].

The output voltage is given by:

$$V_o = \frac{R_3}{R_3 + R_4} - \frac{R_2}{R_1 + R_2} V \quad (1.1) [2]$$

Where:

V_o : The output voltage.

V : The excitation voltage.

R_1, R_2 : Ratio arms.

R_3 : Standard known resistance.

R_4 : Variable resistance.

Gauge Factor

The sensitivity of a strain sensor is termed the gauge factor (GF) and expressed as:

$$GF = \frac{\Delta R/R_0}{\Delta L/L_0} \quad (1.2) [3]$$

Where:

ΔR : change in resistance

R_0 : initial resistance

ΔL : change in length

L_0 : initial length

Strain sensors with higher sensitivities are especially useful in applications involving the detection of smaller strain values. As the typical GF of a conventional foil-type strain gauge is around 2.0 [4], this has spurred research interests into ways of increasing the GF of novel types of strain sensors.

1.1.2 Temperature Sensors

Temperature sensors are devices that are designed to provide readable information about the temperature of an object. One of the common working principles of a temperature sensor is creating a voltage drop across the terminals of a diode [5]. Temperature sensors are divided into two types: contact temperature sensors and non-contact temperature sensors. The first type must be in direct contact with the object that is being measured. The latter is more common and does not need contact with the measured object.

Figure 1.3 describes the main types of non-contact temperature sensors: thermostat, thermistors, resistive temperature detectors (RTD), and thermocouples [6]. The instability, self-heating, and low sensitivity of the current temperature sensors were the urge behind exploring the capability of thermally conductive nanomaterials acting as temperature sensors. Hence, CNTs were a good candidate for such an application.

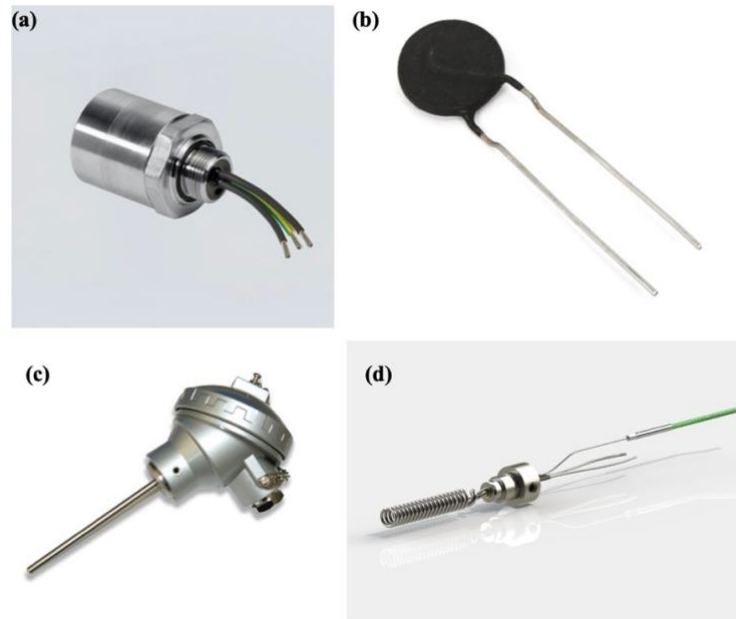


Figure 1.3: Different types of temperature sensors. (a) Thermostat, (b) Thermistor, (c) RTD, and (d) Thermocouple [6].

1.2 Carbon Nanotubes

Carbon nanotubes (CNTs) were discovered in 1991 by Iijima [7]. The structure of the CNT is a seamless tube with lattices in the shape of a hexagonal honeycomb. CNTs are one-dimensional materials with diameters on the nanoscale and can be as small as 1 nanometer (nm) [8]. They have drawn massive attention thanks to their unique mechanical, electrical, and thermal properties [9].

There are two types of CNTs: single-walled carbon nanotubes (SWCNTs) and multi-walled carbon nanotubes (MWCNTs). The significant difference between the different types of CNTs is the layering of the tube as well as the diameter. SWCNT is a rolled single layer of graphene with a diameter of roughly 0.8 nm, as shown in Figure 1.4 (a). On the other hand, MWCNT consists of concentric tubes of graphene stacked together with an average diameter ranging from 10 to 30 nm, as shown in Figure 1.4 (b).

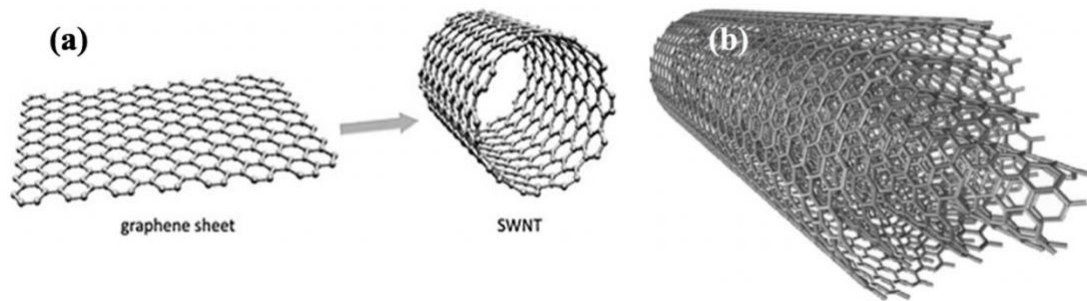


Figure 1.4: Structure of Carbon Nanotubes. (a) Single-walled Nanotube (SWCNT) and (b) Multi-walled Carbon Nanotubes (MWCNT) [10], [11].

CNTs can exist in three forms: armchair, zigzag, and chiral, as illustrated in section 1.2.1 [12]. However, MWCNTs exist in more complex structures, which are Russian dolls and parchment dolls. The first form is when a larger outer tube has one or smaller tubes inside it. The inner cylinder possesses a smaller diameter than the outer nanotube. Whereas the second type of MWCNTs is formed when a single graphene layer is wrapped around itself several times [13]. CNTs exhibit extraordinary mechanical, electrical, transport, and thermal properties due to their unique structure, making them a great candidate in many applications.

Figure 1.5 shows the CNTs applications that are ranging from the automotive industry, water filtration, rechargeable batteries, biomedical applications, sports goods, coatings, and electronics [14]

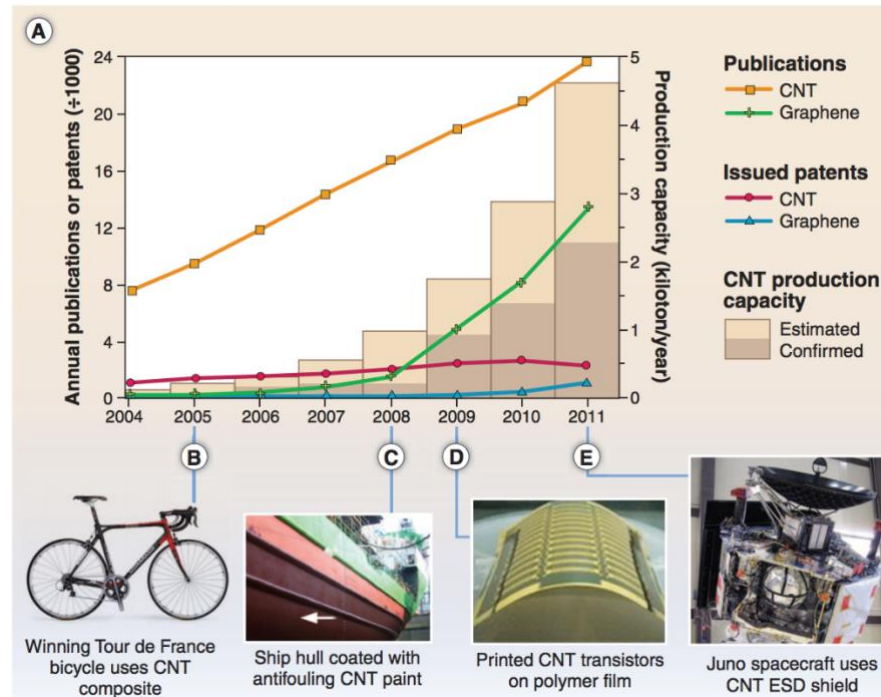


Figure 1.5: Research trends in CNT (A) the annually produced patents using CNT. (B-E) different commercial CNT applications [14].

1.2.1 Electrical Properties

CNTs exhibit superior electrical properties compared to conventional materials, making them a great candidate in various electrical applications [15]. The electronic behavior of CNTs, whether semiconducting, conducting, or metallic behavior, is highly dependent on chirality. The way of rolling up the graphene determines the chirality type.

The chirality of CNTs is governed by two chiral indices, which are (n,m) , and classified into three types: zigzag, armchair, and chiral.

As shown in Figure 1.6, when $n = m$, the CNTs have an armchair structure, indicating that they always exhibit metallic behavior. Moreover, if the chiral index $m = 0$, then the structure will be a zigzag. Furthermore, any other configuration will be referred to as chiral where $n \neq m$ [15]. According to Qiu *et al.* [16], the electronic behavior of the zigzag and chiral structure is either metallic or semiconducting.

According to Dai *et al.* [15][16], the electrical properties of CNTs are a function of the arrangement of graphene. The study also showed that the electrical conductivity of CNTs could exceed the electrical conductivity of copper by 1000 times.

The CNT behavior is determined by dividing $(2n+m)/3$. If the result is an integer, then it will behave like a metal. Otherwise, it will behave like a semiconducting material.

It was reported that the electronic behavior of the CNTs is strongly attributed to the diameter, graphitic rings, chirality, and geometric structure of the tube.

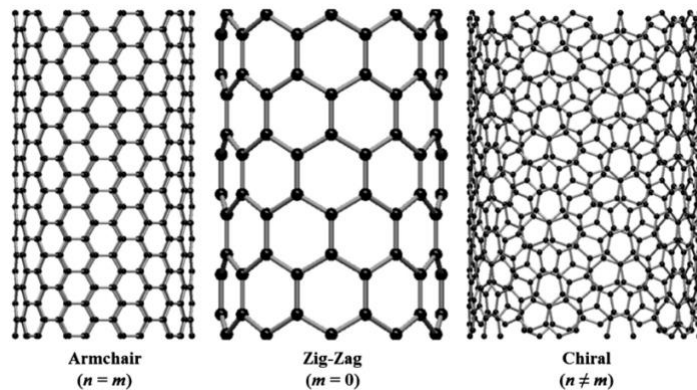


Figure 1.6: Schematic illustration of different types of chirality of Carbon Nanotubes [12].

1.2.2 CNTs Mechanical Properties

Carbon nanotubes are among the stiffest and strongest available materials. Kim *et al.* reported that the tensile strength of CNTs could reach up to 60 GPa. The strength of CNTs is owing to the existing covalent bonds, (C-C)- sp^2 , between carbon atoms [19]. Various techniques were introduced for aligning CNTs, for instance, mechanical stretching, compression, magnetic field, fracture, and uniaxial pressure. Kim *et al.* [20] reported that the young's modulus of CNTs could reach up to 1 TPa.

After deformation, the CNTs original shape can be easily recovered. In the results obtained by Yu *et al.* [21], MWCNTs possess a compressive strength of 100 GPa, and a tensile strength varies between (10 GPa - 60 GPa). In addition to that, Wong *et al.* reported that MWCNTs have a bending strength of 14.2 GPa [22].

CNTs self-assemble in the form of bundles making their properties difficult to be experimentally measured. Based on that, various theoretical and numerical approaches were adopted to quantify the mechanical properties accurately [23].

These approaches include density functional theory (DFT), molecular dynamics (MD), and molecular mechanics [24]–[26]. The exceptional mechanical properties of CNTs are making them an ideal material for many applications that combine eco-friendly, lightweight, and flexibility [27].

According to Pötschke *et al.*, the mechanical behavior of CNT forests is highly attributed to the alignment of the tubes [28], as illustrated in Figure 1.7. In other words, the more the tubes are aligned and unidirectional, the higher the young's modulus and the overall mechanical strength. Likewise, the study carried out by Iakoubovskii *et al.* [29] showed that CNTs superior properties and, accordingly, their functionality requires growing CNT tubes in specific directions.

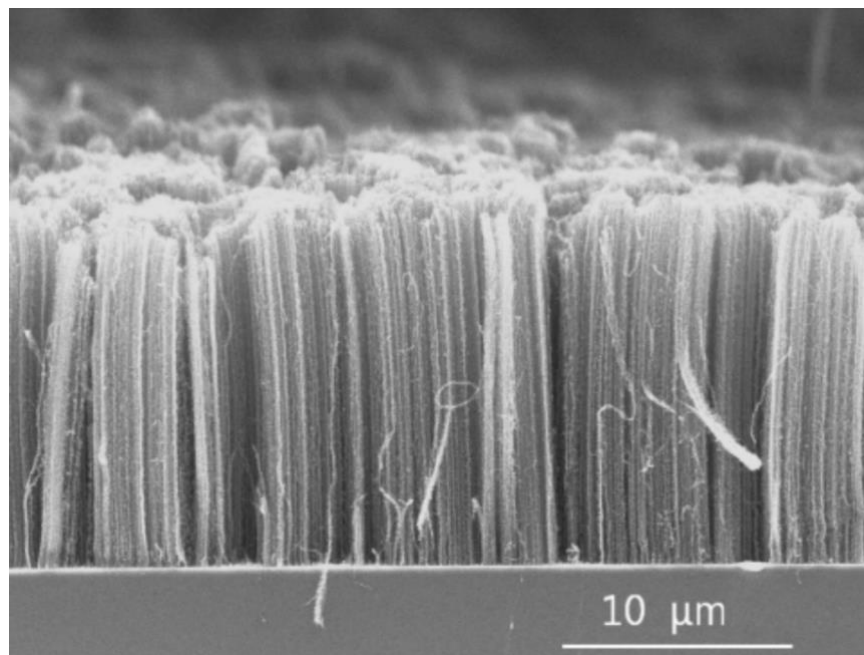


Figure 1.7: SEM image of vertically aligned CNTs [30].

Similarly, Santos *et al.* reported that vertically aligned carbon nanotubes (VA-CNT), as shown in Figure 1.8, exhibit higher GF values when used as strain sensors. [31]

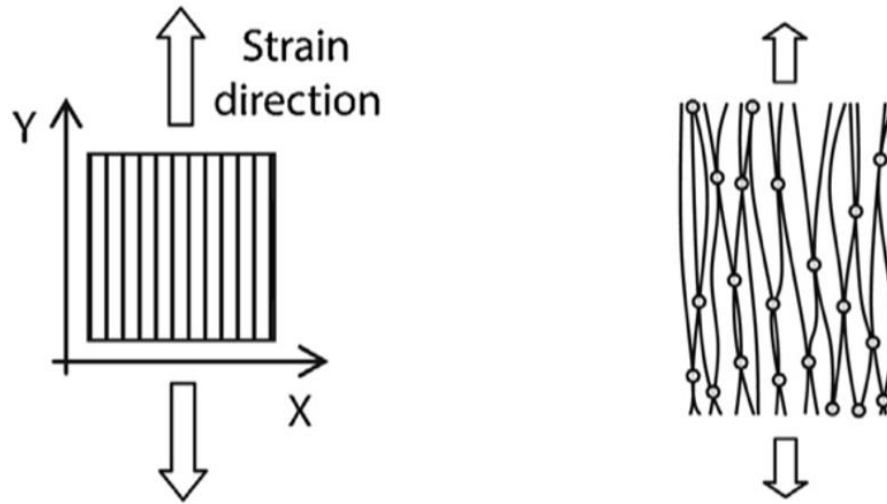


Figure 1.8: CNT vertical alignment in the Y direction.

1.2.3 CNT Thermal Properties

CNTs possess outstanding thermal properties besides electrical and mechanical properties. The thermal conductivity of CNTs is influenced by some factors, such as the CNT density, structural defects, ordering of CNTs networks, and their alignment [32]. Hone *et al.* reported that CNTs display the highest thermal conductivity among different materials [33]. The thermal conductivity of carbon nanotubes can reach up to 6600 W / mK at room temperature [18], [34].

According to Wang *et al.* [32], The large free path of the valence electrons and the carbon-carbon covalent bond between the carbon atoms give rise to the CNTs thermal properties, as shown in Figure 1.9 [35]. Moreover, the superior exceptional thermal properties contribute to their high potential in several thermal applications.

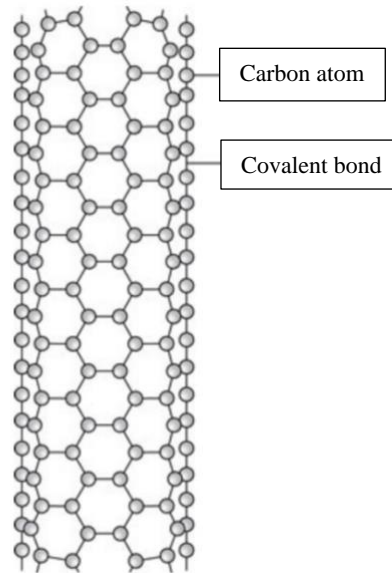


Figure 1.9: Schematic structure of carbon-carbon covalent bond [36].

1.2.4 CNTs Synthesis Processes

Figure 1.10 demonstrates the synthesis techniques used to produce CNTs. The most common fabrication process to produce CNTs is chemical vapor deposition (CVD) [37], [38]. However, several other processes are being used, such as arc discharge deposition [39] and laser-ablation technique [40].

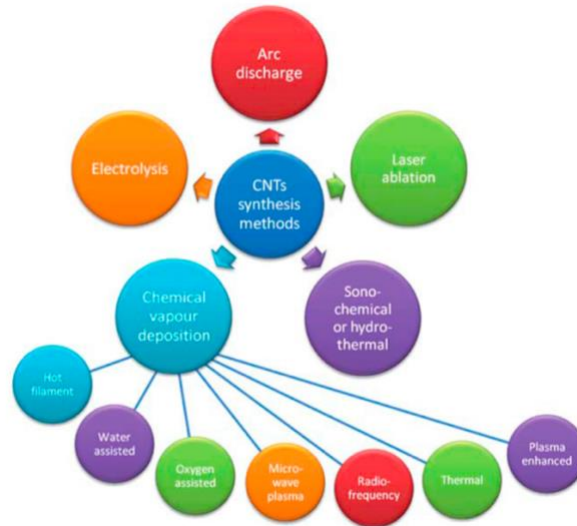


Figure 1.10: The currently used methods for fabricating CNTs [41].

1.3 Carbon Nanotubes Thin Films (Buckypaper)

CNTs are termed buckypaper when fabricated in the form of a macroscopic thin sheet-like material. Being on the macroscale makes the handling process of CNTs easier than a powder form [42]. Buckypaper combines the lightweight as well as the strength. The carbon-carbon covalent bond is the main cause behind the strength of the BP [43]. Furthermore, when BPs are stacked together, they become efficient in several applications such as fire protection, electrical conduction, and thermal conduction [44].

1.3.1 BPs Synthesis Processes

Many studies showed that the buckypaper is typically synthesized by the vacuum filtration technique, as shown in Figure 1.11 where the CNTs powder is dispersed into a solvent. The BP then is passing through sonication, stirring, filtration levels, then it is dried. The BP has a low thickness, in general, less than 50 microns (15).

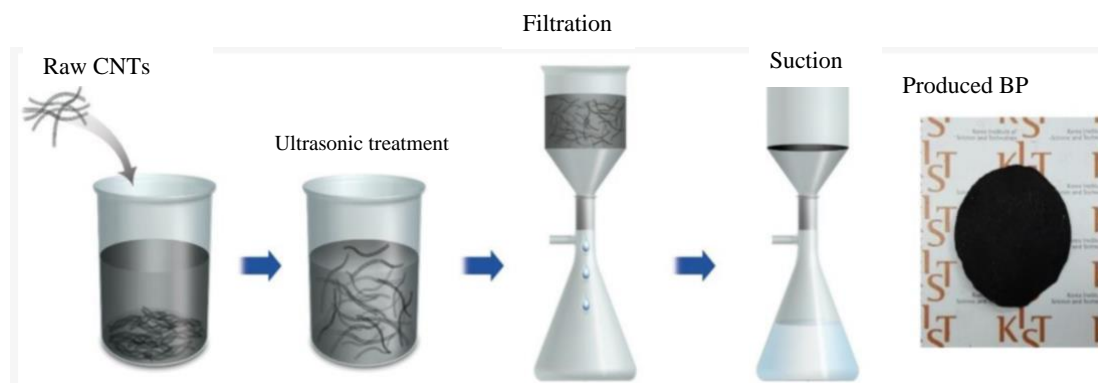


Figure 1.11: Schematic illustration of the fabrication procedure steps of the buckypaper [45].

Two types of CNTs were employed in fabricating the buckypaper: single-walled carbon nanotubes (SWCNTs) and multi-walled carbon nanotubes (MWCNTs). However, the latter is preferred and commonly used. This selection is due to the economic cost, high purity, and exhibition to higher electrical and chirality properties of MWCNTs over SWCNTs [9]

1.4 Drawbacks of the existing strain sensors

As mentioned earlier in section 1.1.1, a conventional metallic strain gauge is widely used due to ease of installation and handling [46]. Strain gauges are isotropic materials where they exhibit the same properties in all strain directions, whether longitudinal or transverse, which is an advantage over CNTs whose electrical resistance changes according to the strain direction. However, there are some drawbacks associated with the current strain sensors.

The conventional strain sensors have a limited sensitivity translating into a GF of around 2.0 [10]. Besides, the use of the existing strain sensors is discouraged due to thermal instability [47]. Furthermore, conventional strain sensors have limited stretchability, which is below 5% compared to CNTs whose strain to failure can reach up to 1380% [48]. However, CNTs at higher strains, above $1000 \mu\epsilon$, can be permanently deformed [49]. Consequently, they cannot fit in some applications.

1.5 Why CNT-based sensors?

CNT-based strain/temperature sensors are attractive candidate sensors because of their high sensitivity, relatively low cost, low power consumption, ease of conformation to any structure shape, and the ability to provide a wide range of strain/temperature sensitivities. Furthermore, a key factor behind using the CNTs is their ability to be tailored for any desired application.

When it comes to strain sensing application, piezoresistivity is an important terminology to acquire. Piezoresistivity is the change in electrical resistivity in response to applied mechanical strain [50]. Some factors influence the piezoresistive behavior of the CNT-based strain sensor, whether it is linear or nonlinear.

These factors are as follows:

- The CNTs are incorporated into a matrix.
- The amount of the subjected strain.
- The volume fraction of the nanotubes in the case of composite [10], [46].
- The CNT morphology [10].
- The CNT aspect ratio.
- The fabrication technique.

The CNT-based sensors have a stable resistance, high sensitivity, and good ability to be mounted on any surface [31],[51], which can be a key point for selection in many applications.

Many attempts have been made by researchers to enhance the BP properties. Packing density is believed to have a major influence on the BP properties. In other words, the less porous the BP structure, the higher properties it can exhibit, including mechanical strength, flexibility, electrical, and thermal conductivities. One of the adopted methods was adding metallic nanoparticles to the CNT thin film. This approach was successful in improving the BP properties, such as the mechanical strength. However, it increases the mass density of the BP from 0.45 g/cm^3 to 0.68 g/cm^3 . Therefore, other efforts have been made to enhance the BP sensitivities without losing the lightweight feature. Some researchers applied a compaction treatment to the BP. But the improvement in the GF was minimal. Moreover, others

suggested using the pressurized filtration technique, and this was useful in improving the GF by 1.9%. However, this solution needs more energy and, accordingly, higher cost. Various treatments, such as annealing (A), exposure to boiling solvent (B), and compaction (C), are believed to improve the properties of the BP. In the present study, a combination of the three treatments (A, B, and C) was applied to the samples and then investigated through Design-Expert software to investigate their influence on the sensitivity.

1.6 Objectives

The objectives of the thesis can be summarized as follows:

- Fabricate a buckypaper sensor from Elicarb MWCNT bucky powder using the vacuum filtration technique.
- Apply a combination of treatments to the produced buckypaper, such as annealing, exposure to a boiling solvent, and compaction to enhance its performance.
- Develop an experimental approach to assess the influential factors on BP sensitivity.
- Explore a preliminary understanding of the temperature significance on the change in the electrical resistance of the BP.
- Develop a good understanding of the thermal and piezoresistive behavior of the BP through explaining the variation of the electrical resistance in response to load, or temperature, or a combination of both factors.

1.7 Statement of Novelty

A combination of treatments, namely annealing, exposure to a boiling solvent, and compaction, was applied to the fabricated sensor to maximize the strain/temperature sensitivities. Furthermore, a series of experiments was done for all combinations to investigate the most influential treatments. Additionally, investigating the change in the resistance of the BP when subjected to mechanical strain and temperature at the same time was conducted.

Moreover, exposing CNTs to boiling solvent has been previously studied to densify CNT forests and enhance their properties, but it was never employed to enhance the electrical/thermal conductivity of BPs. So, using the boiling solvent to enhance the conductivity is considered a novel approach.

CHAPTER 2: LITERATURE REVIEW

CNTs have been previously investigated in the literature in the past thirty years. This chapter will review current literature in terms of properties, preparation, strain sensitivity, and temperature sensitivity.

2.1 Carbon Nanotube Thin Films

2.1.1 Latest Efforts in the Preparation of the CNT Thin Film and the CNT-based Composites

One of the main obstacles that hinder the use of CNT in enormous applications is the handling process. Accordingly, the main objective behind the various buckypaper preparation techniques is to ease the handling process by translating it from a nanoscale into a macroscopic scale [52].

Buckypaper preparation is typically produced by deposition techniques such as membrane filtration, casting techniques, as shown in Figure 2.1 [53][54].

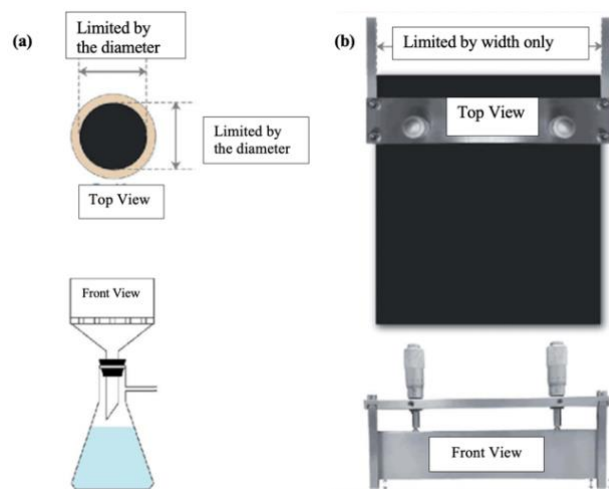


Figure 2.1: BP fabrication techniques. (a) Vacuum filtration method, (b) tape casting [55].

According to [2, 3], the CNT films were prepared using hot filament chemical vapor deposition. Besides, Kang *et al.* prepared the SWNT films by dispersing the SWNT into a solvent, Dimethylformamide (DMF), followed by a sonication bath and filtration. The buckypaper was then subjected to annealing [46].

It has been observed that annealing enhances the electrical properties by removing the contaminants as well as recovering the wall defects of the produced CNT film [46]. Meanwhile, Rein *et al.* prepared the BP film by dispersing the CNT in a solvent followed by successive filtration processes [56]. Similarly, Yong *et al.* followed the same preparation procedure [57]. Zhang *et al.* proposed an in situ cross-linking technique for MWCNT by dispersing the CNT in benzoquinone to improve the mechanical behavior of the buckypaper [58].

According to Pop *et al.* [16], MWCNT was added in a vinyl ester, a thermosetting polymer with a brittle behavior, polypropylene (PP), and thermoplastic polymer with a tough behavior. It was reported that using MWCNT as a filler will enhance the piezoresistive properties [59]. In the meantime, Miao *et al.* showed that subjecting buckypaper to in-plane strain results in improved piezoresistive properties than embedding CNT in composites [60]. Wang *et al.* prepared the buckypaper strain sensor by spray vacuum filtration technique. Then, the CNT was embedded into a glass fiber reinforced polymer (GFRP) [61].

Arif *et al.* studied buckypaper preparation by applying a compressive force to the conventional vacuum filtration method [62]. On the other hand, the mechanical properties of the BP was enhanced by Zhang *et al.* through applying a high pressure up to 12 atm to the conventional vacuum filtration method [63].

Shukrullah *et al.* synthesized the buckypaper using the floating catalytic chemical vapor deposition (FCCVD) method [64]. Li *et al.* synthesized the MWCNT thin films through the chlorine-assist low-pressure method [65].

2.1.2 Buckypaper Surface Morphology

Her *et al.* investigated the buckypaper morphology using field emission scanning electron microscopy (FESEM). The BP samples were coated prior to imaging [66]. It was found that the MWCNTs became tighter as the aspect ratio increases, which are highly desired in properties and applications [67].

Furthermore, Zhang *et al.* analyzed the microstructure of the in-situ cross-linked BP using scanning electron microscopy (SEM), as shown in Figure 2.2, The authors revealed that cross-linking enhances the BP properties [58]. Similarly, Wang *et al.* detected the uniformity of the buckypaper distribution using SEM [61].

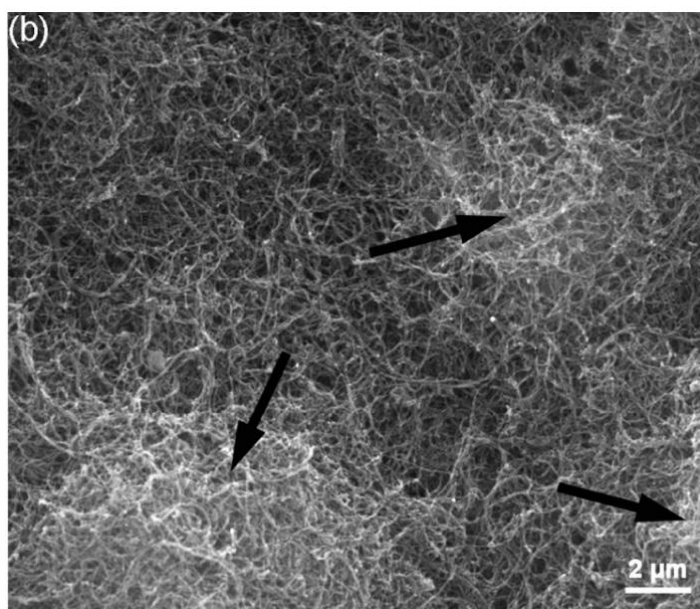


Figure 2.2: The morphology of the in-situ cross-linked BP [58].

Cagatay *et al.* developed CNT film with high uniformity using the spray deposition method, as shown in Figure 2.3. The atomic force microscopy (AFM) revealed that the deposited buckypaper does not contain bundles [68]. Furthermore, Wang *et al.* checked the MWCNT orientation and pore size diameter using FESEM imaging [69]. Similarly, Zhang *et al.* used the same approach to investigate the surface morphology [70].

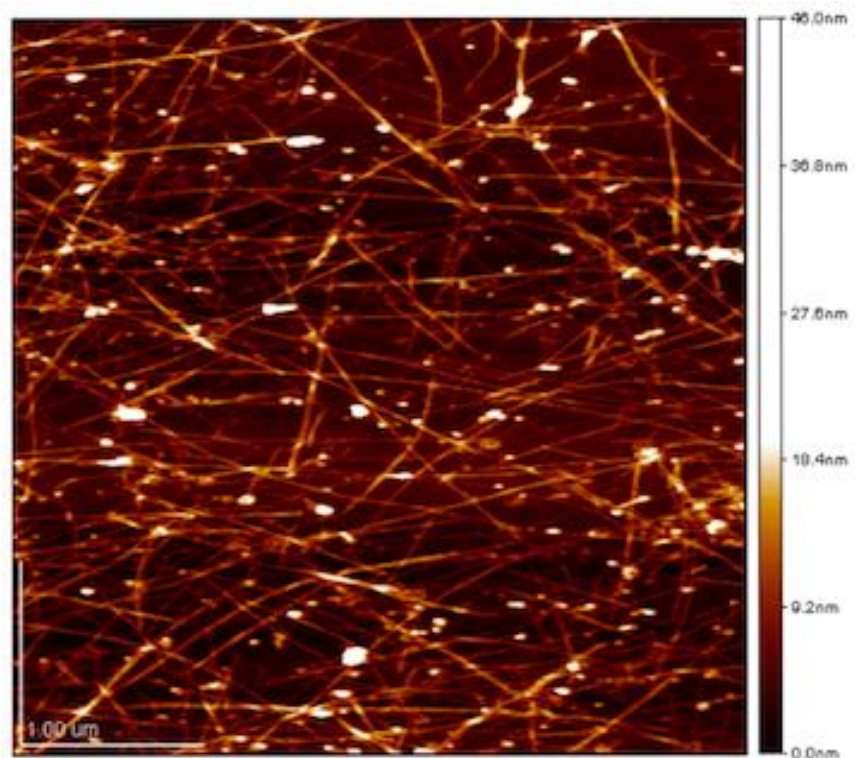


Figure 2.3: AFM analysis of the spray deposited CNT film [68].

2.2 Buckypaper-based Strain Sensor

In this subsection, some of the previous findings regarding the BP-based strain sensor will be reviewed. The testing setup will be reviewed in 2.2.1, the tensile response in 2.2.2, and some of the GF values in the literature will be discussed in 2.3.

2.2.1 Testing Setup

Kang *et al.* performed a strain sensing setup by attaching the buckypaper strain sensor onto a fiberglass cantilever beam. The sample was glued on the substrate with super glue to avoid slippage and ensure strain transfer [46].

A silver epoxy was used to connect the wires to the sensors. Rein *et al.* proposed incorporating the buckypaper strain sensor in the center of a dog-bone-shaped epoxy sample to enhance the homogeneity of the deformation under the tensile tests.

Furthermore, a silver paint was used to adhere the electrodes to the sample the copper electrodes were connected to the sensor through [56]. In the same way, Karimov *et al.* installed the strain sensor on a beam using a silver paste, as shown in Figure 2.4 [71].

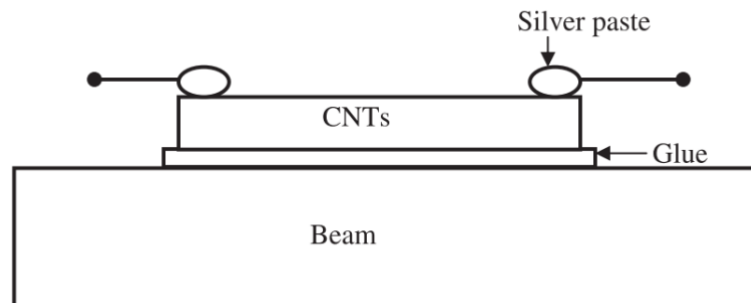


Figure 2.4: Schematic diagram of bending test setup [71].

In the work investigated by [57], the buckypaper sensor was placed on the glass fiber reinforced composite center. Moreover, Wang *et al.* cut the buckypaper sensor into a rectangular sample and fixed it on glass fiber reinforced composite using silver conductive adhesive. The silver adhesive was used to ensure the bonding between the sensor and the matrix. The applied strain was measured using a fiber

Bragg grating sensor [69]. Arif *et al.* used the four-point probe contact method to measure electrical sensitivity [62]. In work conducted by Sanli *et al.*, the BP strain sensor was fixed on a cantilever beam, as shown in Figure 2.5. A cyclic tensile/compressive loading was used to deform the beam [66].

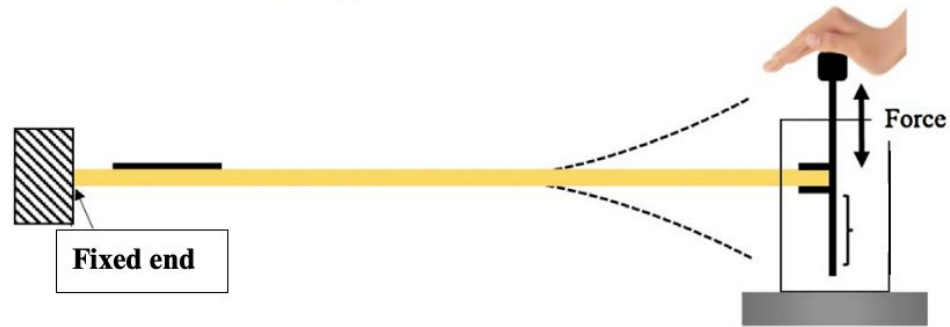


Figure 2.5: Schematic illustration of the cantilever beam strain testing setup[66].

Furthermore, Her *et al.* cut the BP strain sensor into a rectangular cross-section and mounted it on the center of the aluminum (Al) beam. The samples were adhered to the beam using silver electrodes. A speed of 5 mm/min was used through performing the four-point bending test [52].

Miao *et al.* investigated the piezoresistive response of BP by cutting the specimens into rectangular cross-sections. Afterwards, they were subjected to an in-plane longitudinal tensile strain using Instron 1122 (Instron Inc, Canada). The electrical resistance was measured using a multimeter [60].

Vemuru *et al.* attached the BP strain sensor onto a brass beam using silver epoxy as an adhesive. The sample was subjected to a uniaxial tensile loading with the aid of the universal testing machine (UTM), and the electrical resistance was measured through using a multimeter[51].

As shown in Figure 2.6, Dharap *et al.* mounted the BP strain sensor onto a brass beam, and an insulating polyvinyl chloride (PVC) film was used to ensure the strain transfer [72].

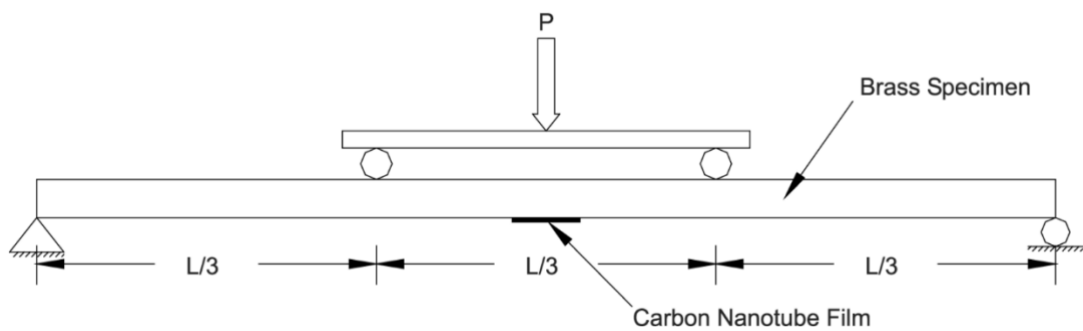


Figure 2.6: Schematic diagram of the bending test setup [72].

Table 2.1 summarized the available testing setups in the current study, which was mentioned earlier in the sub-section 2.2.1.

Table 2.1: Summary of BP different testing setups.

Sensing Material	Testing setup	References
MWCNT thin film	BP was adhered to a fiberglass cantilever beam	[46]
MWCNT thin film	BP was mounted onto an epoxy matrix	[56]
MWCNT thin film	BP was fixed on an elastic beam using silver paste	[71].
MWCNT thin film	BP was mounted onto a brass beam using epoxy as the adhesion material	[51]
SWCNT thin film	BP was attached to a brass beam	[72]

2.2.2 The Tensile Response of Buckypaper

Many of the existing studies showed that the buckypaper strain sensor has a significant resistance change to the strain change. The observed resistance behavior increases with the tensile loading and decreases with the compressive loading. According to Shanov *et al.* [46], the resistance increases linearly as the strain increases.

In accordance with the previous study, Wang *et al.* investigated the BP piezoresistive behavior and reported that the resistance increases linearly with the strain [69]. On the other hand, Rein *et al.* reported that the BP strain sensor does not behave linearly.

This behavior can be attributed to the tunneling resistance between the CNT inter-particle displacement, which is known to behave exponentially. However, the data could be approximated in a linear pattern [56]. Similarly, Yong *et al.* [57] demonstrated the resistance change in a linear behavior to the strain and reported that the resistance increases as the tensile loading increases and decreases with the compressive loading, as shown in Figure 2.7.

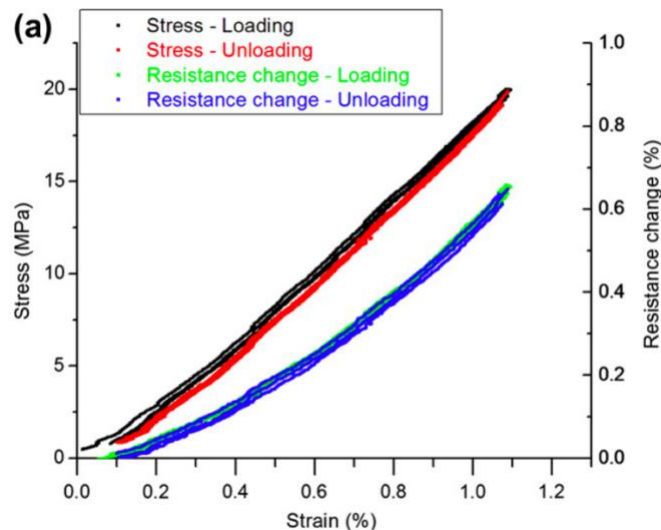


Figure 2.7: Resistance change as a function of the applied strain [53].

2.2.3 Previous Efforts to Improve GF

The conventional (metallic) strain gauges are found to exhibit a gauge factor (GF) of 2. This is a significant limitation in strain sensing applications. Li *et al.* researched the piezoresistive behavior of the buckypaper and found out that the GF improves when using higher aspect ratio CNTs. A GF of around 65 under 500 microstrains and at room temperature was reported [9][73]. Sanli *et al.* reported that MWCNT/epoxy nanocomposite strain sensor has a GF of 78 [66].

The improvement in the GF is may be due to the change in the CNTs bandgap caused by the strain [57]. According to the study conducted by Yang *et al.* [74], it was observed that the carbon nanotubes gauge factor is 8.18, while it has goodness of linear fit of 0.999, which indicates the linear behavior between the normalized change in the resistance and the applied strain. Also, the authors argued that loading the CNTs and increasing the ϵ results in opening the entanglement of the CNTs networks as well as allowing an additional slippage between CNTs. This, in turn, straightens the shape of CNTs and causes a significant change in the electrical resistance. Thus, the observed improved strain sensing.

Another study carried out by Wang *et al.* demonstrated the potential of buckypaper acting as a strain sensor with a relative GF of 13. Their study shows that applying strain results in changing the buckypaper morphology, which changes the piezoresistive behavior of the buckypaper [61].

On the other hand, Kang *et al.* studied the sensitivity of the BP. The study showed the limitation and degradation of strain sensing capabilities happen due to the slippage caused by the secondary forces between particles. To overcome this drawback, a novel CNT/PMMA composite was developed [56].

Table 2.2 summarized the GF values found in the previous studies.

Table 2.2: Summary of some of the GF values found in the previous studies.

Sensing material	GF	References
SWCNTs	65	[7]
MWCNT/Epoxy	78	[46]
CNT thin film	8.18	[59]
CNT thin film	13	[63]

2.3 BP-based Temperature Sensor

In this section, the BP-based temperature sensor will be discussed. The fabrication techniques will be reviewed in subsection 2.3.1, TCR values obtained in the literature will be addressed in 0, and the temperature versus resistance relationship will be presented in 2.3.3.

2.3.1 Fabrication Technique

Sanginovich *et al.* fabricated the temperature sensor by mixing the CNT nanopowder with thin layers of glue and then depositing the mixture on a paper substrate, as shown in Figure 2.8. The sample was subjected to compaction of 10 kN to enhance the durability [75]. The electrode terminals were connected to the BP sensor using the silver paste.

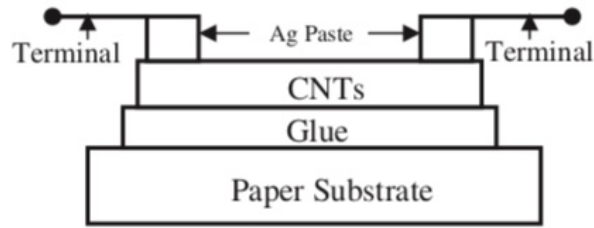


Figure 2.8: Schematic diagram of using the four-probe method to measure the resistance of CNTs [73].

According to the study carried out by Karimov *et al.*, the Al/CNT/Al temperature sensor was produced by depositing the CNT film on a tape made out of elastic tape and then packed in a flexible casing shown in Figure 2.9 [76].

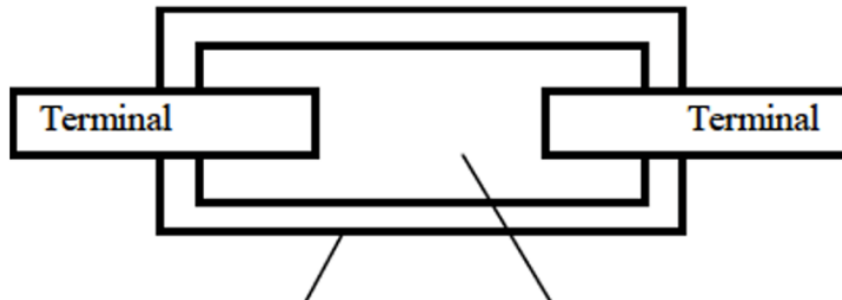


Figure 2.9: Schematic diagram of BP temperature sensor testing setup [75].

In the research conducted by Cagatay *et al.* [68], an automated spray deposition technique was proposed to fabricate and deposit the buckypaper, as illustrated in Figure 2.10. The low cost, reproducibility and the homogeneity of the deposited films were the reason behind working with the deposition approach.

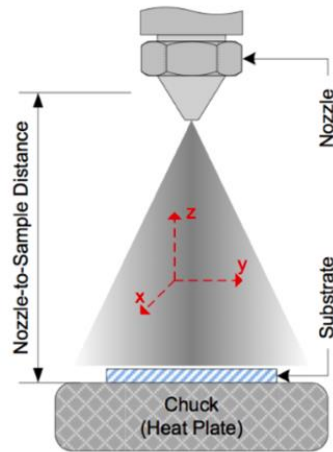


Figure 2.10: Schematic illustration represents the spray deposition fabrication technique [68].

Sarma *et al.* synthesized the buckypaper temperature sensor using CVD. MWCNTs were the sensing element, and Silicon (Si) was the substrate. A Diamond like-carbon catalyst (DLC: Ni) was sputtered on the substrate to assist the growth of the CNTs [77].

Furthermore, Saraiya *et al.* demonstrated the fabrication of CNTs using CVD assembling technique. In addition, a nickel (Ni) film catalyst was added to the float glass substrate [78]. The CNTs exhibited semiconducting behavior by getting exposed to nickel, as shown in Figure 2.11.

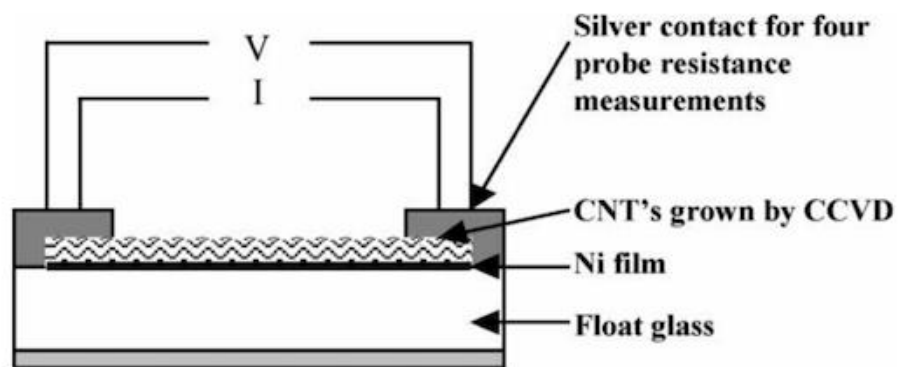


Figure 2.11: Schematic diagram illustrates CNTs grown on Ni film [78].

2.3.2 Temperature Sensitivity

The temperature sensor sensitivity is denoted by the temperature coefficient of resistance (TCR). It has the unit of $^{\circ}\text{C}^{-1}$, and it is given by the formula (2.1).

$$TCR = \frac{\Delta R/R_o}{\Delta T} \quad (2.1)$$

Where,

R_o : The initial resistance at which the experiment starts.

ΔR : Change in resistance.

ΔT : Change in temperature.

Her *et al.* investigated the temperature coefficient of resistance (TCR) for two different types of MWCNTS: high aspect ratio and the low aspect ratio, and the values were $-8.24 \times 10^{-2} \text{ }^{\circ}\text{C}^{-1}$ and $-1.05 \times 10^{-1} \text{ }^{\circ}\text{C}^{-1}$ [52].

Furthermore, Kuo *et al.* introduced a CNT temperature sensor with a TCR = $-0.0008152 \text{ }^{\circ}\text{C}^{-1}$ at the operating range between $25 \text{ }^{\circ}\text{C}$ to $135 \text{ }^{\circ}\text{C}$ [79]. Sarma *et al.* developed MWCNT temperature sensor with a TCR = $-1.03 \times 10^{-1} \text{ }^{\circ}\text{C}^{-1}$ at an increasing temperature range from $22 \text{ }^{\circ}\text{C}$ to $200 \text{ }^{\circ}\text{C}$ [80]. Besides, Cagatay *et al.* introduced a high-density CNT sensor by stacking it into layers. The sensor was tested in a range from $0 \text{ }^{\circ}\text{C}$ to $80 \text{ }^{\circ}\text{C}$, and the TCR was $-0.002954 \text{ }^{\circ}\text{C}^{-1}$ [68].

Table 2.3 summarizes the TCR values of different types of BP-based temperature sensor available in the literature. A negative TCR was observed in all cases showing that the resistance of CNT films decreases as temperature increases.

Table 2.3: Summary of TCR values as found in the previous studies.

Sensing material	Working range	TCR	References
MWCNTs with the high aspect ratio	22 °C to 200°C	$- 8.24 \times 10^{-2} \text{ }^{\circ}\text{C}^{-1}$	[48]
MWCNTs with the low aspect ratio	22 °C to 200°C	$-1.05 \times 10^{-1} \text{ }^{\circ}\text{C}^{-1}$	[48]
CNT film	25 °C to 135 °C	0.0008152/K	[76]
MWCNT film	22 °C to 200 °C	$-1.03 \times 10^{-1} \text{ }^{\circ}\text{C}^{-1}$	[77]
CNT film	0°C to 80 °C	$-0.002954 \text{ }^{\circ}\text{C}^{-1}$	[65]

2.3.3 Resistance Vs. Temperature Relation

The range of temperature used by Sanginovich was from 20°C to 75°C, and the resistance decreases by 1.2 times as the temperature increases, as shown in Figure 2.12 [75].

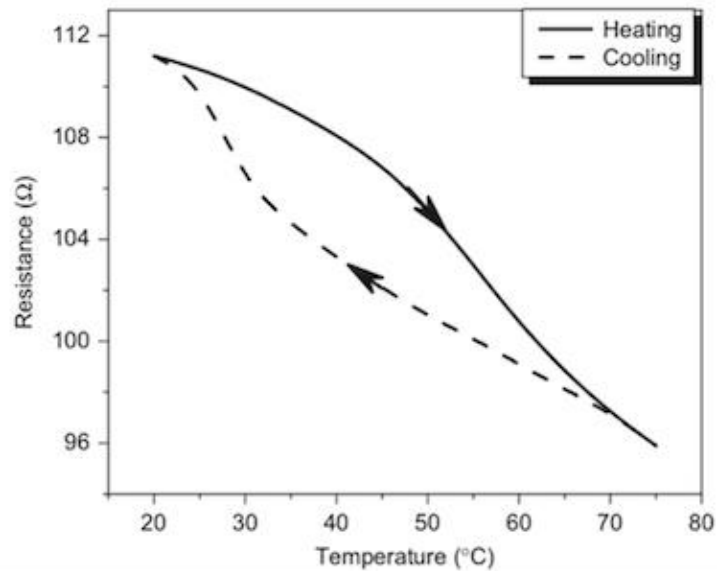


Figure 2.12: Temperature Vs. resistance relationship in heating/cooling process [57].

In accordance with the previous study, Johnson *et al.* [81] reported that resistance decreases as temperature increases, as shown in Figure 2.13.

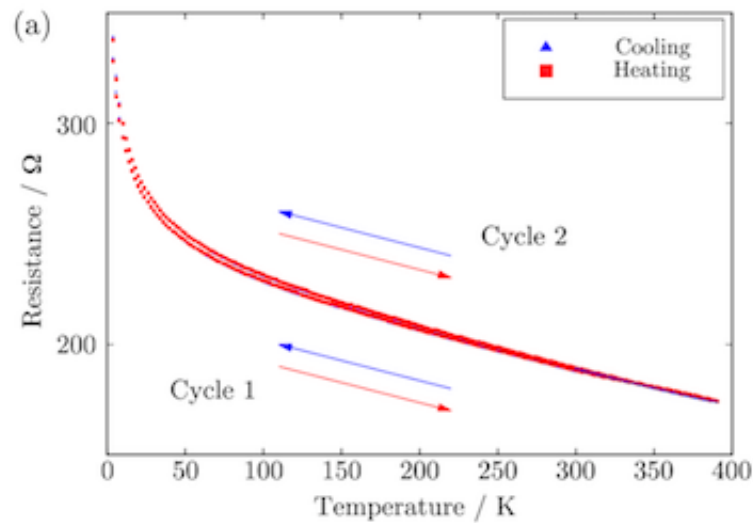


Figure 2.13: Resistance change as a function in temperature [64].

2.4 Summary of Literature Review

This literature review summarizes the current knowledge in CNT-based strain and temperature sensors. However, there are some existing gaps in terms of:

- Limited sensitivity associated with the current BP-based strain sensors. Thus, a novel combination of treatments was proposed to enhance the buckypaper strain and temperature sensitivities through enhancing the GF and TCR values.
- Lack of understanding of the behavior of the buckypaper when exposed to mechanical strain and a heat source at the same time. Therefore, the present study intends to combine the effect of strain and temperature and to investigate how the temperature change will affect the strain sensitivity. This will be obtained through observing the changes in the BP electrical resistance during the exposure to both factors, strain and temperature, simultaneously.

CHAPTER 3: MATERIALS AND EXPERIMENTAL METHODS

This chapter is divided into four key sections; section 3.1 presents the materials used, section 3.2 discusses the fabrication techniques, section 3.3 demonstrates the applied combination of treatments, and section 3.4 discusses the characterization techniques used for strain and temperature sensing.

3.1 Materials

3.1.1 Elicarb CNT Powder

Figure 3.1 shows Elicarb MWCNTs that were supplied by (Thomas Swan & Co. Ltd – County Durham, UK.) in the form of dry powder. The inner diameter of MWCNTs is between 1 to 2 nm, and the external diameter ranges from 3 to 30 nm.

The CNTs were used as received. It is worth noting that MWCNTs exhibit higher electrical conductivity, higher purity, higher dispersibility with less opportunity to form bundles, and are more economical than SWCNTs [82]. Hence, they were selected as the used material.



Figure 3.1: As received dry powder form of Elicarb MWCNTs supplied by Thomas Swan [83].

3.1.2 Isopropyl Alcohol (IPA)

The used solvent for the apparatus Isopropyl Alcohol (IPA) was supplied by Sigma-Aldrich company. A set of experiments was carried out to obtain the best composition in terms of dispersion and homogeneity. The optimum formula was diluting 0.025 gm of CNT powder into 160 ml of IPA. IPA was the chosen solvent owing to its properties, such as: enhancing the dispersibility by preventing the formation of the bundles [84].

3.2 Processing & Fabrication Techniques

3.2.1 BP Fabrication

To fabricate the buckypaper, two methods were tested: The first one is the surfactant method where Triton X-100 was added to the Elicarb powder and sonicated then filtered, and the second one is the low-temperature method where the sonication process was done at 7°C. There was an issue associated with the surfactant method that the produced BPs had impurities in addition to the length of time taken by the procedure. Based on that, the latter method was selected.

3.2.1.1 Dispersion

One of the main obstacles that are faced by researchers is the CNTs high surface area. In other words, CNTs tend to cluster and agglomerate to minimize the surface energy [85]. Consequently, numerous methods were investigated to enhance the dispersibility of CNTs [86],[87]. The dispersion process aims at homogenizing the produced films.

In the current study, the first step in achieving uniform dispersion of the CNTs in IPA involved weighing 0.05 grams of Elicarb MWCNTs with a Mettler Toledo sensitive balance and then diluting them in 160 ml of Isopropyl Alcohol (IPA) acting as the solvent material. The solution was suspended into a beaker and sealed with a plastic wrap, supplied by Sigma-Aldrich, to preserve it and prevent evaporation.

3.2.1.2 Stirring

To improve CNTs dispersion, the formed bundles needed to be separated. Stirring is an effective process to disperse the material particles into any solvent/surfactant [88]. To improve the dispersion, the beaker was placed onto the magnetic stirrer (supplied by Stuart, UC152) for 30 minutes, as shown in Figure 3.2.

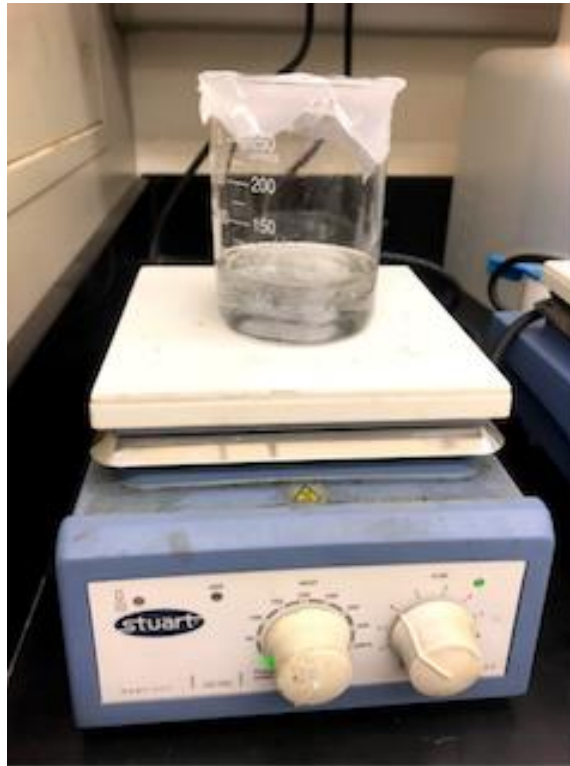


Figure 3.2: The magnetic stirrer used for sample dispersion; image was taken at AUC chemistry lab.

3.2.1.3 Sonication

Sonication is a process where the beakers are placed in an ultrasonic bath. Figure 3.3 shows the sonicator (VWR, model 150 HT), used to provide sound energy to the beaker, containing Elicarb MWCNTs powder dissolved in IPA solvent, and it eventually enhances the dispersion and the solubility of the mixture [89].

The temperature of the sonicator should be kept at 7°C. Therefore, the sonicator was filled with ice and continuously monitored. The sonicator was turned on and left empty for 15 minutes, then the beakers were placed into the sonicator for an hour. The filtration process started upon the completion of the sonication process.



Figure 3.3: The sonication process. (a) The sonication bath after placing the two samples was divided into four beakers and (b) The sonication bath prior to placing the ice and the samples. The images were taken at AUC chemistry research lab.

3.2.2 Filtration Process

Vacuum filtration is a common technique to fabricate the CNT thin films. The pressure difference of the Buchner funnel is responsible for the separation process between CNTs and solvents. The formation of the BP is followed by a peeling process where you peel the produced sample from the filter membrane and then the sample is left in air to dry. A 47 mm Polytetrafluoroethylene (PTFE) filter membrane supplied by (Chrom tech, Inc. UK) [90] was placed on top of the Buchner funnel, and the solution was poured through it. The filtration process was done in 60 minutes using a vacuum filtration setup.

The formed freestanding BPs have the exact dimensions of the filter membrane. The BP was air-dried then it was peeled carefully from the membrane. To avoid contamination that may deteriorate the BP properties significantly, the BP was transferred into a well-sealed plastic beaker. By following the previous steps, BP is ready to use in mechanical testing, as shown in Figure 3.4.

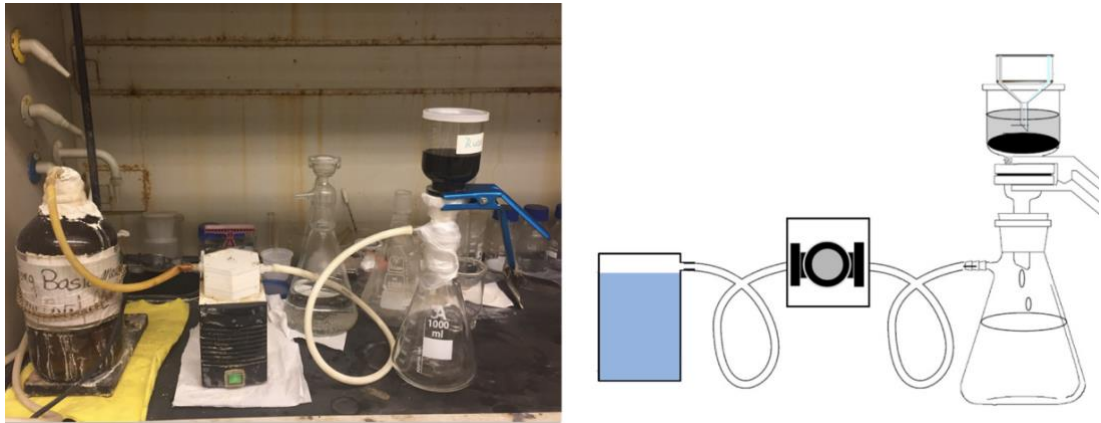


Figure 3.4: The vacuum filtration setup. (a) The experimental setup at AUC chemistry research lab, (b) a schematic illustration of the filtration process.

Figure 3.5 (a) summarizes all the fabrication processes that the buckypaper is passing through in order to be ready for the characterization phase. In addition, Figure 3.5 (b) shows the produced buckypaper sample. It has a diameter of 47 mm and a thickness of 35 μm according to the scanning electron microscopy (SEM) analysis.

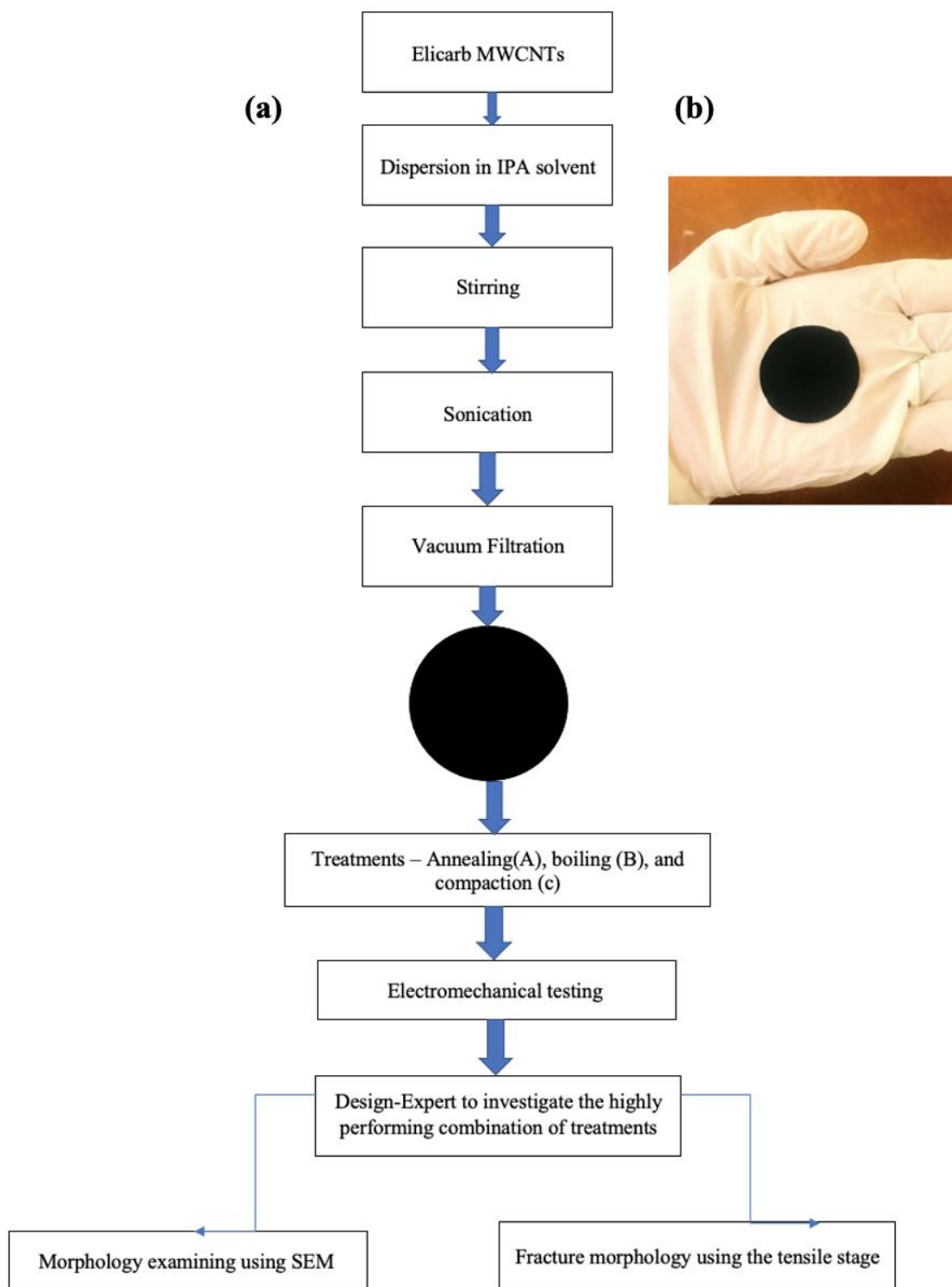


Figure 3.5: Summary of the fabrication processes. (a) Schematic representation of the buckypaper fabrication procedure and (b) The BP sensor after preparation step and prior to testing.

3.3 Applied Treatments Before Testing (A, B, and C)

3.3.1 BP Conditioning

Some studies mentioned the influence of applying treatments to the CNTs thin film on the sensitivity [81] [91]. In the current study, BPs were exposed to annealing (A), boiling (B), and compaction (C). Each treatment has three different levels: low, medium, and high, as shown in Table 3.1. The aim of conditioning the samples is to test the BP sensitivity under several conditions and to find out if there is a specific condition or combination that impacts the samples positively (in terms of gauge factor value GF).

Table 3.1: Different conditions applied to the BP samples with different levels.

Factors	Units	Levels of Factors		
		Low	Medium	High
Annealing (A)	°C	RT	100	200
Boiling (B)	Minutes	No treatment (-)	30	60
Compaction (C)	kN	No treatment (-)	5	10

The idea of the design of experiments (DOE) software is that it contains one dependent variable denoted by “response” and an independent variable denoted by “factors.” Experimental trials are called runs, which take place at different values of the factors. At each experimental run, a combination of levels was investigated [92]. In the meantime, three replicates were made from each combination to guarantee reliable results, and GF was computed by their average value [92].

The aim is to understand the influence of one experimental factor on other factors and whether the chosen variables have positive or negative impacts on the response. Reflecting on the current study, the selected response is the gauge factor, while the factors are annealing, boiling, and compaction. Testing all the experimental combinations would result in 3^3 runs.

3.3.2 Annealing

According to Johnson *et al.* [81], the CNTs transport properties, in terms of electrical and thermal conductivity, are significantly improved by annealing. In the current work, the BP samples were placed in an electric oven for an hour according to the desired annealing level, either 100°C or 200°C. The samples stayed for an hour inside the electric oven and then the sample was taken out for testing.

3.3.3 Exposure to Boiling Solvent

In this treatment, the BP sample was exposed to Dimethylformamide (DMF) for either 30 or 60 minutes. A hot plate was used to boil a 150 ml of DMF solvent, and the solution was boiled for 40 minutes. Additionally, a wire mesh was used to cover the BP beaker. Another inverted beaker was placed on top of the wire mesh to avoid solvent volatility, as shown in Figure 3.6.



Figure 3.6: The used boiling setup. The image was taken at AUC chemistry research lab.

3.3.4 Compaction

Zhong *et al.* showed that subjecting CNTs to compaction would result in a significant improvement in terms of mechanical properties and strength [93]. Furthermore, the compaction process led to making the CNT film densely compacted, which eventually translates into increased strength.

In the current study, the compaction was done with the aid of the universal testing machine shown in Figure 3.7. BP samples were placed between two rectangular metal discs were subjected to compaction forces of either 5 kN or 10 kN according to the sample conditioning.



Figure 3.7: A universal testing machine used for compacting CNT samples. The image was taken at AUC materials testing lab.

3.4 Characterization

3.4.1 BP morphology using Scanning Electron Microscopy (SEM)

SUPRA 55 FESEM was used to characterize the BP morphology and the fracture morphology with the aid of the tensile stage demonstrated in the sub-section 3.4.2. For SEM analysis, the BP samples were cut and mounted onto a silver stub using a conductive adhesive. The used operating parameters in the SEM analysis were a voltage of around 10 KV and a working distance (WD) of 4 mm.

3.4.2 Fracture Morphology Using the Tensile Stage

Figure 3.8 shows the external view of the tensile stage equipment (TS-1500-III) used for evaluating the behavior of BPs by applying quasi-static loading/unloading cycles. The motivation behind using the tensile stage is the nature of the sensor being a thin film. Thus, strength and elongation could not be measured using a conventional tensile testing machine. The tensile stage was used because it allows very small loads to be applied. Moreover, it allows in-situ loading and fracture observation inside the SEM.

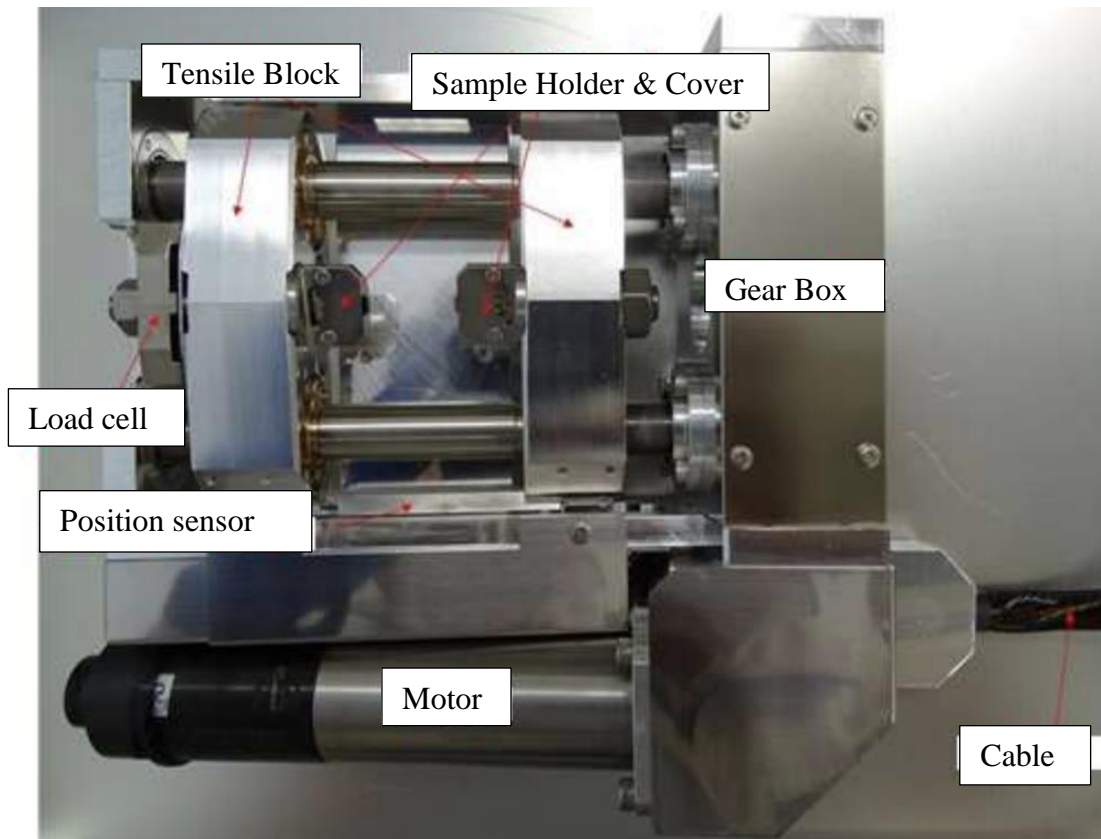


Figure 3.8: Tensile stage external view [94].

Figure 3.9 (a) shows a BP sample after cutting it using a press cutter into a typical dog-bone-shape with a standard dimensions of 15.125 mm x 4.25 mm x 0.035 mm. Figure 3.9 (b) shows the used tensile stage, which is designed to hold the sample in a horizontal position to properly secured inside the SEM vacuum chamber as described in section 3.4.1.

A series of tensile tests were run using a 50 N load cell, EHT of 10 KV, WD = 4 mm, and at a speed rate of 5 mm/min. Additionally, the images were recorded each 50 mm displacement until failure. Following the failure, the fracture morphology of the sensor was assessed by observing the resulting images and the force-displacement curves, as demonstrated later in Figure 4.6.

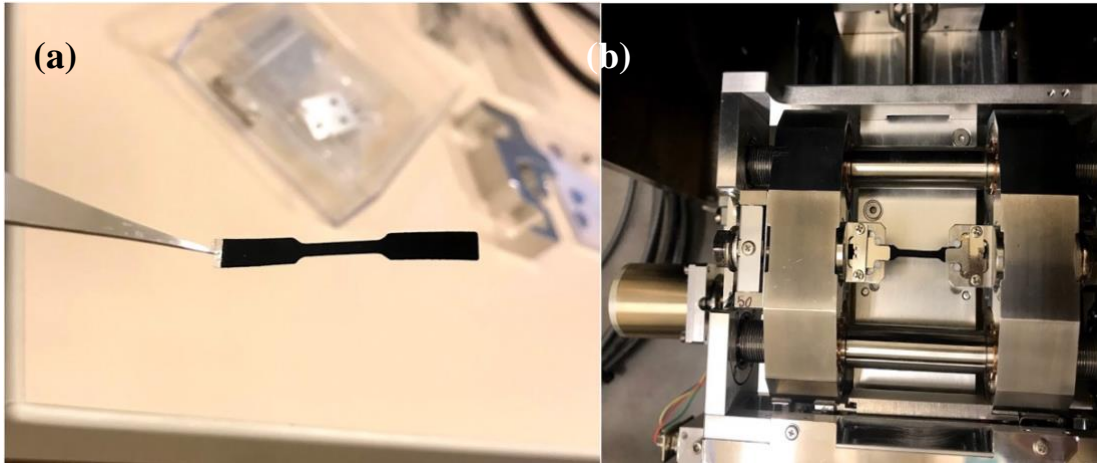


Figure 3.9: SEM using tensile stage setup. (a) the prepared CNT tensile specimen prior to testing, and (b) The sample fixation inside the tensile stage.

3.5 BP-based Strain Sensor

3.5.1 Strain Sensor Testing Setup

To assess the piezoresistive behavior of the proposed sensor, the prepared BP samples were cut into rectangular strips measuring $1\text{ cm} \times 3\text{ cm} \times 0.0035\text{ cm}$ and fixed on a $20 \times 4 \times 2\text{ cm}$ plastic beam which was used as the test beam specimen.

The beam was fixed from one end to stimulate the cantilever behavior. The BP sample was adhered to the center of the beam surface using double-sided tape.

In order to measure the electrical resistance, two copper electrodes were placed onto the sample and were connected to a digital multimeter (FLUKE 15B) using electrical wire probes [95]. The beam was subjected to incremental loads up to 160 g in increments of 20 g, as shown in Figure 3.10. The gauge factor was evaluated according to equation

$$(1.1).$$

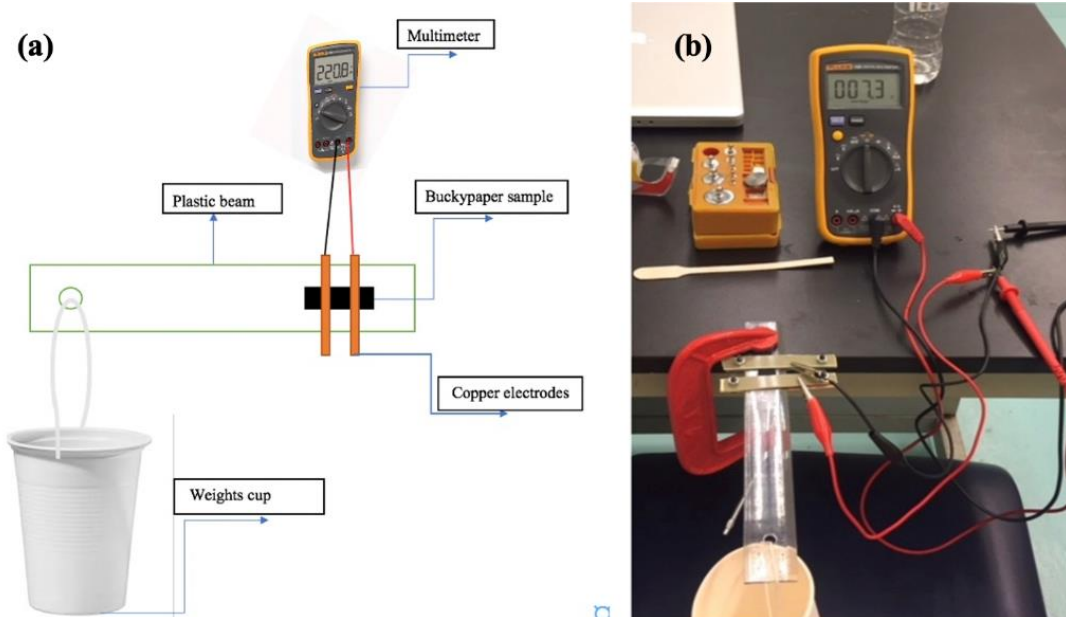


Figure 3.10: Strain sensor testing setup (a) schematic representation of the setup and (b) the actual testing setup captured at AUC vibration lab.

3.5.2 Strain Calculations

To calculate the theoretical values of the strain, the beam bending theory was used.

The bending stress is calculated using the equation (3.1)

$$\sigma = \frac{MY}{I} \quad (3.1)$$

Where:

- σ Bending stress
- M Internal bending moment
- Y Half the beam thickness
- I Moment of inertia.

The theoretical strain (ε) is calculated using the formula (3.2)

$$\varepsilon = \frac{MY}{EI} \quad (3.2)$$

Where E is the young's modulus and was calculated according to the used beam material. For instance: when the used beam was polystyrene the value of E was determined accordingly and the same was applied for the stainless-steel beam. The dimensions of the different parts in the testing setup were measured as recorded below in Table 3.2. To calculate the GF values, the dimensions, as shown in Figure 3.11, were measured carefully, and the theoretical strain was calculated at different loads. It is worth noting that two different types of beams were used: a plastic beam was used in the strain experiment where there was no applied heat. On the other hand, a stainless-steel beam was used in temperature experiments and strain/temperature combined experiments.

Table 3.2: Dimensions of the apparatus components.

Sensor dimension (m ³)	$L \times W \times H$	0.03 x 0.01 x 0.00035
Distance from the free end to the BP center (m)	ℓ	0.15
Depth of plastic beam (m)	h_p	0.002
Depth of Stainless-steel beam (m)	h_s	0.0012
Width of plastic beam (m)	b_p	0.03
Width of Stainless-steel beam (m)	b_s	0.02
Young's modulus of plastic (N/m ²)	E	3.25×10^9
Young's modulus of stainless steel (N/m ²)	E	1.90×10^{10}
Second Moment of Inertia ($bh^3/12$) (m ⁴)	I	200×10^{-9}

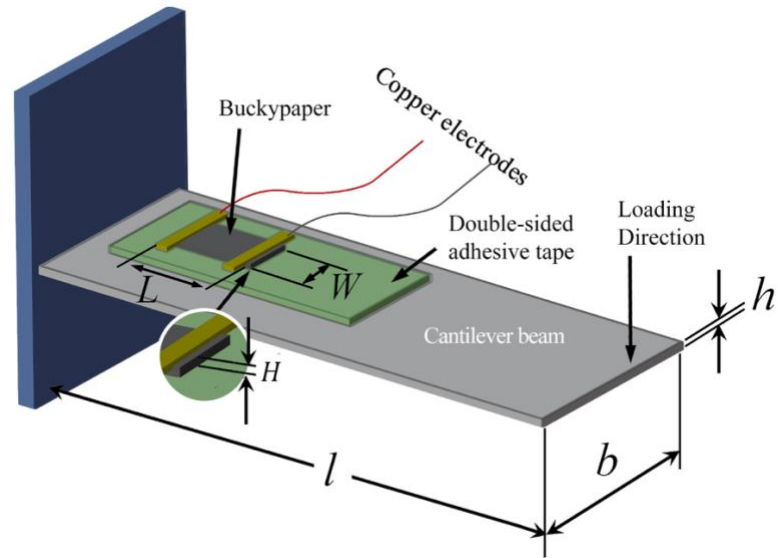


Figure 3.11: Schematic illustration for the cantilever beam.

3.6 Buckypaper-based Temperature Sensor

The key point behind using CNT films in the miniaturized sensors is that they offer a high-temperature sensitivity with a speedy response to the change in temperature with a significant low energy consumption compared to the conventional temperature sensors [96].

3.6.1 Temperature Testing Setup

The temperature sensitivity of the proposed BP sensor was investigated through attaching the sensor to a stainless-steel beam and subjected to a heat source. The temperature varied from room temperature to 80°C. The temperature was measured by an infrared thermometer.

The corresponding change in resistance data was collected every ten degrees by a digital multimeter, as shown in Figure 3.12 (b). The temperature sensitivity was characterized by the temperature coefficient of resistance (TCR) illustrated below.

$$TCR = \frac{\Delta R/R_0}{\Delta T}$$

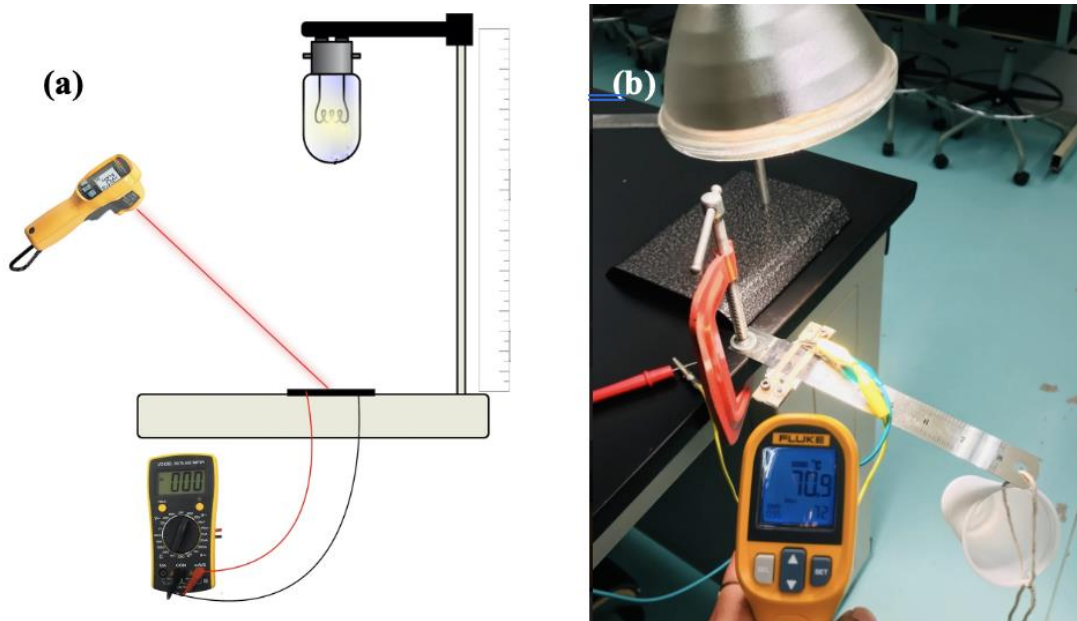


Figure 3.12: Temperature sensor testing setup (a) schematic representation of the setup and (b) the actual testing setup captured at AUC vibration lab.

3.7 Factors to be studied

To further enhance the strain and temperature sensitivities, the mentioned three treatments annealing, boiling solvent, and compaction will be applied to the produced sensor and their influence will be studied using half normal plot and Design-Expert software.

CHAPTER 4: RESULTS AND DISCUSSION

The results of strain and temperature experiments are presented in this chapter. The chapter begins with discussing the strain results in order to identify the sample with the combinations of treatments that gave the highest gauge factor. This sample will then be used in the temperature experiments.

A comparative assessment will be conducted between the highest GF sample and the control sample. Lastly, SEM imaging results that show the morphology of the BP-based sensor are presented. Moreover, the results of the fracture morphology of different samples, which were evaluated by loading the BP samples inside the SEM chamber using the tensile stage will be presented.

4.1 Design-Expert Results

Design expert software was used to determine the most influential factors in terms of GF and improving the sensitivity. Based on that, two different methods were used: the first one is the ANOVA model as shown in Table 4.1, and the second is the half-normal plot illustrated in Figure 4.1. According to design expert software results presented in Table 4.1, the factors that have a P-Value less than 0.05 indicate that they have a significant/positive impact on the response, the GF values.

In addition, factors with a P-value greater than 0.1 indicate that they have an insignificant/negative effect on results. Reflecting on the current study, it was observed that AC, BC, and C have the most significant impact on the gauge factor (GF). However, A, B, and ABC have a negative effect on the GF.

Table 4.1: ANOVA model results generated by Design-Expert software.

Factors	P-Value	Significance
AC: Annealing + Compaction	0.0011	Yes
BC: Boiling + Compaction	0.0085	Yes
C: Compaction	0.0199	Yes
A: Annealing	0.2916	No
B: Boiling	0.4644	No
ABC: Annealing + Boiling + Compaction	0.0856	No

Table 4.2 shows the calculated gauge factor values for the 81 samples. The control sample has a gauge factor of 17, which is still eight times higher in sensitivity than the conventional strain gauge. Furthermore, the highest GF value was obtained when the annealing and compaction treatments were combined at the same time.

According to Table 3.1, A_, B_, C_ represents the control sample/low level of the treatments where the BP sample is at room temperature and without applying any compaction force or exposing it to the boiling solvent. As mentioned earlier in section 3.3.1, three samples were produced from each combination of treatments to ensure the accuracy and reliability of the fabrication procedure and the GF values. Thus, appendix A graphically presents the results of the 81 samples where every three samples exposed to the same treatments are grouped and compared together. It was found that the variation in the GF for each group of treatments is minimal.

Table 4.2: Calculated gauge factors for all samples.

Sample number	Sample factors	Average GF
1	A_, B_, C_	17
2	A_, B_, C_	18.34
3	A_, B_, C_	16.62
4	A_, B_, C5	33.34
5	A_, B_, C5	25
6	A_, B_, C5	43.05
7	A_, B_, C10	49.44
8	A_, B_, C10	55
9	A_, B_, C10	48.54
10	A_, B30, C_	29.75
11	A_, B30, C_	49.8
12	A_, B30, C_	29.44
13	A_, B30, C5	37
14	A_, B30, C5	33.7
15	A_, B30, C5	32.4
16	A_, B30, C10	48.2
17	A_, B30, C10	49
18	A_, B30, C10	45.8
19	A_, B60, C_	39.63
20	A_, B60, C_	40.36
21	A_, B60, C_	36.56
22	A_, B60, C5	35.53
23	A_, B60, C5	35.53
24	A_, B60, C5	27.69
25	A_, B60, C10	45.52
26	A_, B60, C10	48.2
27	A_, B60, C10	54.5

28	A100, B_, C_	32.82
29	A100, B_, C_	53.82
30	A100, B_, C_	44.69
31	A100, B_, C5	76.26
32	A100, B_, C5	62.87
33	A100, B_, C5	78.2
34	A100, B_, C10	175.5
35	A100, B_, C10	169.13
36	A100, B_, C10	179.68
37	A100, B30, C_	45.89
38	A100, B30, C_	51.24
39	A100, B30, C_	55.1
40	A100, B30, C5	62.93
41	A100, B30, C5	59
42	A100, B30, C5	60.12
43	A100, B30, C10	42.13
44	A100, B30, C10	35
45	A100, B30, C10	42.38
46	A100, B60, C_	58.92
47	A100, B60, C_	41.47
48	A100, B60, C_	39.2
49	A100, B60, C5	21.47
50	A100, B60, C5	24.74
51	A100, B60, C5	33.17
52	A100, B60, C10	19.05
53	A100, B60, C10	16.12
54	A100, B60, C10	19.05
55	A200, B_, C_	47.56
56	A200, B_, C_	59.6
57	A200, B_, C_	47
58	A200, B_, C5	14.5

59	A200, B_, C5	13
60	A200, B_, C5	20.82
61	A200, B_, C10	33.68
62	A200, B_, C10	50.1
63	A200, B_, C10	38.02
64	A200, B30, C_	68.34
65	A200, B30, C_	75.1
66	A200, B30, C_	67.54
67	A200, B30, C5	32.62
68	A200, B30, C5	37
69	A200, B30, C5	34.18
70	A200, B 30, C10	28.17
71	A200, B 30, C10	32.42
72	A200, B 30, C10	38.26
73	A200, B60, C_	65.3
74	A200, B60, C_	54.12
75	A200, B60, C_	58.4
76	A200, B60, C5	52.9
77	A200, B60, C5	47.77
78	A200, B60, C5	52.13
79	A200, B60, C10	38.3
80	A200, B60, C10	47.34
81	A200, B60, C10	41.7

4.1.1 Half-Normal Plot Results

Figure 4.1 shows the Half-Normal plot generated by the Design-Expert software. A half normal plot is an important tool used to assess all the experimental factors/treatments (annealing, boiling, and compaction) in addition to evaluating the impact of the factors on the output (GF). In this study, it was observed that annealing and compaction had the highest positive impact on the output.

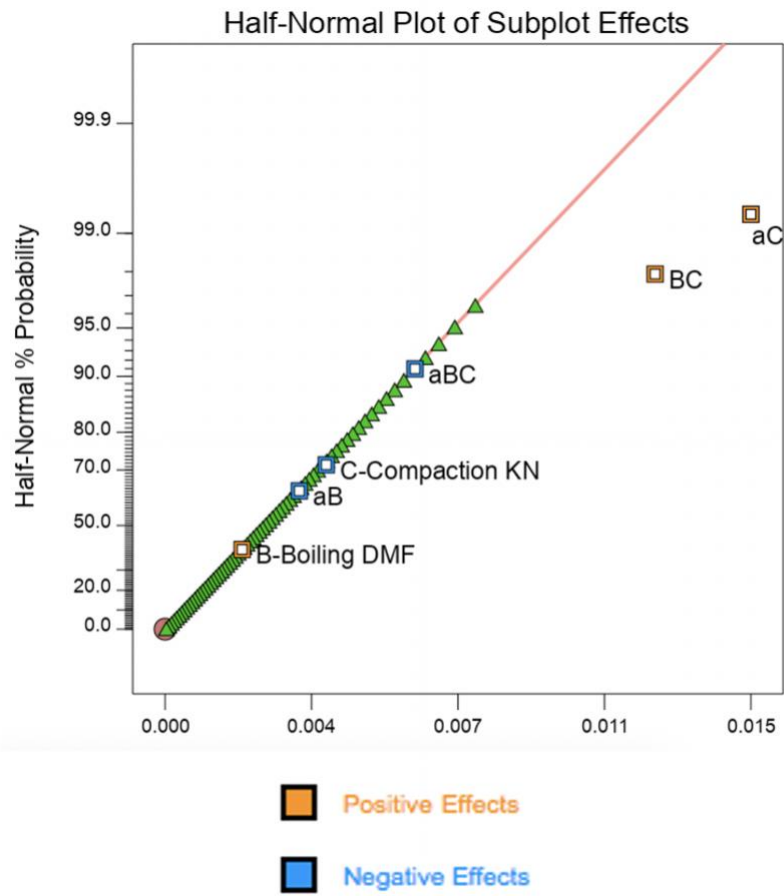


Figure 4.1: Design expert half-normal probability graph result.

4.2 Buckypaper-based Strain Sensor

4.2.1 Loading/Unloading results

Figure 4.2 (a) and Figure 4.2 (b) show the normalized change in the resistance ($\frac{\Delta R}{R_0}$) in response to the applied strain (ϵ). Figure 4.2 (a) represents the control sample with no treatments (A0, C0), and Figure 4.2 (b) shows the sample subjected to a temperature of 100 °C and compaction of 10 kN (A100, C10). It can be observed that the buckypaper exhibits a linear behavior with $R^2 = 0.99$ in response to the applied load. The BP showed a potential to be used as a strain sensor due to the linearity and repeatability of the ($\frac{\Delta R}{R_0} - \epsilon$).

The gauge factors for the control sample A0, C0, and A100, C10 are 17.32 and 174.8, respectively. It is worth noting that the treatments, annealing, and compaction, clearly enhanced the BP sensitivity. The significant increase in the gauge factor value confirms that applying combinations of different treatments within certain levels can drastically improve the MWCNTs piezoresistive behavior since the increased BP electrical resistance due to the applied strain. The effective resistance of the buckypaper can be divided into two main types: the intrinsic resistance, which has a noticeably minor effect on BP resistance, and the resistance between the contacted tubes referred to as the intertube resistance. while the second resistance is composed of two resistances which are the resistance of the contacted tubes referred to as the contact resistance R_C and the resistance of tubes separated by a relatively small band gap namely tunneling resistance [52], [62].

The dominating mechanism of the BP piezoresistivity is the tunneling resistance variation where electrons are transported between neighboring CNTs.

When BP is subjected to tensile loading, it is stretched, increasing the tunneling distance between neighboring MWCNTs [97]. Increasing the tunneling distance leads to increasing the tunneling effect and decreasing the conductive paths of CNTs. Consequently, reduced conductivity and enhanced electrical resistivity are observed, as confirmed by the increase in resistance when subjecting the BP to strain.

On the other hand, in the unloading cycles, the electrical resistance decreases as the load decreases. When the load is removed, the tunneling distance between MWCNTs decreases leading to increased conductive paths and reduced resistance. The loading/unloading behavior is consistent in the 81 samples, and the obtained GF numeric values are listed in

According to Table 3.1, A_, B_, C_ represents the control sample/low level of the treatments where the BP sample is at room temperature and without applying any compaction force or exposing it to the boiling solvent. As mentioned earlier in section 3.3.1, three samples were produced from each combination of treatments to ensure the accuracy and reliability of the fabrication procedure and the GF values. Thus, appendix A graphically presents the results of the 81 samples where every three samples exposed to the same treatments are grouped and compared together. It was found that the variation in the GF for each group of treatments is minimal.

Table 4.2. Furthermore, all loading/unloading graphs are displayed in Appendix B.

The difference in response to strain between the control sample A0, C0 versus the sample with the highest gauge factor A100, C10 can be related to the increased densification in the case of A100, C10, as discussed below.

According to Danish *et al.* [98], compression increases the packing density of buckypaper, leading to increasing the bonding between the inter-tubes and decreasing the inter-tube distances. Additionally, Wang *et al.* [99] reported that BP mechanical properties are a function of the BP packing density. In other words, the denser the BP structure, the higher the electrical conductivity.

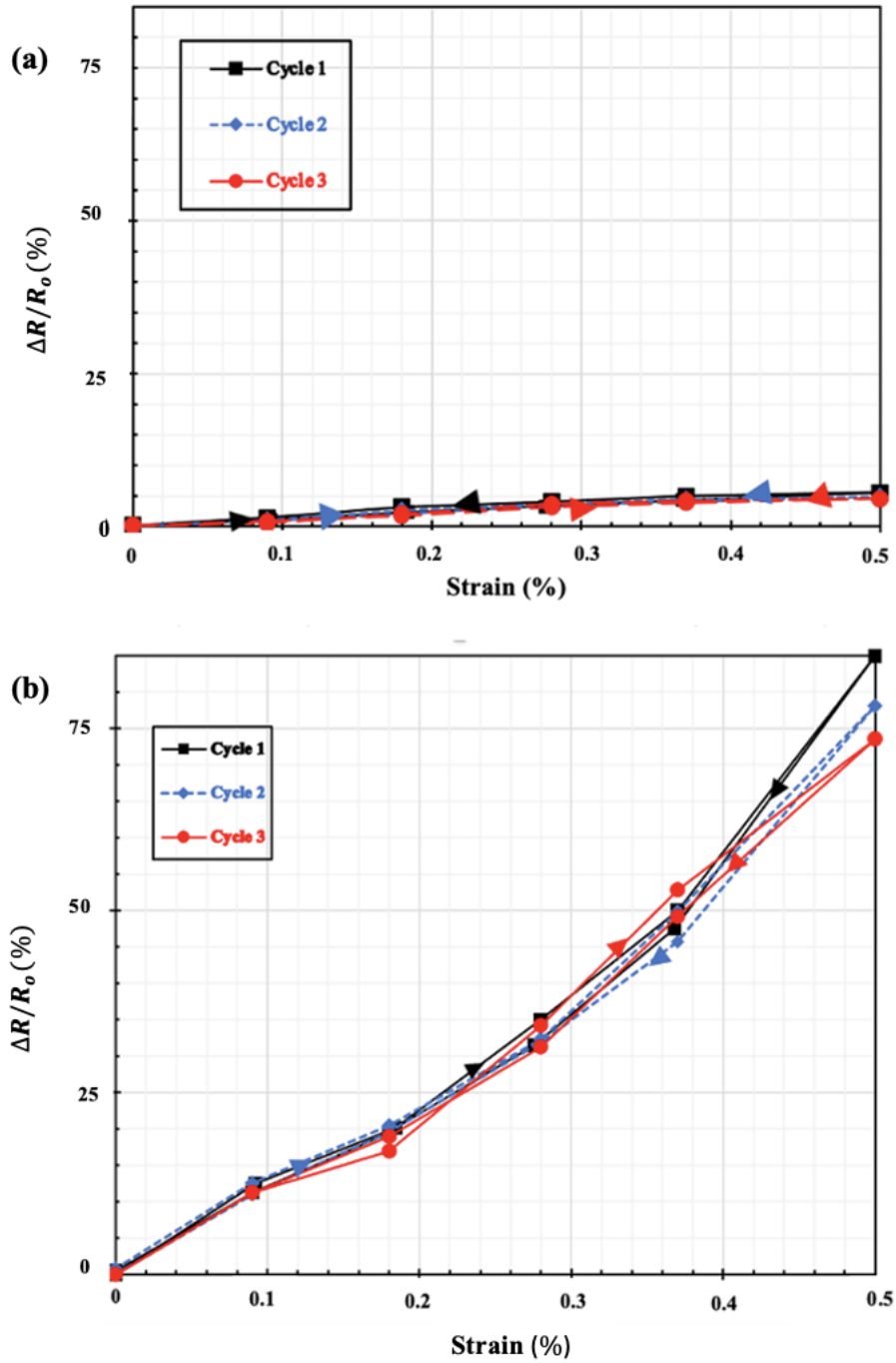


Figure 4.2: Cyclic loading of BP-based strain sensor. Three loading/unloading cycles of (a) control sample and (b) A100, C10. The experiment was carried out on a plastic beam.

4.3 Buckypaper-based temperature sensor

4.3.1 Heating/Cooling Results

The resistivity behavior was observed during several subsequent cycles of heating/cooling, as shown in Figure 4.3 (a) and Figure 4.3 (b). The proposed BP-temperature sensor showed a linear reversible behavior. To assess the sensitivity of any temperature sensor quantitatively, a TCR value should be determined. TCR has the same analogy as the GF, but the induced change in the resistance happens due to the change in the temperature instead of changing the force/applied load.

The TCR values were computed using Equation (2.1) and were found to be -0.0038 °C⁻¹ for the (A0, C0), and -0.0064 °C⁻¹ for the (A100, C10). The resistance decreases as temperature increases, resulting in negative TCR values, which agrees with previous findings in the literature [52][33][77]. The decrease of resistance can be attributed to the semiconducting behavior that MWCNTs exhibit as a response to thermal excitation [100].

As the temperature goes up, the gained energy of the valence electrons is transformed from a thermal energy to a kinetic energy which increases the inter-tube mobility of electrons of individual CNTs, and the mobility of electrons between adjacent CNTs. Therefore, the electrons leap easily across the potential barrier, from the valence band into the conduction band, increasing the conductivity and decreasing the resistance [101].

It can be observed that (A100, C10) sample has a higher slope value (TCR), which translates to a higher thermal sensitivity. Annealing was previously investigated to have an influence on the electrical and thermal conductivities of CNTs [81],[102].

This influence is owing to the contribution of thermal annealing in:

- Annealing significantly eliminates the contaminants and impurities [103].
- Improving the CNTs structure [17].
- It helps to recover the wall defects of CNTs that are initially existed [104].
- Improves the CNTs crystallinity [105]

On the other hand, compaction has a positive role in enhancing the transport properties of the CNTs. It was reported by Tsai *et al.* [106] that compression enhances the conductivity of MWCNTs thin films. At first, the as received bucky powder has a great tendency to agglomerate. However, by applying a compression force, the distance between the carbon nanotubes decreased, increasing the BP density and, hence, the conductive paths [62] [107].

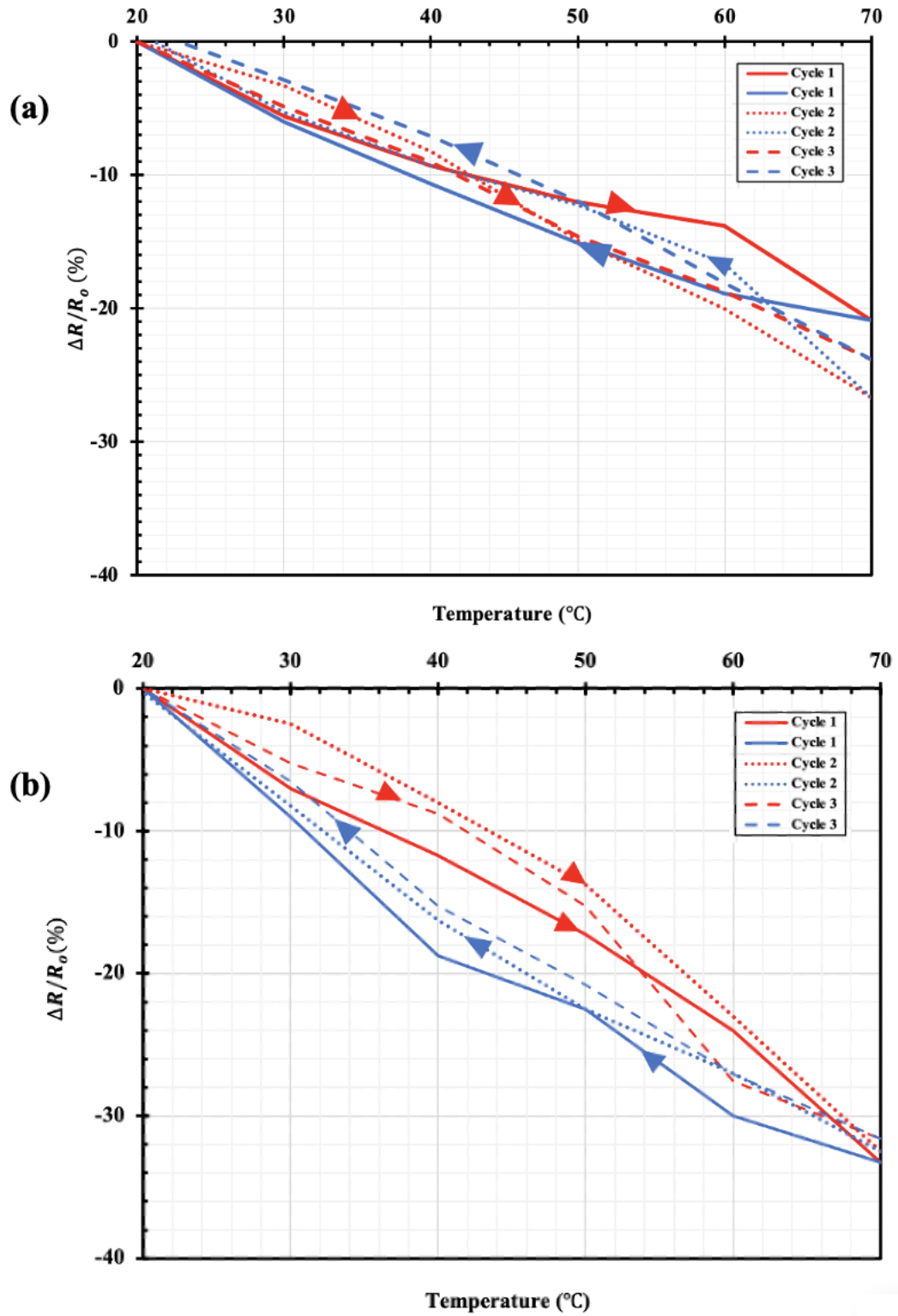


Figure 4.3: Thermal Cyclic of BP. the heating process is represented by the red lines, and the cooling process is represented by the blue lines. (a) Control sample (A0, C0) and (b) (A100, C10).

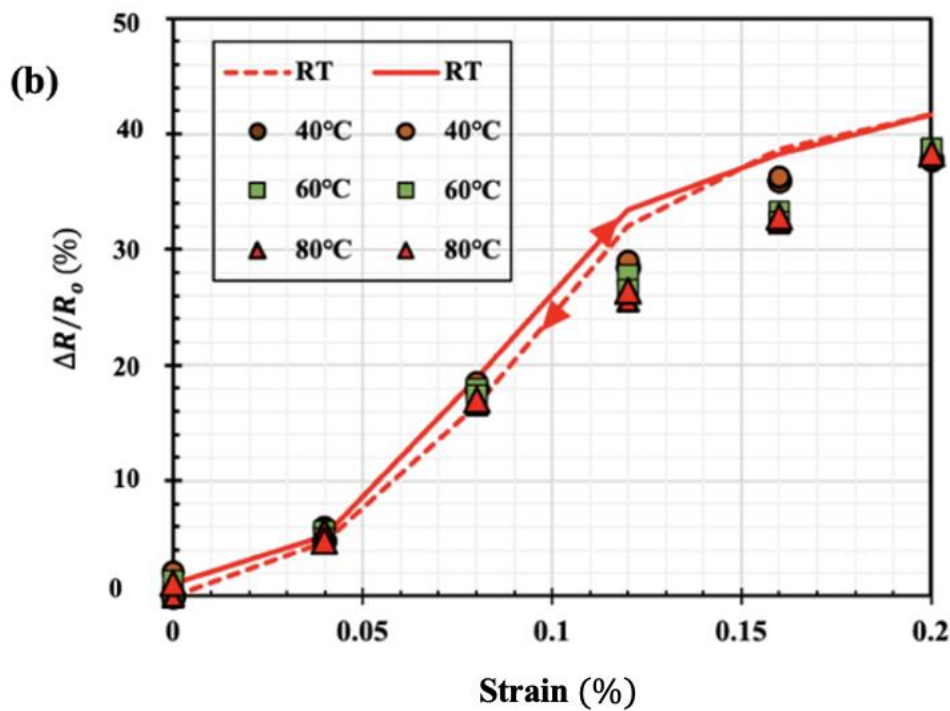
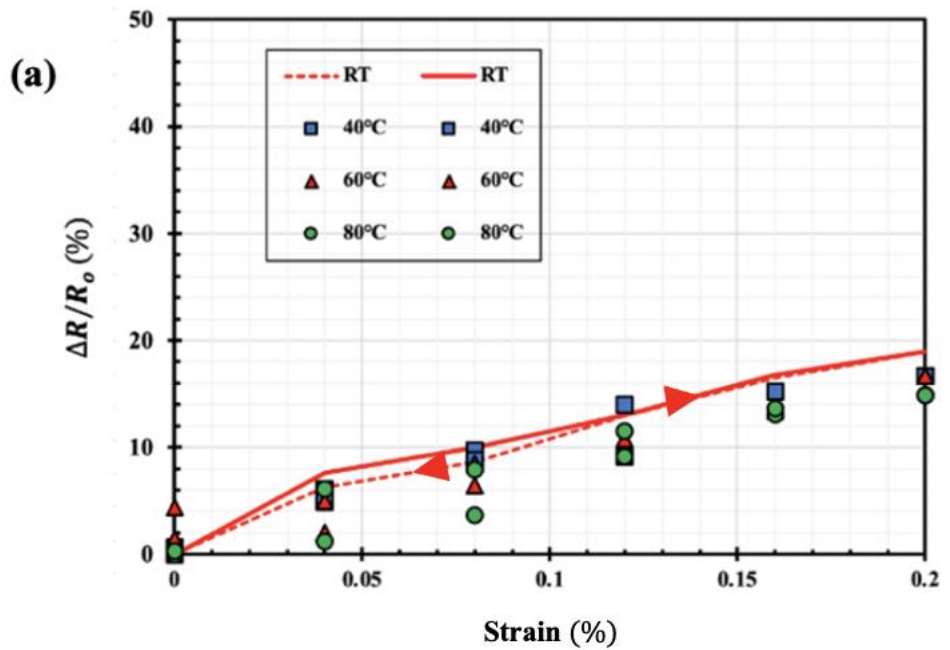
4.4 Strain/Temperature combination results

This section shows the behavior of BP in response to combined strain and temperature. To determine the effects properly, the used criteria was to measure one variable at a time.

(a) and

(b) show the load vs. resistance relation at four different temperatures, namely Room Temperature (RT), 40°C, 60°C, and 80°C for A0, C0, and A100, C10 respectively. It can be observed that the normalized change in resistance exhibits a linear reversible relation with the load. In addition, it can be observed that the BP sensor becomes less sensitive to strain as temperature increases. This deterioration may be due to the excitation of electrons and moving from the valence band to the conduction band leading to decreasing the resistivity of the sensor [108].

Figure 4.4 shows temperature vs. resistance by adding loads that are equally spaced. For instance: no load, 25g, 50g, and 75g. It is worth noting that the applied treatments, annealing (A) and compaction (C), positively impacted the GF value in both scenarios. According to a study led by et Johnson *et al.* [81], thermal annealing improves the thermal and electrical properties of CNTs, as explained earlier. It is also observed that the change in resistance of the control sample at any load remains constant. Conversely, it exhibits higher sensitivity in the treated sample, which agrees with the literature that applying treatments to BP significantly enhances the thermal properties [81].



: Effect of cyclic loading at different temperature points going up from room temperature up to 80°C. (a) represents (A0, C0) and (b) represents (A100, C10). The test was done on a stainless-steel beam. The Solid line represents the loading cycle and the dotted line represents the unloading cycle.

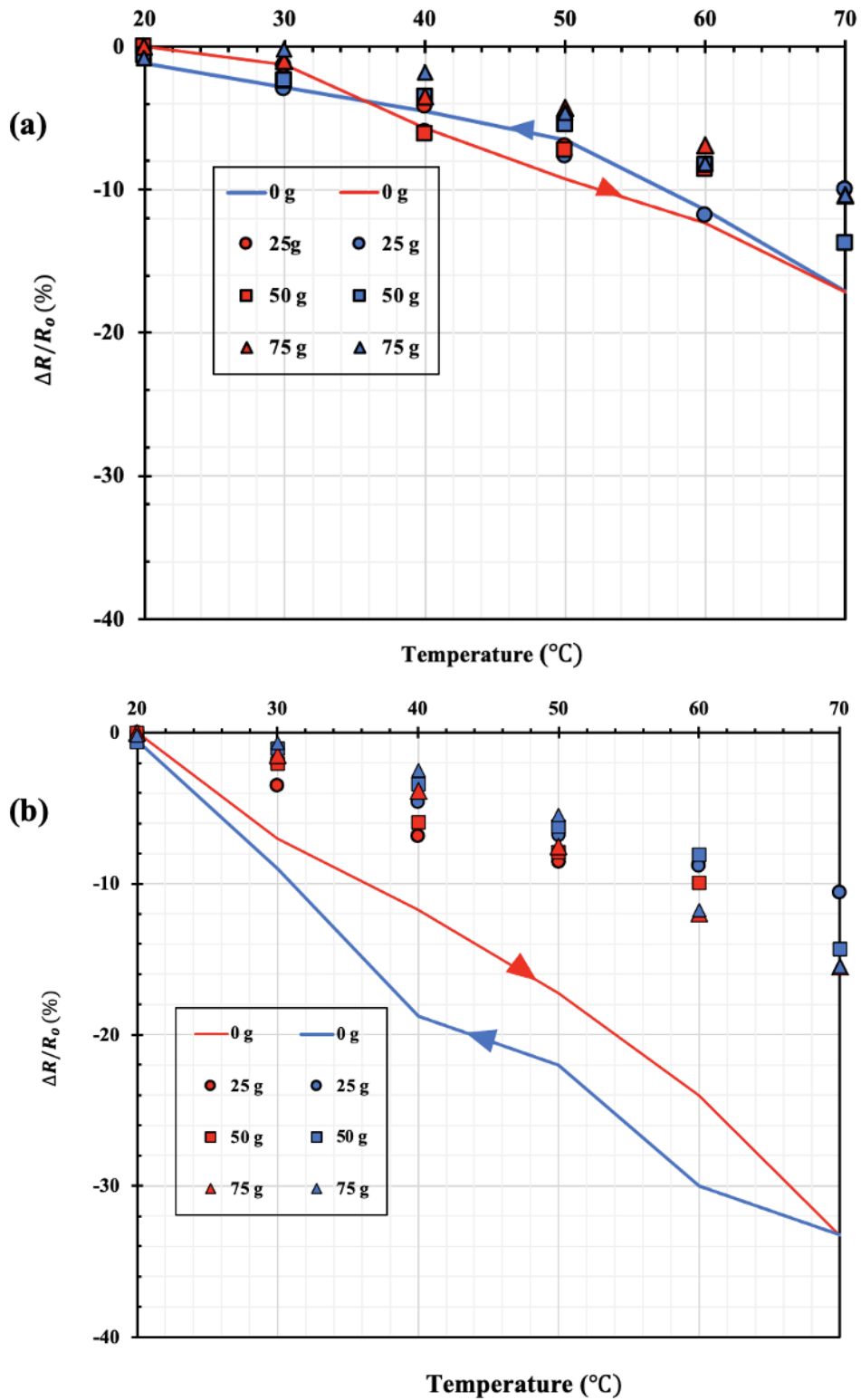


Figure 4.4: Effect of thermal cycling on BP-based temperature sensor with adding constant loads: 25g, 50g, and 75g. (a) the control sample (A0, C0) and (b) the treated sample (A100, C10).

4.5 SEM Results

It can be observed that the treated sample (A100, C10) shown in Figure 4.5 (b) has a denser structure with a more closely packed nanotube structure than the untreated sample (A0, C0) shown in Figure 4.6 (a), which shows larger pores.

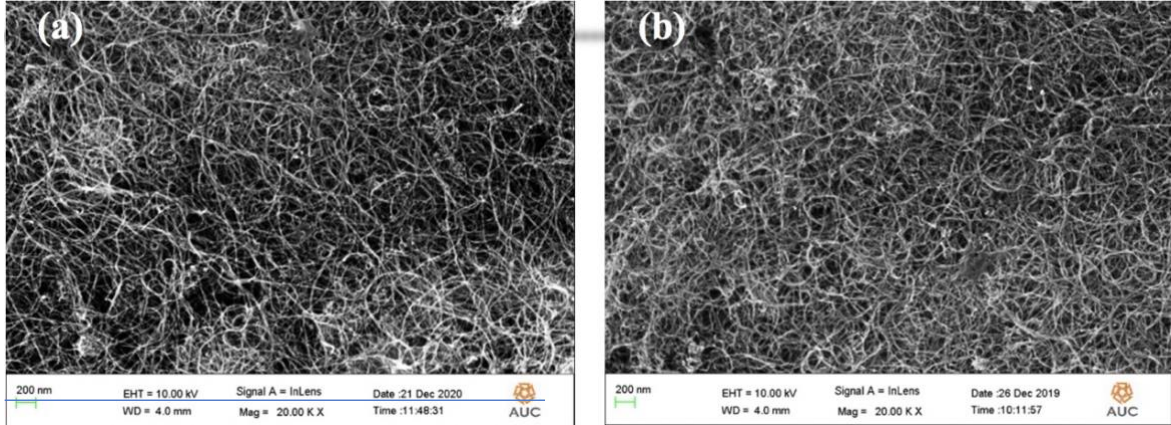


Figure 4.5: BP morphology using SEM. (a) (A0, C0) at 20 KX magnification scale, (b) (A100, C10).

4.6 Tensile Stage Results

4.6.1 Force-Displacement Graphs

The force-displacement curve demonstrated in Figure 4.6 is very beneficial in showing the mechanical properties of the proposed sensor. Moreover, using this curve, a quantitative comparison can be done with samples of different combinations of treatments. Figure 4.6 (a) represents the untreated sample (A0, C0), and Figure 4.6 (b) represents (A100, C10).

It can be shown that the treated sample has a significantly higher elongation at break value of $900 \mu\text{m}$ compared to the control sample, which failed at $250 \mu\text{m}$. This result agrees with the mechanical tensile testing results illustrated earlier in the subsection 4.2.1. Figure 4.6 also revealed that the BP can withstand a strain up to 9% before failure, which is much higher than the used maximum strain value in the cantilever testing setup.

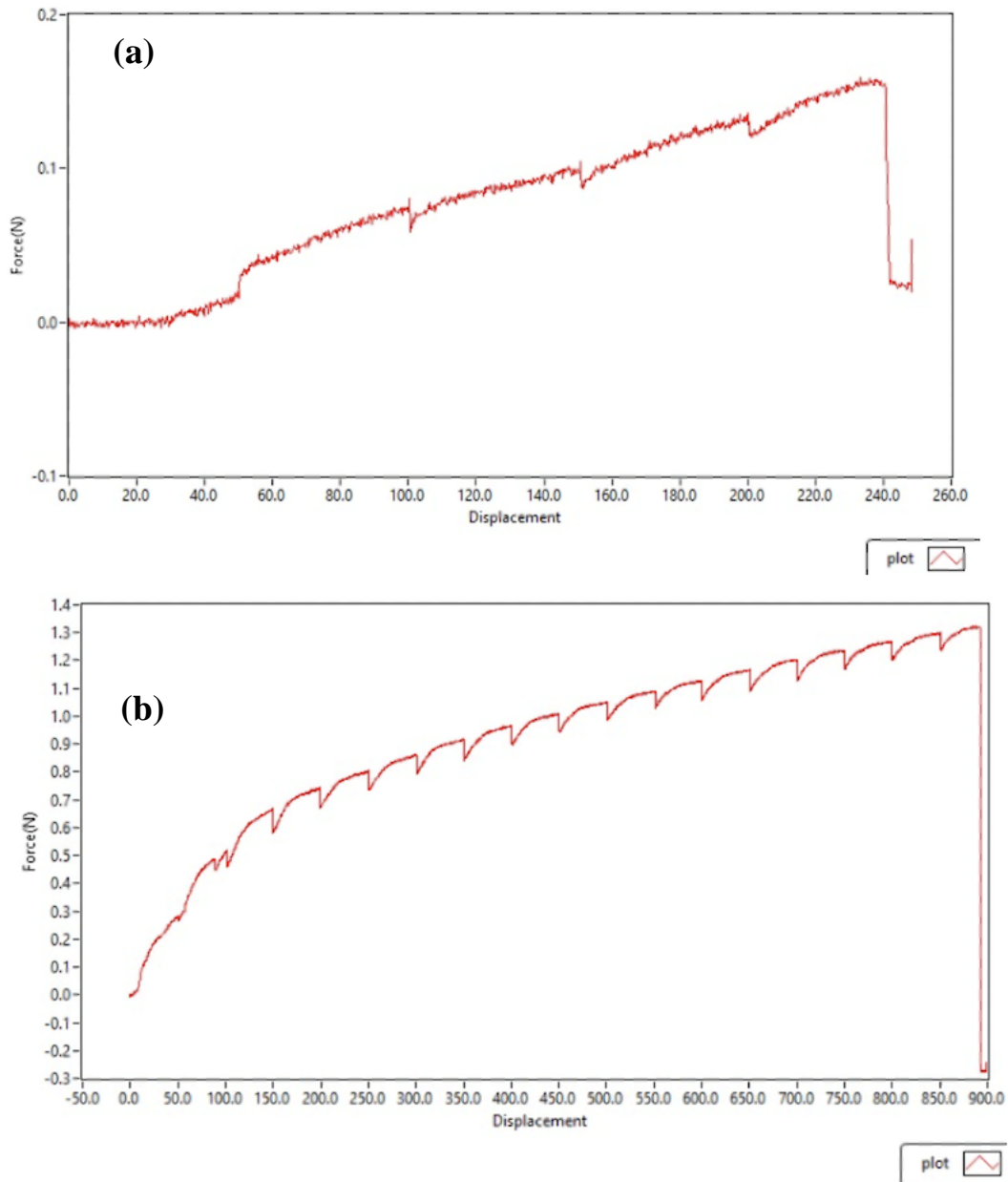


Figure 4.6: The force-displacement graphs generated from the tensile stage software plot of (a) (A0, C0) and (b) (A100, C10).

4.6.2 Quasi-static Loading/Unloading Graphs

Figure 4.7 shows the repetitive loading/unloading cycles with several load increments for the control sample. It can be clearly shown that the hysteresis area has a direct proportionality to the subjected load. In other words, the hysteresis area increases as the applied load increases. In addition, in the unloading cycles, the sample cannot retain the original length. It was found that the networks of BP become unfolded as a result of the applied tensile loading [62].

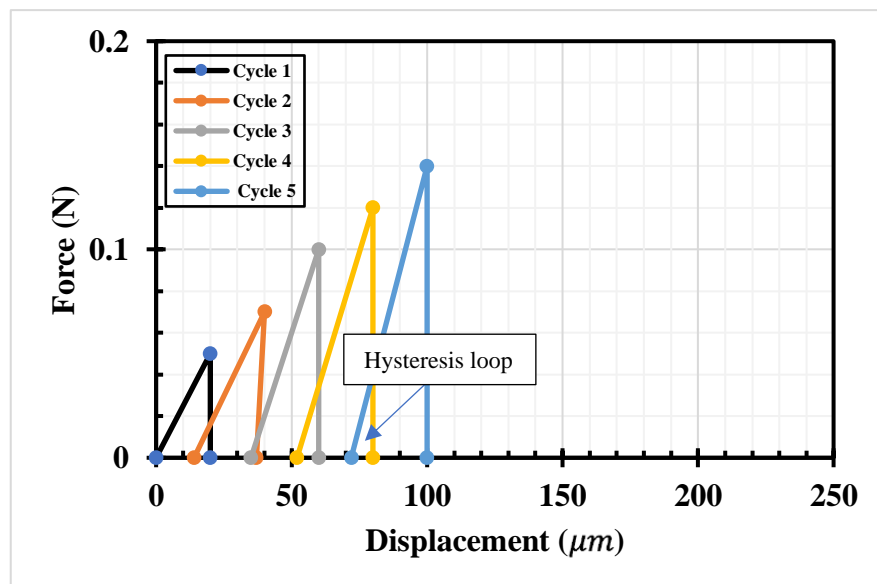


Figure 4.7: Cyclic loading - 5 loading/unloading cycles of the control sample.

4.6.3 Fracture Morphology

Figure 4.8 represents the fracture morphology of CNTs during the in-situ tensile loading using a 50N load cell. Figure 4.8 (a) and (c) illustrate the control sample (A0, C0) at different magnification scales, 5 KX and 20 KX, respectively. While Figure 4.8 (b) and (d) represent (A100, C10). These images were obtained by the tensile stage during the in-situ tensile loading. It can be clearly shown that CNTs are straightened.

This observation is supported by a previous study [109]. According to Jin *et al.* [109], when CNTs are subjected to in-situ tensile strain, the CNTs straightened and reoriented according to the applied strain direction. Additionally, the treated sample shows a highly entangled microstructure compared to the control sample.

According to Behler *et al.* [102], subjecting CNTs to annealing improves their electrical and thermal properties by eliminating the existing initial wall defects. Yoann *et al.* [104] showed that the CNTs transport properties are significantly enhanced by annealing. Also, the structure of the treated sample showed a better alignment as well as a denser structure.

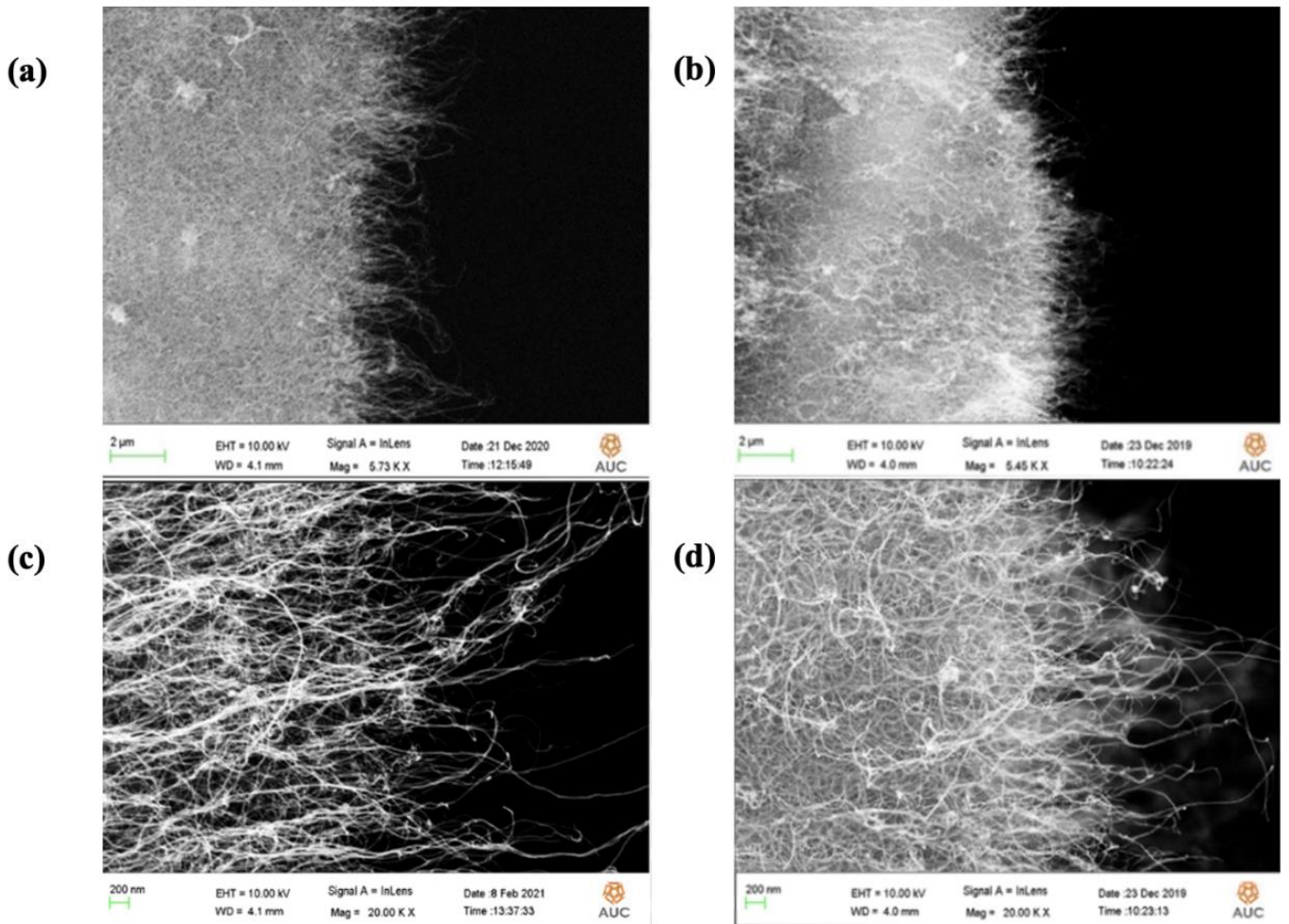


Figure 4.8: Fracture morphology of the control sample and the treated sample. (a) A0, C0 at 5 kX magnification scale, (b) A100, C10, (c) A0, C0 at higher magnification scale, and (d) A100, C10.

5.1 Summary and Conclusions

The thesis intends to evaluate and improve the strain and temperature sensitivities of MWCNT thin films (buckypaper) by applying a combination of treatments. Buckypaper samples were fabricated using the vacuum filtration technique and sonicated using the low-temperature method. They were then subjected to the treatments according to the desired level. The proposed treatments were annealing (A), exposure to boiling solvent (B), and compaction (C). Each treatment had three different levels, and each combination of treatments had three replicates to ensure the accuracy and repeatability of the results.

A series of experimental procedures was applied to detect the change in resistance in response to the applied strain/temperature. The characterization techniques include mechanical loading-unloading, thermal heating-cooling, SEM, and the fracture morphology resulting from the tensile stage inside the SEM.

Regarding the BP acting as a strain sensor, which was studied extensively by testing 81 samples, the results showed a potential to be used instead of the conventional strain gages thanks to the high sensitivity quantified by GF value that can reach up to roughly 180 for treated BPs.

Statistical analysis was performed using the Design-Expert software to observe the most influential combination of treatments. According to the software, it was observed that combining annealing with compaction had the highest influence on the strain sensitivity quantified by GF values that can reach up to 180.

Regarding the BP acting as a temperature sensor, it was observed that resistance decreases as temperature goes up. This can be due to the gained thermal energy by the valence electrons. This energy is transmitted to a kinetic energy which enables the electrons to cross the potential barrier easily. Regarding the combined effect of strain and temperature, it was observed that the BP exhibit a lower strain sensitivity when subjected to a heat source.

The BP morphology was tested, and the treated sample showed a denser closely packed structure which agrees with the experimental results. In addition, the BP tested using the tensile stage inside the SEM demonstrated a higher elongation at break value for the treated sample as compared to the control sample.

5.2 Recommendations

There are some recommendations to be considered for further investigations in this research that may be beneficial for the current knowledge, such as:

- Study the effect of aspect ratio on the sensitivity of the buckypaper.
- Test sensors that are produced by other techniques such as the tape casting technique, which allow larger sensors to be produced.
- Apply Monte Carlo simulation to detect the response of the BP under different loading values [110].
- Further investigations for the buckypaper-based temperature sensors with a wider range of temperature points, including the sub-zero region.
- Perform a thermogravimetric analysis (TGA) to the samples.
- Investigate a higher level of treatments, the positive treatments, to further enhance the BP sensitivity.

REFERENCES

- [1] Avent.com, “Piezoresistive Pressure Sensors | The Design Engineer’s Guide | Avnet Abacus.” .
- [2] P. Knowledge and P. Guide, “Wheatstone Bridge Overview,” pp. 1–12, 1865.
- [3] A. S. Devyatisil’nyi, “Mechanical measurements,” *Meas. Tech.*, vol. 47, no. 10, pp. 991–993, 2004, doi: 10.1007/s11018-005-0008-1.
- [4] J. Zhao, G. Y. Zhang, and D. X. Shi, “Review of graphene-based strain sensors,” *Chinese Phys. B*, vol. 22, no. 5, 2013, doi: 10.1088/1674-1056/22/5/057701.
- [5] “Temperature Sensors: Types, How It Works, & Applications | by Encardio rite | Medium.” <https://encardio.medium.com/temperature-sensors-types-how-it-works-applications-cac9305a14e3> (accessed Apr. 14, 2021).
- [6] “4 Most Common Types of Temperature Sensor | Ametherm.” <https://www.ametherm.com/blog/thermistors/temperature-sensor-types> (accessed Apr. 14, 2021).
- [7] H. H. M. Van Tol, “© 1991 Nature Publishing Group 그래첼꺼,” *Nature*, vol. 354, pp. 56–58, 1991.
- [8] R. Purohit, K. Purohit, S. Rana, R. S. Rana, and V. Patel, “Carbon Nanotubes and Their Growth Methods,” *Procedia Mater. Sci.*, vol. 6, no. Icmpc, pp. 716–728, 2014, doi: 10.1016/j.mspro.2014.07.088.
- [9] W. Obitayo and T. Liu, “A review: Carbon nanotube-based piezoresistive strain sensors,” *J. Sensors*, vol. 2012, 2012, doi: 10.1155/2012/652438.
- [10] G. Yin, N. Hu, Y. Karube, Y. Liu, Y. Li, and H. Fukunaga, “A carbon nanotube/polymer strain sensor with linear and anti-symmetric piezoresistivity,” *J. Compos. Mater.*, vol. 45, no. 12, pp. 1315–1323, 2011, doi:

10.1177/0021998310393296.

- [11] N. Hu *et al.*, “Investigation on sensitivity of a polymer/carbon nanotube composite strain sensor,” *Carbon N. Y.*, vol. 48, no. 3, pp. 680–687, 2010, doi: 10.1016/j.carbon.2009.10.012.
- [12] S. Iijima and T. Ichihashi, “Single-shell carbon nanotubes of 1-nm diameter,” *Nature*, vol. 363, no. 6430, pp. 603–605, 1993, doi: 10.1038/363603a0.
- [13] A. Eatemadi *et al.*, “Carbon nanotubes: Properties, synthesis, purification, and medical applications,” *Nanoscale Res. Lett.*, vol. 9, no. 1, pp. 1–13, 2014, doi: 10.1186/1556-276X-9-393.
- [14] Michael F. L.; De Volder, Sameh H.; Tawfick, Ray H.; Baughman, and A. John ;Hart, “Carbon Nanotubes: Present and Future Commercial Applications,” *Science (80-.)*, vol. 339, no. 6119, pp. 535–539, 2013, [Online]. Available: <http://science.sciencemag.org/content/339/6119/535?sid=599bece0-48b5-4fcc-9d21-5e29be89422c>.
- [15] P. R. Bandaru, “Electrical properties and applications of carbon nanotube structures,” *J. Nanosci. Nanotechnol.*, vol. 7, no. 4–5, pp. 1239–1267, 2007, doi: 10.1166/jnn.2007.307.
- [16] H. Qiu and J. Yang, *Structure and Properties of Carbon Nanotubes*, no. 2. Elsevier Inc., 2017.
- [17] H. Dai, E. W. Wong, and C. M. Liebert, “Probing Electrical Transport in Nanomaterials : Conductivity of Individual Carbon Nanotubes Author (s): Hongjie Dai , Eric W . Wong and Charles M . Lieber Published by : American Association for the Advancement of Science Stable URL : <http://www.jstor.o>,” vol. 272, no. 5261, pp. 523–526, 2017.
- [18] E. Pop *et al.*, “Thermal conductance of an individual single-wall carbon

- nanotube above room temperature,” *Nano Lett.*, vol. 84, no. 1, pp. 5552–5555, 2000, doi: 10.1021/nl052145f.
- [19] K. Kamaras and M. E. Itkis, “Covalent Bond Formation to a,” vol. 301, no. October, 2003.
- [20] H. I. Kim *et al.*, “Tensile properties of millimeter-long multi-walled carbon nanotubes,” *Sci. Rep.*, vol. 7, no. 1, pp. 1–7, 2017, doi: 10.1038/s41598-017-10279-0.
- [21] M. F. Yu, O. Lourie, M. J. Dyer, K. Moloni, T. F. Kelly, and R. S. Ruoff, “Strength and breaking mechanism of multiwalled carbon nanotubes under tensile load,” *Science (80-.)*, vol. 287, no. 5453, pp. 637–640, 2000, doi: 10.1126/science.287.5453.637.
- [22] E. W. Wong, P. E. Sheehan, and C. M. Liebert, “Nanobeam Mechanics : Elasticity , Strength , and Toughness of Nanorods and Nanotubes Author (s): Eric W . Wong , Paul E . Sheehan and Charles M . Lieber Published by : American Association for the Advancement of Science Stable URL : <http://www.jstor.org>,” vol. 277, no. 5334, pp. 1971–1975, 2016.
- [23] B. I. Yakobson, C. J. Brabec, and J. Bernholc, “Nanomechanics of carbon tubes: Instabilities beyond linear response,” *Phys. Rev. Lett.*, vol. 76, no. 14, pp. 2511–2514, 1996, doi: 10.1103/PhysRevLett.76.2511.
- [24] S. Xie, W. Li, Z. Pan, B. Chang, and S. Lianfeng, “Mechanical and physical properties on carbon nanotube,” *J. Phys. Chem. Solids*, vol. 61, no. 7, pp. 1153–1158, 2000, doi: 10.1016/S0022-3697(99)00376-5.
- [25] C. Li and T. W. Chou, “A structural mechanics approach for the analysis of carbon nanotubes,” *Int. J. Solids Struct.*, vol. 40, no. 10, pp. 2487–2499, 2003, doi: 10.1016/S0020-7683(03)00056-8.

- [26] C. F. Cornwell and L. T. Wille, “Elastic properties of single-walled carbon nanotubes in compression,” *Solid State Commun.*, vol. 101, no. 8, pp. 555–558, 1997, doi: 10.1016/S0038-1098(96)00742-9.
- [27] P. Pötschke, H. Brünig, A. Janke, D. Fischer, and D. Jehnichen, “Orientation of multiwalled carbon nanotubes in composites with polycarbonate by melt spinning,” *Polymer (Guildf)*, vol. 46, no. 23, pp. 10355–10363, 2005, doi: 10.1016/j.polymer.2005.07.106.
- [28] B. Schartel, P. Pötschke, U. Knoll, and M. Abdel-Goad, “Fire behaviour of polyamide 6/multiwall carbon nanotube nanocomposites,” *Eur. Polym. J.*, vol. 41, no. 5, pp. 1061–1070, 2005, doi: 10.1016/j.eurpolymj.2004.11.023.
- [29] K. Iakoubovskii, “Techniques of aligning carbon nanotubes,” *Cent. Eur. J. Phys.*, vol. 7, no. 4, pp. 645–653, 2009, doi: 10.2478/s11534-009-0072-2.
- [30] “Cross-sectional SEM image of the ~ 20- μ m-long, vertically aligned... | Download Scientific Diagram.” https://www.researchgate.net/figure/Cross-sectional-SEM-image-of-the-20-m-m-long-vertically-aligned-carbon-nanotubes_fig1_230608862 (accessed Jan. 04, 2021).
- [31] A. Li *et al.*, “Aligned carbon nanotube based sensors for strain sensing applications,” *Sensors Actuators, A Phys.*, vol. 289, no. 9, pp. 157–164, 2019, doi: 10.1016/j.sna.2019.02.026.
- [32] D. J. Yang *et al.*, “Thermal conductivity of multiwalled carbon nanotubes,” *Phys. Rev. B - Condens. Matter Mater. Phys.*, vol. 66, no. 16, pp. 1–6, 2002, doi: 10.1103/PhysRevB.66.165440.
- [33] J. Hone *et al.*, “Electrical and thermal transport properties of magnetically aligned single wall carbon nanotube films,” *Appl. Phys. Lett.*, vol. 77, no. 5, pp. 666–668, 2000, doi: 10.1063/1.127079.

- [34] B. Kumanek and D. Janas, “Thermal conductivity of carbon nanotube networks: a review,” *J. Mater. Sci.*, vol. 54, no. 10, pp. 7397–7427, 2019, doi: 10.1007/s10853-019-03368-0.
- [35] T. Yamamoto, Y. Nakazawa, and K. Watanabe, “Control of electron- And phonon-derived thermal conductances in carbon nanotubes,” *New J. Phys.*, vol. 9, 2007, doi: 10.1088/1367-2630/9/8/245.
- [36] X. Fu, C. Zhang, T. Liu, R. Liang, and B. Wang, “Carbon nanotube buckypaper to improve fire retardancy of high-temperature/high-performance polymer composites,” *Nanotechnology*, vol. 21, no. 23, 2010, doi: 10.1088/0957-4484/21/23/235701.
- [37] A. S. Lim, Q. An, T. W. Chou, and E. T. Thostenson, “Mechanical and electrical response of carbon nanotube-based fabric composites to Hopkinson bar loading,” *Compos. Sci. Technol.*, vol. 71, no. 5, pp. 616–621, 2011, doi: 10.1016/j.compscitech.2010.12.025.
- [38] M. José-Yacamán, M. Miki-Yoshida, L. Rendón, and J. G. Santiesteban, “Catalytic growth of carbon microtubules with fullerene structure,” *Appl. Phys. Lett.*, vol. 62, no. 6, pp. 657–659, 1993, doi: 10.1063/1.108857.
- [39] R. E. Smalley, “Crystalline Ropes of Metallic Carbon Nanotubes,” pp. 31–40, 1998, doi: 10.1007/978-3-662-03569-6_3.
- [40] L. Chico, V. H. Crespi, L. X. Benedict, S. G. Louie, and M. L. Cohen, “Pure carbon nanoscale devices: Nanotube heterojunctions,” *Phys. Rev. Lett.*, vol. 76, no. 6, pp. 971–974, 1996, doi: 10.1103/PhysRevLett.76.971.
- [41] J. Prasek *et al.*, “Methods for carbon nanotubes synthesis - Review,” *J. Mater. Chem.*, vol. 21, no. 40, pp. 15872–15884, 2011, doi: 10.1039/c1jm12254a.
- [42] J. Y. Oh *et al.*, “Easy preparation of self-assembled high-density buckypaper

with enhanced mechanical properties,” *Nano Lett.*, vol. 15, no. 1, pp. 190–197, 2015, doi: 10.1021/nl5033588.

- [43] “8.8: Strength of Covalent Bonds - Chemistry LibreTexts.”
[https://chem.libretexts.org/Bookshelves/General_Chemistry/Map%3A_Chemistry_-_The_Central_Science_\(Brown_et_al.\)/08._Basic_Concepts_of_Chemical_Bonding/8.8%3A_Strength_of_Covalent_Bonds](https://chem.libretexts.org/Bookshelves/General_Chemistry/Map%3A_Chemistry_-_The_Central_Science_(Brown_et_al.)/08._Basic_Concepts_of_Chemical_Bonding/8.8%3A_Strength_of_Covalent_Bonds) (accessed Jun. 02, 2021).
- [44] S. Potnis, “From carbon to buckypaper,” *Resonance*, vol. 22, no. 3, pp. 257–268, 2017, doi: 10.1007/s12045-017-0458-1.
- [45] J. E. Cha, S. Y. Kim, and S. H. Lee, “Effect of continuous multi-walled carbon nanotubes on thermal and mechanical properties of flexible composite film,” *Nanomaterials*, vol. 6, no. 10, 2016, doi: 10.3390/nano6100182.
- [46] I. Kang, M. J. Schulz, J. H. Kim, V. Shanov, and D. Shi, “A carbon nanotube strain sensor for structural health monitoring,” *Smart Mater. Struct.*, vol. 15, no. 3, pp. 737–748, 2006, doi: 10.1088/0964-1726/15/3/009.
- [47] W. Zhang, J. Suhr, and N. Koratkar, “Carbon nanotube/polycarbonate composites as multifunctional strain sensors,” *J. Nanosci. Nanotechnol.*, vol. 6, no. 4, pp. 960–964, 2006, doi: 10.1166/jnn.2006.171.
- [48] M. Amjadi and I. Park, “CARBON NANOTUBES-ECOFLEX NANOCOMPOSITE FOR STRAIN SENSING WITH ULTRA-HIGH STRETCHABILITY Department of Mechanical Engineering , Korea Advanced Institute of Science & Technology,” *Ieee Mems*, pp. 744–747, 2015.
- [49] G. Sapra, “Carbon Nanotube Bucky Paper Based Strain Sensor,” vol. 2, no. 4, pp. 289–292, 2015.
- [50] Alamusi, N. Hu, H. Fukunaga, S. Atobe, Y. Liu, and J. Li, “Piezoresistive

- strain sensors made from carbon nanotubes based polymer nanocomposites,” *Sensors*, vol. 11, no. 11, pp. 10691–10723, 2011, doi: 10.3390/s111110691.
- [51] S. M. Vemuru, R. Wahi, S. Nagarajaiah, and P. M. Ajayan, “Strain sensing using a multiwalled carbon nanotube film,” *J. Strain Anal. Eng. Des.*, vol. 44, no. 7, pp. 555–562, 2009, doi: 10.1243/03093247JSA535.
- [52] S. C. Her and W. C. Hsu, “Strain and temperature sensitivities along with mechanical properties of CNT Buckypaper sensors,” *Sensors (Switzerland)*, vol. 20, no. 11, 2020, doi: 10.3390/s20113067.
- [53] T. V. Sreekumar, T. Liu, S. Kumar, L. M. Ericson, R. H. Hauge, and R. E. Smalley, “Single-wall carbon nanotube films,” *Chem. Mater.*, vol. 15, no. 1, pp. 175–178, 2003, doi: 10.1021/cm020367y.
- [54] R. Duggal, F. Hussain, and M. Pasquali, “Self-assembly of single-walled carbon nanotubes into a sheet by drop drying,” *Adv. Mater.*, vol. 18, no. 1, pp. 29–34, 2006, doi: 10.1002/adma.200500625.
- [55] R. A. Susantyoko, Z. Karam, S. Alkhoori, I. Mustafa, C. H. Wu, and S. Almheiri, “A surface-engineered tape-casting fabrication technique toward the commercialisation of freestanding carbon nanotube sheets,” *J. Mater. Chem. A*, vol. 5, no. 36, pp. 19255–19266, 2017, doi: 10.1039/c7ta04999d.
- [56] M. D. Rein, O. Breuer, and H. D. Wagner, “Sensors and sensitivity: Carbon nanotube buckypaper films as strain sensing devices,” *Compos. Sci. Technol.*, vol. 71, no. 3, pp. 373–381, 2011, doi: 10.1016/j.compscitech.2010.12.008.
- [57] A. Lekawa-Raus, K. K. K. Koziol, and A. H. Windle, “Piezoresistive effect in carbon nanotube fibers,” *ACS Nano*, vol. 8, no. 11, pp. 11214–11224, 2014, doi: 10.1021/nn503596f.
- [58] J. Zhang, D. Jiang, H. X. Peng, and F. Qin, “Enhanced mechanical and

- electrical properties of carbon nanotube buckypaper by in situ cross-linking,” *Carbon N. Y.*, vol. 63, pp. 125–132, 2013, doi: 10.1016/j.carbon.2013.06.047.
- [59] F. Avilés *et al.*, “Influence of carbon nanotube on the piezoresistive behavior of multiwall carbon nanotube/polymer composites,” *J. Intell. Mater. Syst. Struct.*, vol. 27, no. 1, pp. 92–103, 2016, doi: 10.1177/1045389X14560367.
- [60] Y. Miao, L. Chen, Y. Lin, R. Sammynaiken, and W. J. Zhang, “On finding of high piezoresistive response of carbon nanotube films without surfactants for in-plane strain detection,” *J. Intell. Mater. Syst. Struct.*, vol. 22, no. 18, pp. 2155–2159, 2011, doi: 10.1177/1045389X11426179.
- [61] G. Dong Wang *et al.*, “Monitoring the drilling process of GFRP laminates with carbon nanotube buckypaper sensor,” *Compos. Struct.*, vol. 208, pp. 114–126, 2019, doi: 10.1016/j.compstruct.2018.10.016.
- [62] M. F. Arif, S. Kumar, and T. Shah, “Tunable morphology and its influence on electrical, thermal and mechanical properties of carbon nanostructure-buckypaper,” *Mater. Des.*, vol. 101, pp. 236–244, 2016, doi: 10.1016/j.matdes.2016.03.122.
- [63] J. Zhang, D. Jiang, and H. X. Peng, “A pressurized filtration technique for fabricating carbon nanotube buckypaper: Structure, mechanical and conductive properties,” *Microporous Mesoporous Mater.*, vol. 184, pp. 127–133, 2014, doi: 10.1016/j.micromeso.2013.10.012.
- [64] S. Shukrullah, N. M. Mohamed, M. S. Shaharun, and M. Yasar, “Study of surface morphology and alignment of MWCNTs grown by chemical vapor deposition,” vol. 1621, pp. 505–509, 2014, doi: 10.1063/1.4898513.
- [65] A. Li, A. E. Bogdanovich, and P. D. Bradford, “Aligned carbon nanotube sheet piezoresistive strain sensors,” *Smart Mater. Struct.*, vol. 24, no. 9, p. 95004,

2015, doi: 10.1088/0964-1726/24/9/095004.

- [66] A. Sanli, A. Benchirouf, C. Müller, and O. Kanoun, “Piezoresistive performance characterization of strain sensitive multi-walled carbon nanotube-epoxy nanocomposites,” *Sensors Actuators, A Phys.*, vol. 254, pp. 61–68, 2017, doi: 10.1016/j.sna.2016.12.011.
- [67] I. Lahiri, D. Lahiri, S. Jin, A. Agarwal, and W. Choi, “Carbon nanotubes: How strong is their bond with the substrate?,” *ACS Nano*, vol. 5, no. 2, pp. 780–787, 2011, doi: 10.1021/nn102900z.
- [68] E. Cagatay, A. Falco, A. Abdellah, and P. Lugli, “Carbon nanotube based temperature sensors fabricated by large-scale spray deposition,” *Conf. Proc. - 10th Conf. Ph. D. Res. Microelectron. Electron. PRIME 2014*, pp. 2–5, 2014, doi: 10.1109/prime.2014.6872731.
- [69] X. Wang, S. Lu, K. Ma, X. Xiong, H. Zhang, and M. Xu, “Tensile strain sensing of buckypaper and buckypaper composites,” *Mater. Des.*, vol. 88, pp. 414–419, 2015, doi: 10.1016/j.matdes.2015.09.035.
- [70] Z. Zhang, H. Wei, Y. Liu, and J. Leng, “Self-sensing properties of smart composite based on embedded buckypaper layer,” *Struct. Heal. Monit.*, vol. 14, no. 2, pp. 127–136, 2015, doi: 10.1177/1475921714568405.
- [71] K. S. Karimov, F. A. Khalid, and M. T. S. Chani, “Carbon nanotubes based strain sensors,” *Meas. J. Int. Meas. Confed.*, vol. 45, no. 5, pp. 918–921, 2012, doi: 10.1016/j.measurement.2012.02.003.
- [72] P. Dharap, Z. Li, S. Nagarajaiah, and E. V. Barrera, “Flexural strain sensing using carbon nanotube film,” *Sens. Rev.*, vol. 24, no. 3, pp. 271–273, 2004, doi: 10.1108/02602280410545399.
- [73] W. L. Wang, K. J. Liao, Y. Li, and Y. T. Wang, “Piezoresistive Effect of

- Doped carbon Nanotube/Cellulose Films,” *Chinese Phys. Lett.*, vol. 20, no. 9, pp. 1544–1547, 2003, doi: 10.1088/0256-307X/20/9/339.
- [74] G. Yang, L. Liu, and Z. Wu, “Improved strain sensing capability of nano-carbon free-standing buckypapers based strain gauges,” 2019.
- [75] K. S. S. Karimov, M. T. S. T. S. Chani, and F. A. A. Khalid, “Carbon nanotubes film based temperature sensors,” *Phys. E Low-Dimensional Syst. Nanostructures*, vol. 43, no. 9, pp. 1701–1703, 2011, doi: 10.1016/j.physe.2011.05.025.
- [76] “Cnt Based Sensor.Pdf.” .
- [77] B. F. Monea, E. I. Ionete, S. I. Spiridon, D. Ion-Ebrasu, and E. Petre, “Carbon nanotubes and carbon nanotube structures used for temperature measurement,” *Sensors (Switzerland)*, vol. 19, no. 11, 2019, doi: 10.3390/s19112464.
- [78] A. Saraiya, D. Porwal, A. N. Bajpai, N. K. Tripathi, and K. Ram, “Investigation of carbon nanotubes as low temperature sensors,” *Synth. React. Inorganic, Met. Nano-Metal Chem.*, vol. 36, no. 2, pp. 163–164, 2006, doi: 10.1080/15533170500524496.
- [79] C. Y. Kuo, C. L. Chan, C. Gau, C. W. Liu, S. H. Shiau, and J. H. Ting, “Nano temperature sensor using selective lateral growth of carbon nanotube between electrodes,” *IEEE Trans. Nanotechnol.*, vol. 6, no. 1, pp. 63–69, 2007, doi: 10.1109/TNANO.2006.888531.
- [80] S. Sarma and J. H. Lee, “Developing efficient thin film temperature sensors utilizing layered carbon nanotube films,” *Sensors (Switzerland)*, vol. 18, no. 10, pp. 1–10, 2018, doi: 10.3390/s18103182.
- [81] J. F. Niven, M. B. Johnson, S. M. Juckes, M. A. White, N. T. Alvarez, and V. Shanov, “Influence of annealing on thermal and electrical properties of carbon

- nanotube yarns,” *Carbon N. Y.*, vol. 99, pp. 485–490, 2016, doi: 10.1016/j.carbon.2015.12.014.
- [82] D. Tománek, A. Jorio, M. S. Dresselhaus, and G. Dresselhaus, “Introduction to the important and exciting aspects of carbon-nanotube science and technology,” *Top. Appl. Phys.*, vol. 111, no. 2008, pp. 1–12, 2008, doi: 10.1007/978-3-540-72865-8_1.
- [83] “Thomas Swan & Co. Ltd.” .
- [84] “volatility .,” vol. I, p. 1955, 1955, doi: 10.1021/ed032p291.1.
- [85] K. Jagadish, S. Srikantaswamy, K. Byrappa, L. Shruthi, and M. R. Abhilash, “Dispersion of Multiwall Carbon Nanotubes in Organic Solvents through Hydrothermal Supercritical Condition,” *J. Nanomater.*, vol. 2015, 2015, doi: 10.1155/2015/381275.
- [86] L. Dumée, K. Sears, J. Schütz, N. Finn, M. Duke, and S. Gray, “Influence of the Sonication Temperature on the Debundling Kinetics of Carbon Nanotubes in Propan-2-ol,” *Nanomaterials*, vol. 3, no. 1, pp. 70–85, 2013, doi: 10.3390/nano3010070.
- [87] L. Vaisman, H. D. Wagner, and G. Marom, “The role of surfactants in dispersion of carbon nanotubes,” *Adv. Colloid Interface Sci.*, vol. 128–130, no. 2006, pp. 37–46, 2006, doi: 10.1016/j.cis.2006.11.007.
- [88] L. Guadagno *et al.*, “properties of structural advanced materials Effect of dispersion method and CNT loading on the quality and performance of nanocomposite soy protein / CNTs adhesive for wood application.”
- [89] K. Yang, Z. L. Yi, Q. F. Jing, R. L. Yue, W. Jiang, and D. H. Lin, “Sonication-assisted dispersion of carbon nanotubes in aqueous solutions of the anionic surfactant SDBS: The role of sonication energy,” *Chinese Sci. Bull.*, vol. 58,

- no. 17, pp. 2082–2090, 2013, doi: 10.1007/s11434-013-5697-2.
- [90] “Chrom Tech | Chrom Tech, Inc.” <https://www.chromtech.com/chrom-tech#/pageSize=24&viewMode=grid&orderBy=0&pageNumber=3> (accessed Jan. 10, 2021).
- [91] J. Li and L. Fan, “An Experimental Study of Boiling Heat Transfer During Quenching,” *Proc. ASME 2016 Heat Transf. Summer Conf.*, pp. 1–7, 2016.
- [92] “Introduction to Design of Experiments (DOE)- DOE Types.” .
- [93] Y. Ge Yu *et al.*, “In-situ pressing synthesis of densely compacted carbon nanotubes reinforced nanocomposites with outstanding mechanical performance,” *Compos. Sci. Technol.*, vol. 146, pp. 131–138, 2017, doi: 10.1016/j.compscitech.2017.04.001.
- [94] I. S. T. Stage, “In-Situ Specimen Tensile Stage for EBSD TS-1500-III Instruction manual.”
- [95] “Fluke 15B+ Digital Multimeter | Fluke.” .
- [96] J. Bernholc, D. Brenner, M. Buongiorno Nardelli, V. Meunier, and C. Roland, “Mechanical and electrical properties of nanotubes,” *Annu. Rev. Mater. Sci.*, vol. 32, pp. 347–375, 2002, doi: 10.1146/annurev.matsci.32.112601.134925.
- [97] Y. Zare and K. Y. Rhee, “Formulation of tunneling resistance between neighboring carbon nanotubes in polymer nanocomposites,” *Eng. Sci. Technol. an Int. J.*, no. xxxx, 2020, doi: 10.1016/j.jestch.2020.11.002.
- [98] M. Danish and S. Luo, “A new route to enhance the packing density of buckypaper for superior piezoresistive sensor characteristics,” *Sensors (Switzerland)*, vol. 20, no. 10, 2020, doi: 10.3390/s20102904.
- [99] Y. Wang, Y. Wang, P. Zhang, F. Liu, and S. Luo, “Laser-Induced Freestanding Graphene Papers: A New Route of Scalable Fabrication with Tunable

Morphologies and Properties for Multifunctional Devices and Structures,”
Small, vol. 14, no. 36, pp. 1–9, 2018, doi: 10.1002/sml.201802350.

- [100] T. T. Tung, C. Pham-Huu, I. Janowska, T. Kim, M. Castro, and J. F. Feller, “Hybrid Films of Graphene and Carbon Nanotubes for High Performance Chemical and Temperature Sensing Applications,” *Small*, vol. 11, no. 28, pp. 3485–3493, 2015, doi: 10.1002/sml.201403693.
- [101] S. Dehghani, M. K. Moravvej-Farshi, and M. H. Sheikhi, “Temperature dependence of electrical resistance of individual carbon nanotubes and carbon nanotubes network,” *Mod. Phys. Lett. B*, vol. 26, no. 21, pp. 1–13, 2012, doi: 10.1142/S0217984912501369.
- [102] K. Behler, S. Osswald, H. Ye, S. Dimovski, and Y. Gogotsi, “Effect of thermal treatment on the structure of multi-walled carbon nanotubes,” *J. Nanoparticle Res.*, vol. 8, no. 5, pp. 615–625, 2006, doi: 10.1007/s11051-006-9113-6.
- [103] W. Huang, Y. Wang, G. Luo, and F. Wei, “99.9% Purity Multi-Walled Carbon Nanotubes By Vacuum High-Temperature Annealing,” *Carbon N. Y.*, vol. 41, no. 13, pp. 2585–2590, 2003, doi: 10.1016/S0008-6223(03)00330-0.
- [104] Y. Dini, D. Rouchon, J. Faure-Vincent, and J. Dijon, “Large improvement of CNT yarn electrical conductivity by varying chemical doping and annealing treatment,” *Carbon N. Y.*, vol. 156, pp. 38–48, 2020, doi: 10.1016/j.carbon.2019.09.022.
- [105] Y. K. Kwon and P. Kim, “Unusually high thermal conductivity in carbon nanotubes,” *High Therm. Conduct. Mater.*, pp. 227–265, 2006, doi: 10.1007/0-387-25100-6_8.
- [106] W. L. Tsai *et al.*, “Conductivity enhancement of multiwalled carbon nanotube thin film via thermal compression method,” *Nanoscale Res. Lett.*, vol. 9, no. 1,

pp. 1–6, 2014, doi: 10.1186/1556-276X-9-451.

- [107] A. I. Zhbanov, E. G. Pogorelov, and Y. C. Chang, “Van der Waals interaction between two crossed carbon nanotubes,” *ACS Nano*, vol. 4, no. 10, pp. 5937–5945, 2010, doi: 10.1021/nn100731u.
- [108] M. De Volder, D. Reynaerts, C. Van Hoof, S. Tawfick, and A. J. Hart, “A temperature sensor from a self-assembled carbon nanotube microbridge,” *Proc. IEEE Sensors*, pp. 2369–2372, 2010, doi: 10.1109/ICSENS.2010.5690868.
- [109] L. Jin *et al.*, “Microstructural origin of resistance-strain hysteresis in carbon nanotube thin film conductors,” *Proc. Natl. Acad. Sci. U. S. A.*, vol. 115, no. 9, pp. 1986–1991, 2018, doi: 10.1073/pnas.1717217115.
- [110] D. Mählich, O. Eberhardt, and T. Wallmersperger, “Numerical simulation of the mechanical behavior of a carbon nanotube bundle,” *Acta Mech.*, vol. 232, no. 2, pp. 483–494, 2021, doi: 10.1007/s00707-020-02874-6.

APPENDICES

The appendices section is divided into three sub-sections, appendix A, B, and C. the raw data of GF experiments and the loading/unloading graphs will be illustrated in Appendix A and B respectively. Furthermore, the numeric GF values will be demonstrated in appendix C.

Appendix A: Graphical representation of GF values

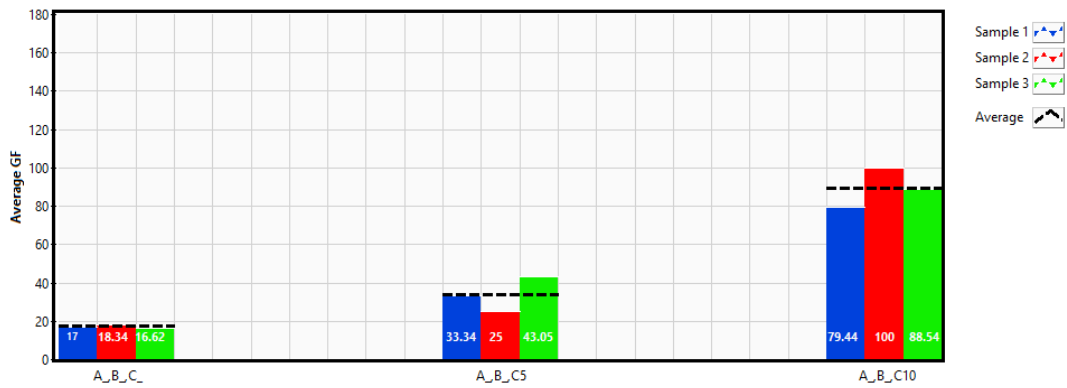


Figure A. 1: GF values of (A, B, C), (A, B, C5), and (A, B, C10).

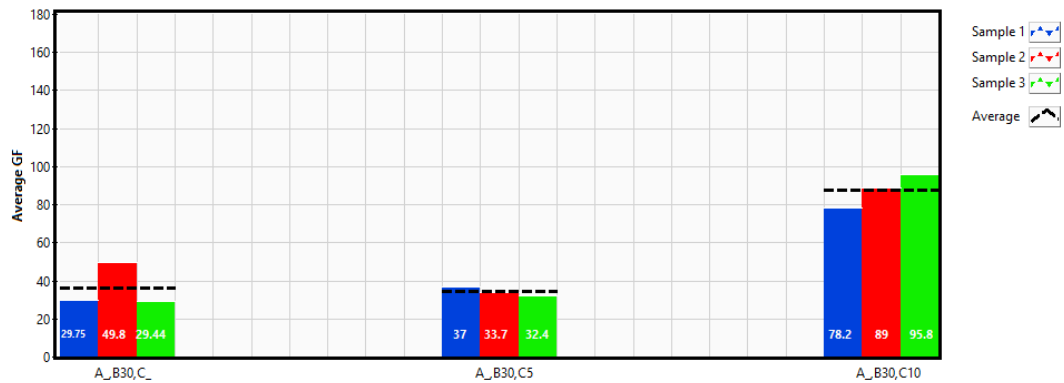


Figure A. 2: GF values of (A, B30, C), (A, B30, C5), and (A, B30, C10).

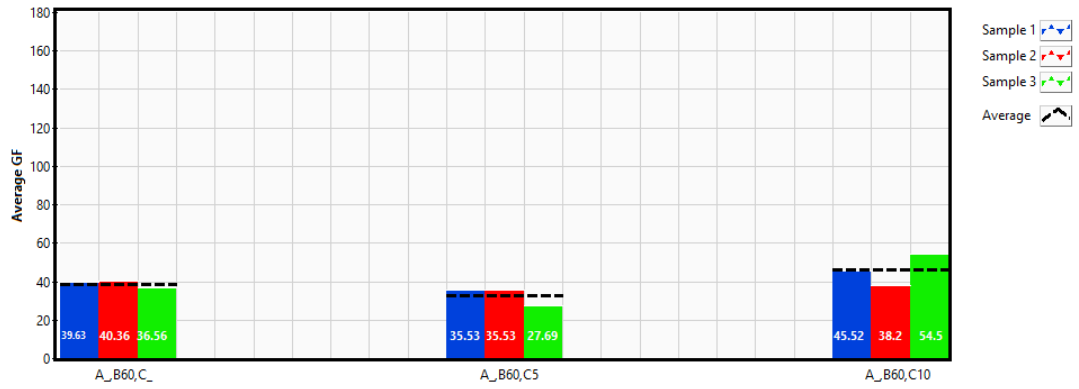


Figure A. 3: GF values of (A_, B60, C_), (A_, B60, C5), and (A_, B60, C10).

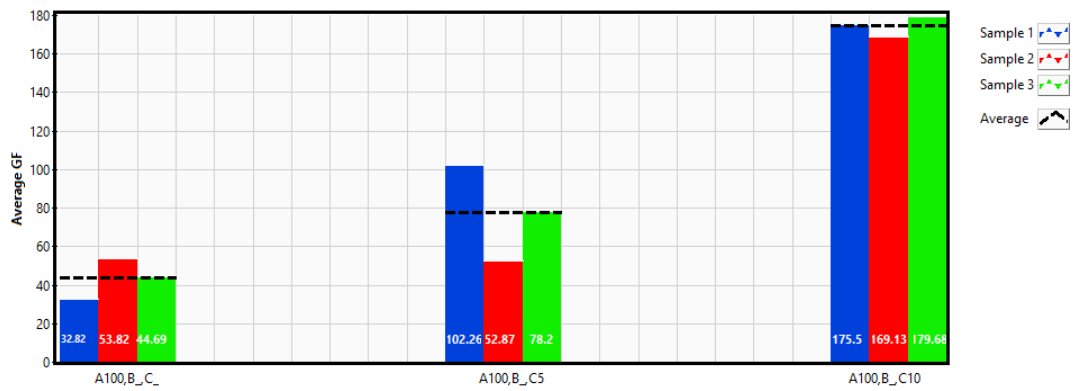


Figure A. 4: GF values of (A100, B_, C_), (A100, B_, C5), and (A100, B_, C10).

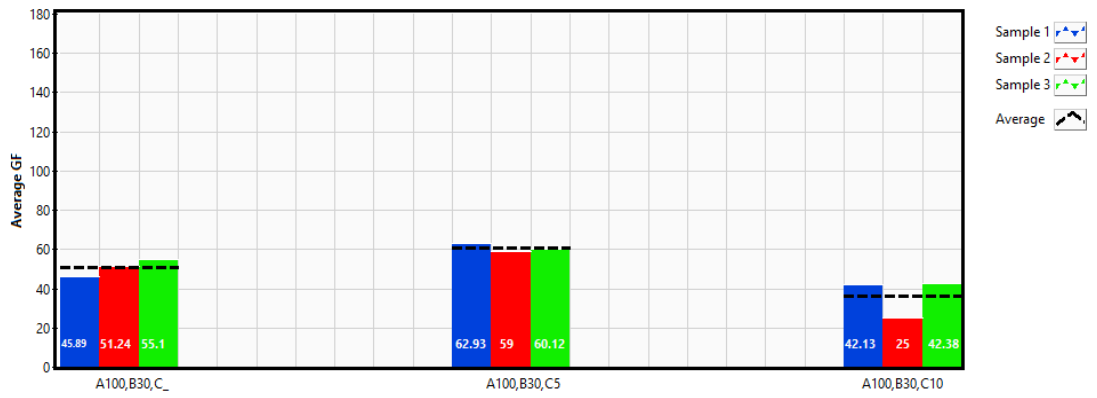


Figure A. 5: GF values of (A100, B30, C₋), (A100, B30, C5), and (A100, B30, C10).

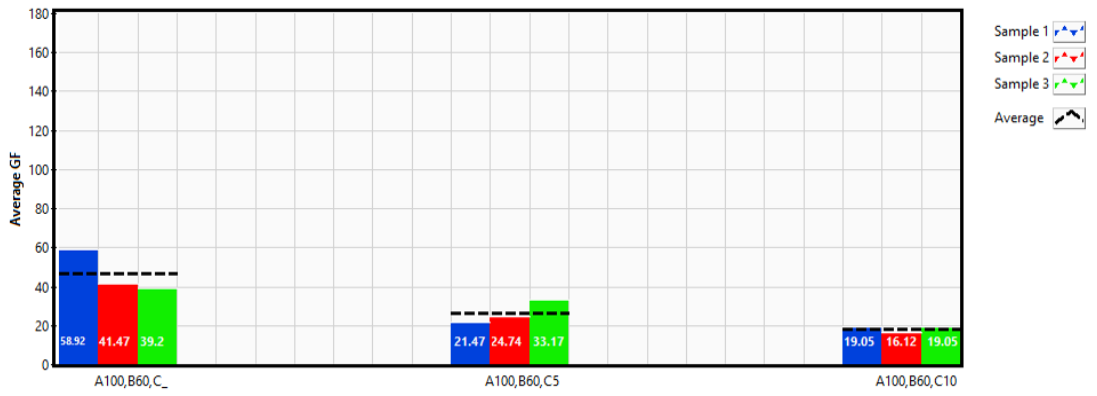


Figure A. 6: GF values of (A100, B60, C₋), (A100, B60, C5), and (A100, B60, C10).

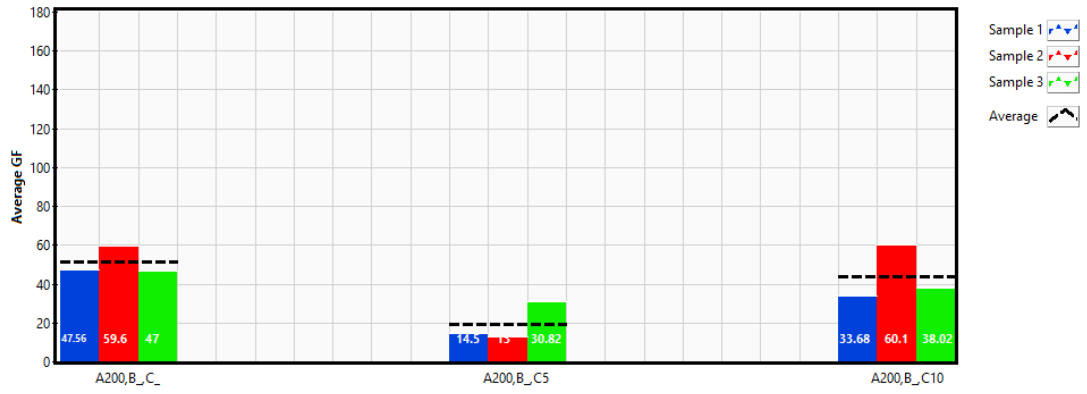


Figure A. 7: GF values of (A200, B_, C_), (A200, B_, C5), and (A200, B_, C10).

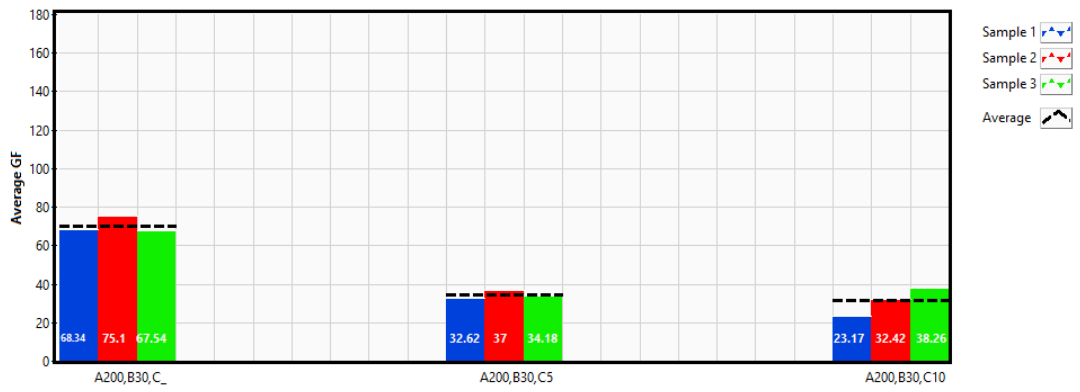


Figure A. 8: GF values of (A200, B30, C_), (A200, B30, C5), and (A200, B30, C10)

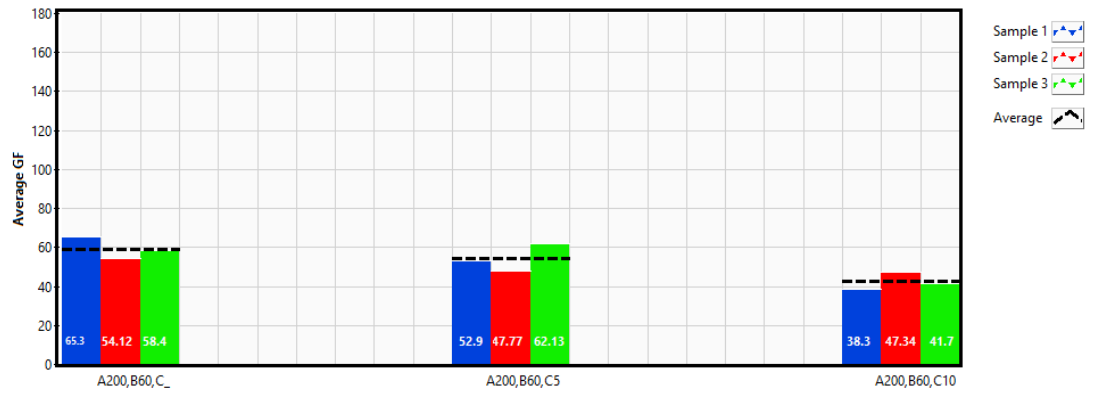


Figure A. 9: GF values of (A200, B60, C_), (A200, B60, C5), and (A200, B60, C10)

Appendix B: All loading/unloading graphs

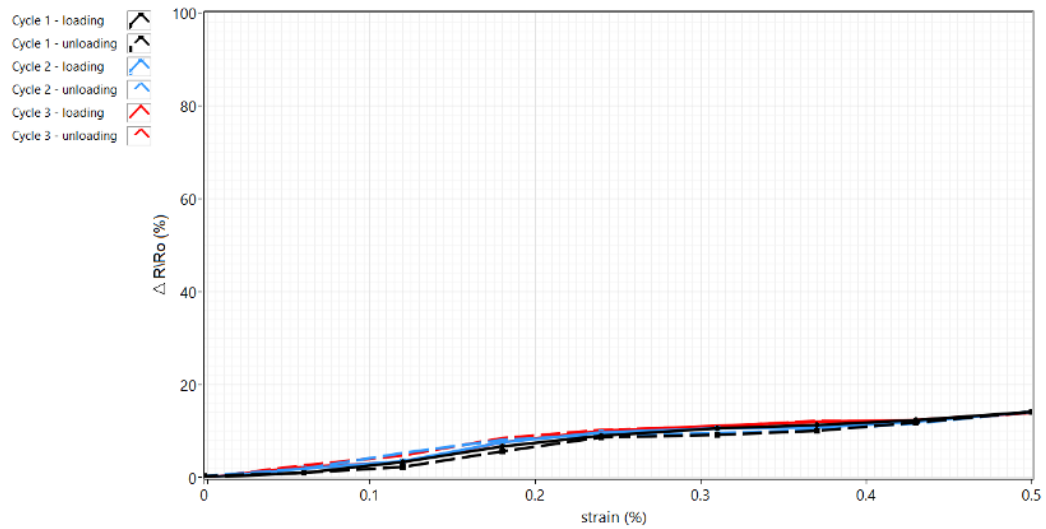


Figure B. 1: Three loading/unloading cycles of the sample (A_, B_, C5)

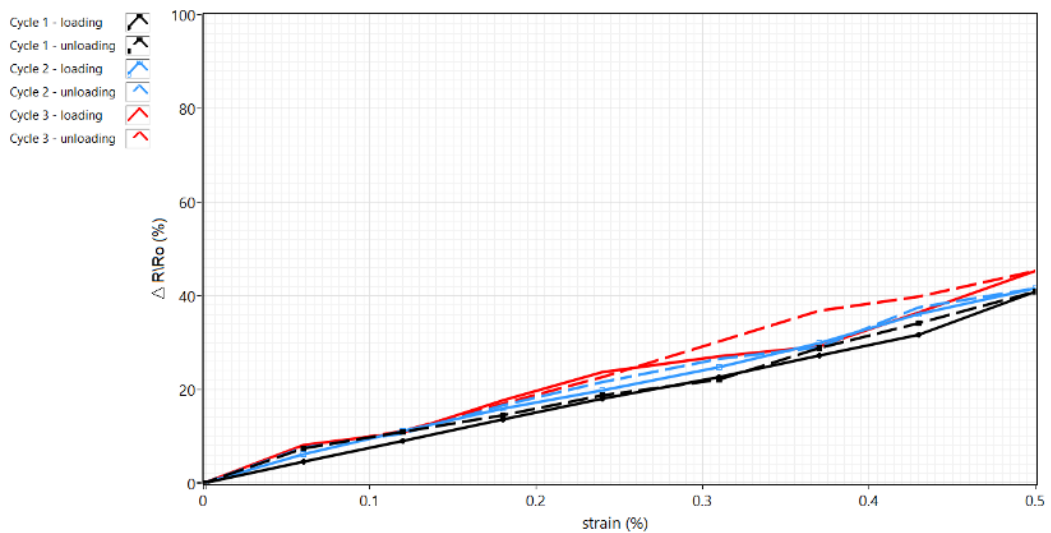


Figure B. 2: Three loading/unloading cycles of the sample (A_, B_, C10).

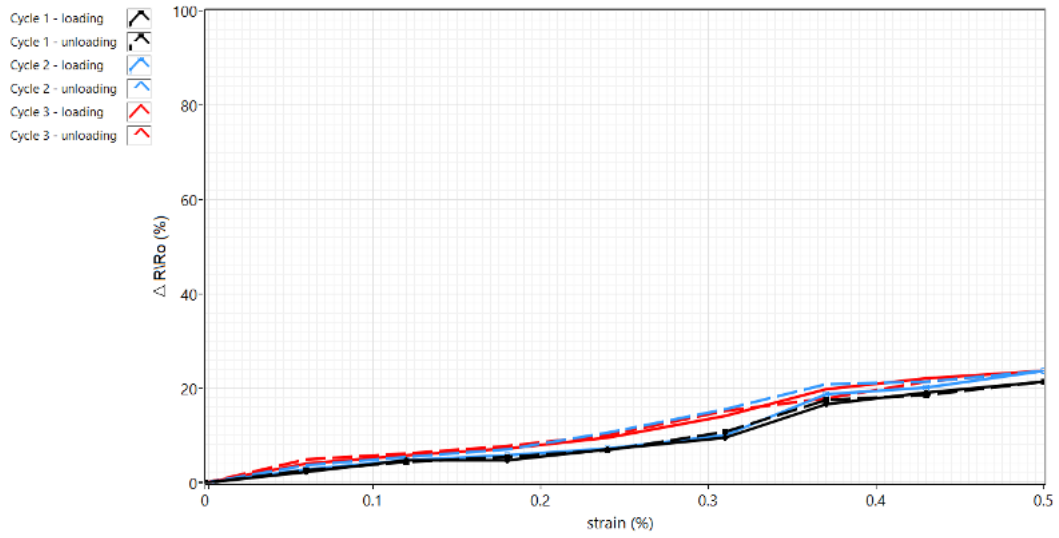


Figure B. 3: Three loading/unloading cycles of the sample (A_, B30, C_).

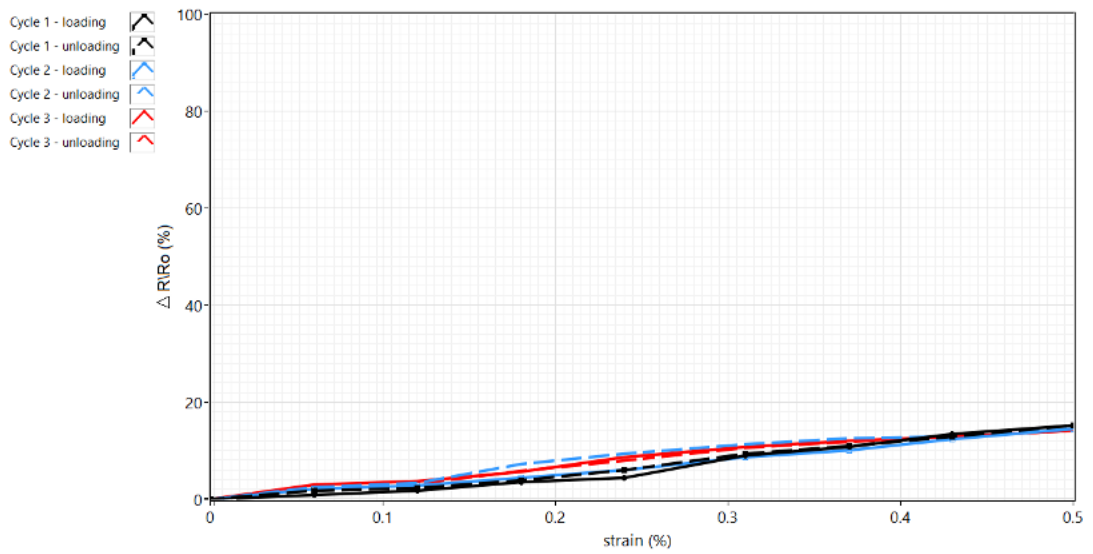


Figure B. 4: Three loading/unloading cycles of the sample (A_, B30, C5).

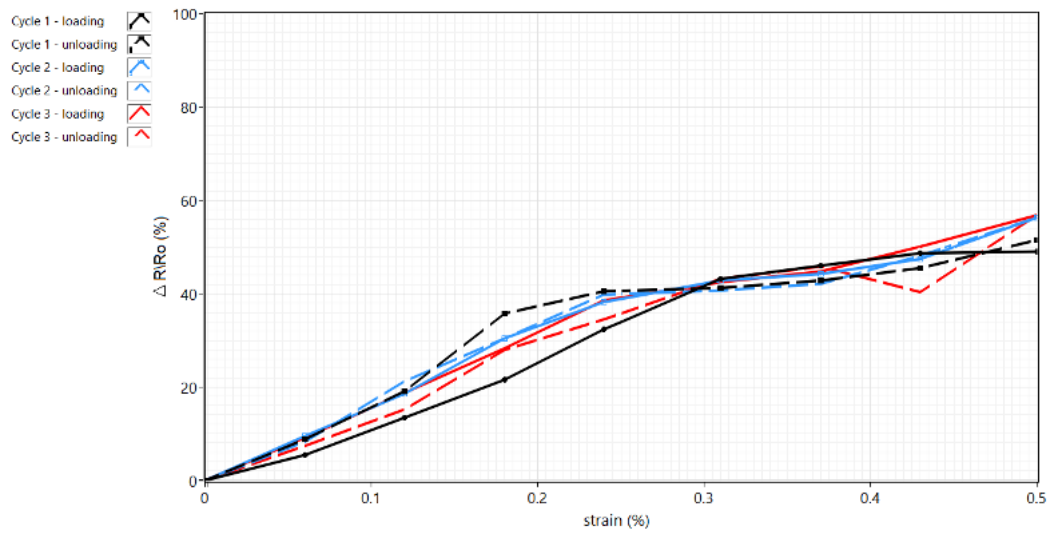


Figure B. 5: Three loading/unloading cycles of the sample (A_, B30, C10).

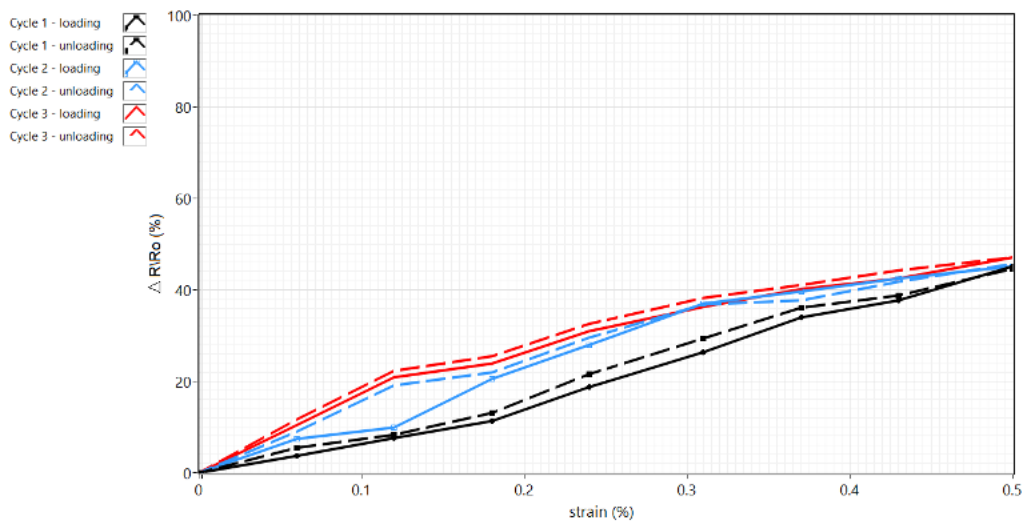


Figure B. 6: Three loading/unloading cycles of the sample (A_, B60, C_).

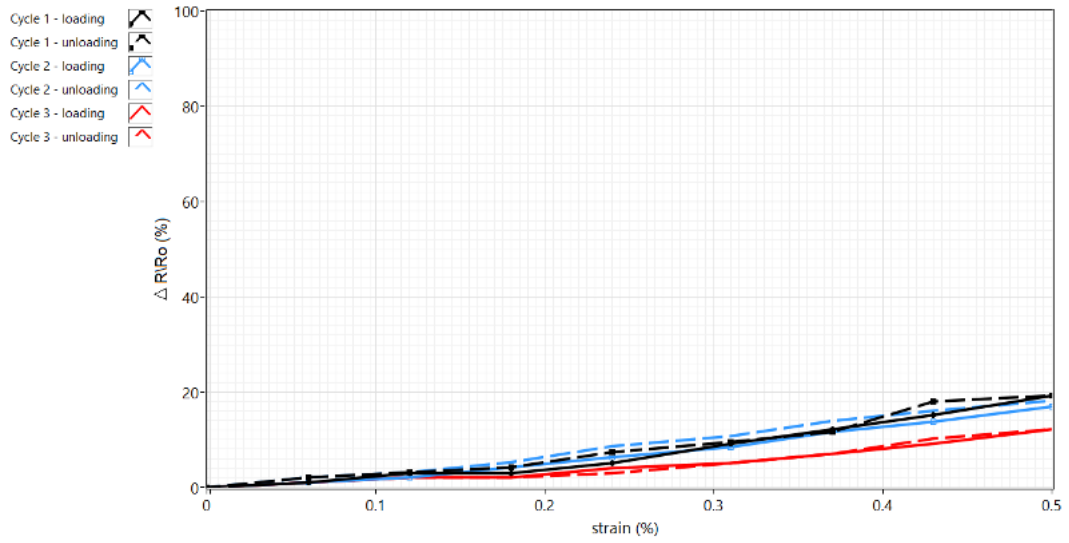


Figure B. 7: Three loading/unloading cycles of the sample (A_, B60, C5).

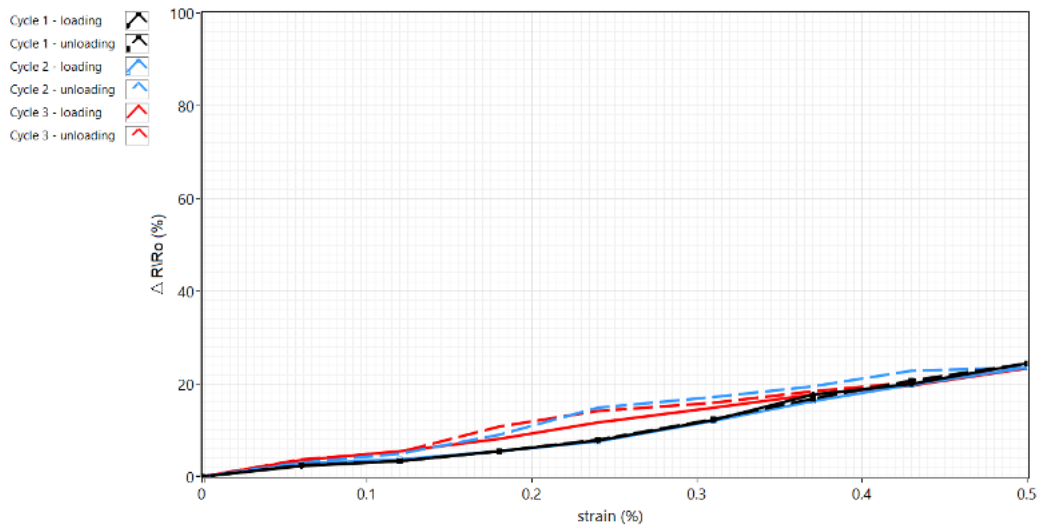


Figure B. 8: Three loading/unloading cycles of the sample (A_, B60, C10).

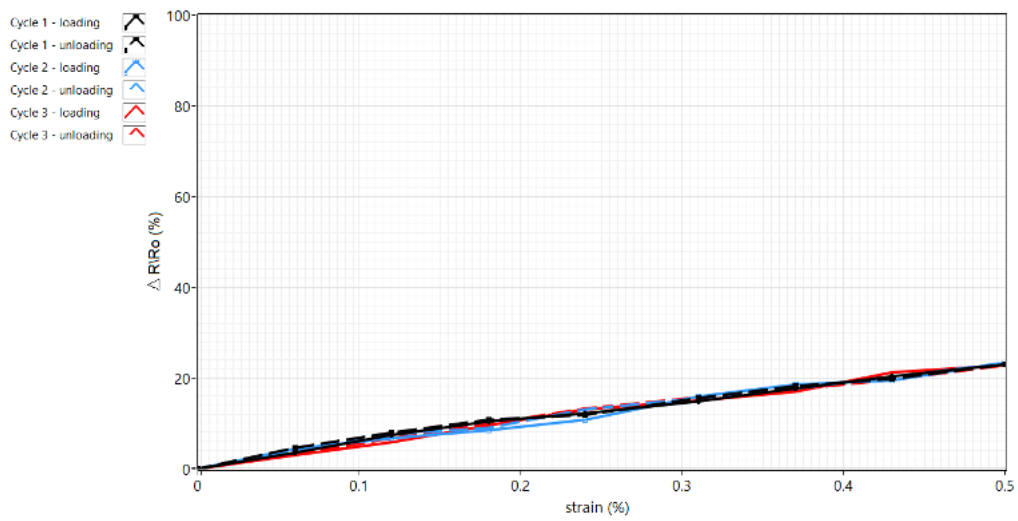


Figure B. 9: Three loading/unloading cycles of the sample (A100, B_, C_).

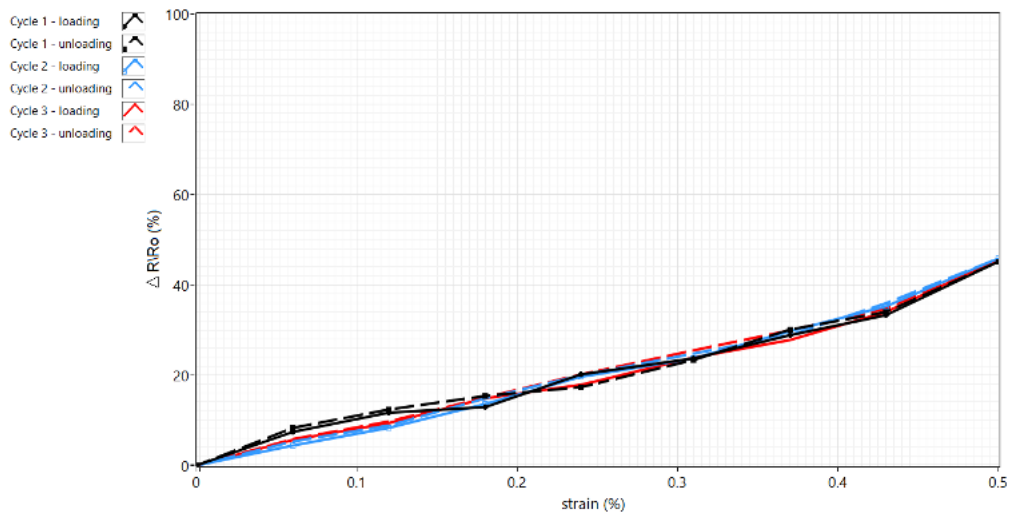


Figure B. 10: Three loading/unloading cycles of the sample (A100, B_, C5).

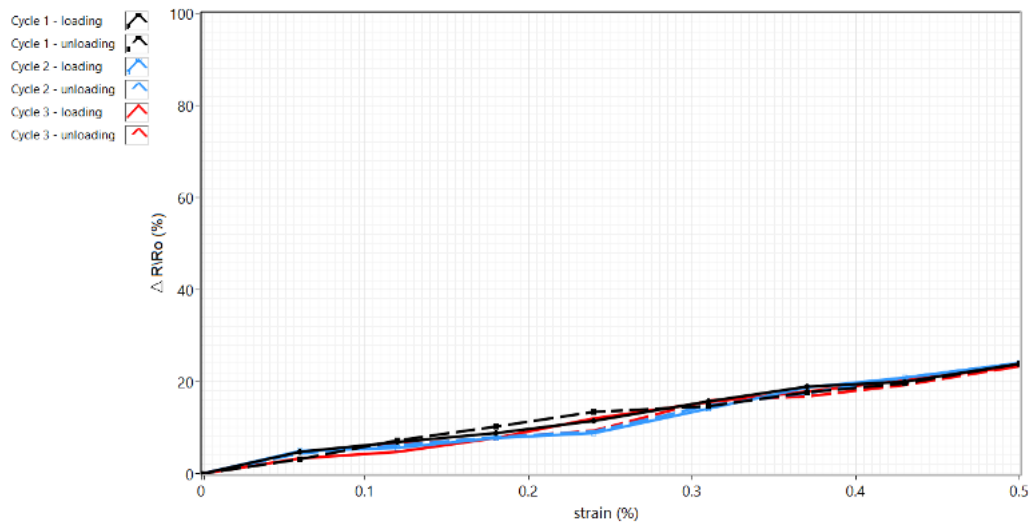


Figure B. 11: Three loading/unloading cycles of the sample (A100, B30, C_).

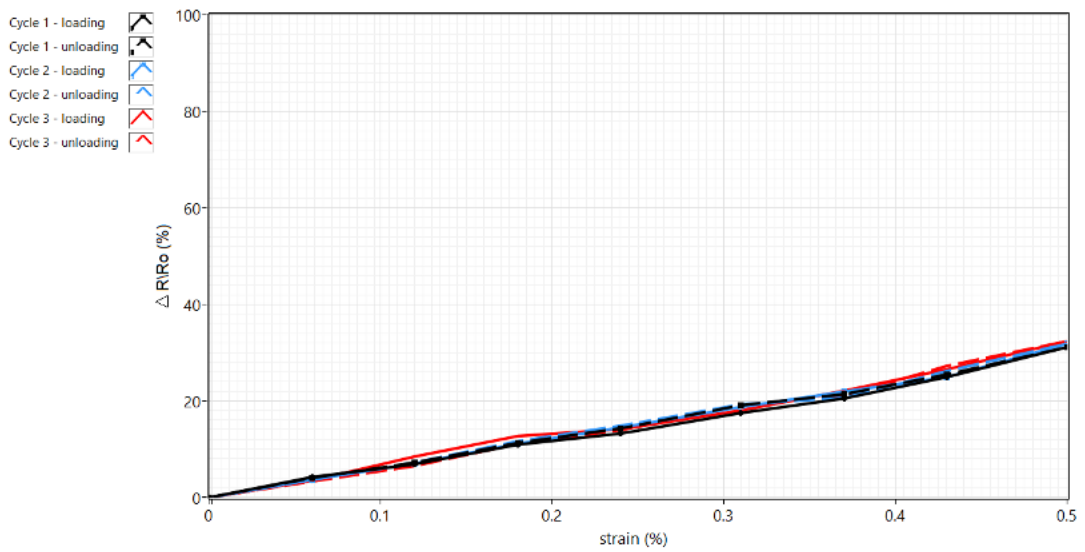


Figure B. 12: Three loading/unloading cycles of the sample (A100, B30, C5)

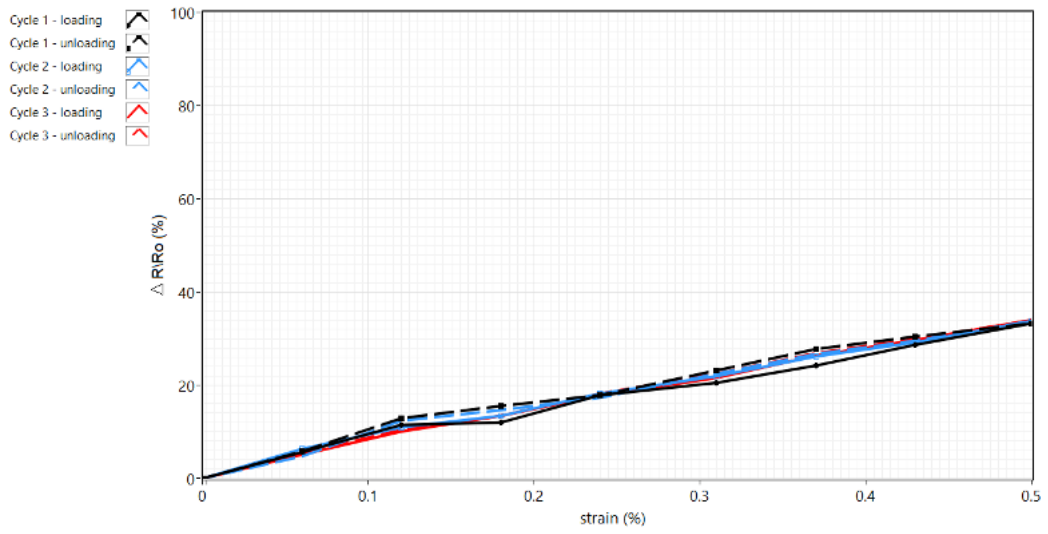


Figure B. 13: Three loading/unloading cycles of the sample (A100, B30, C10)

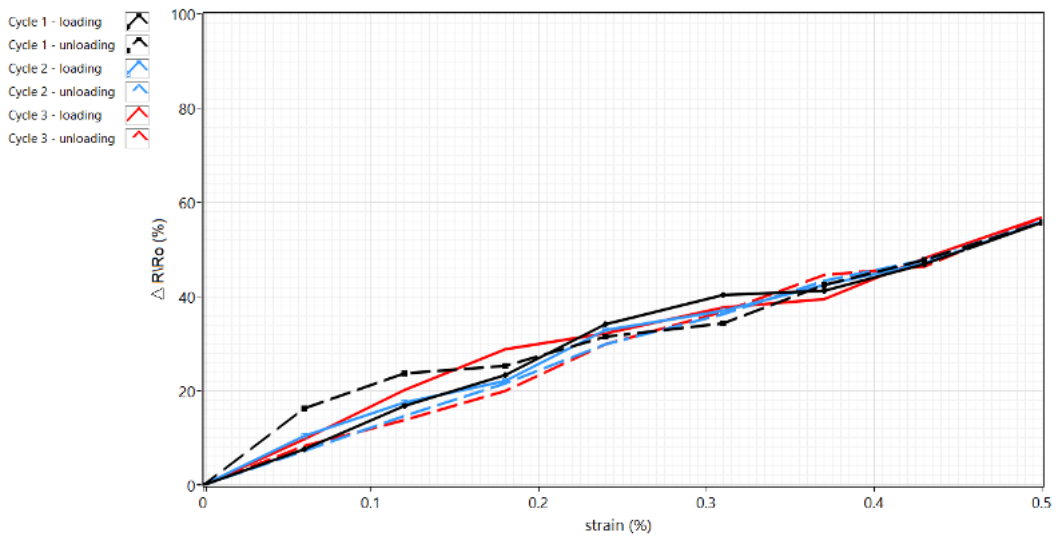


Figure B. 14: Three loading/unloading cycles of the sample (A100, B60, C_).

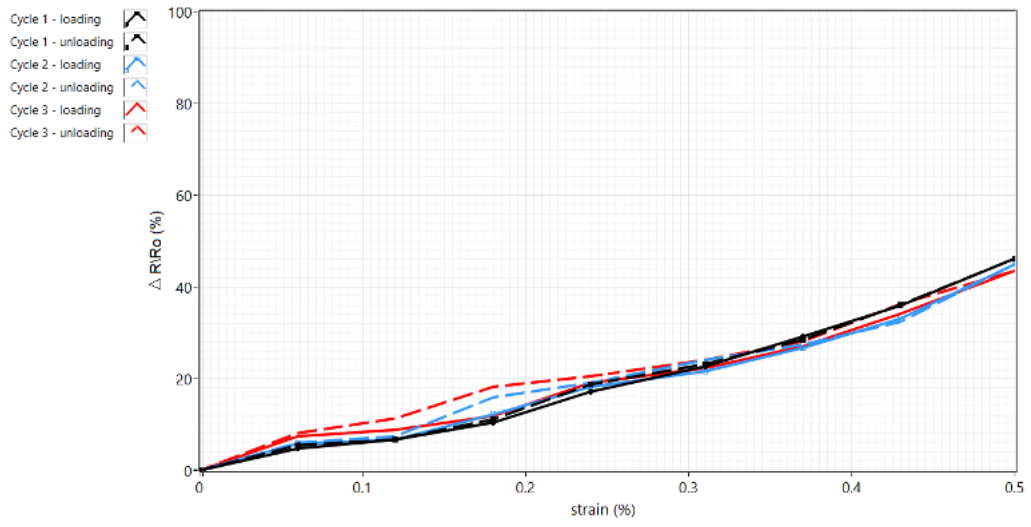


Figure B. 15: Three loading/unloading cycles of the sample (A100, B60, C5).

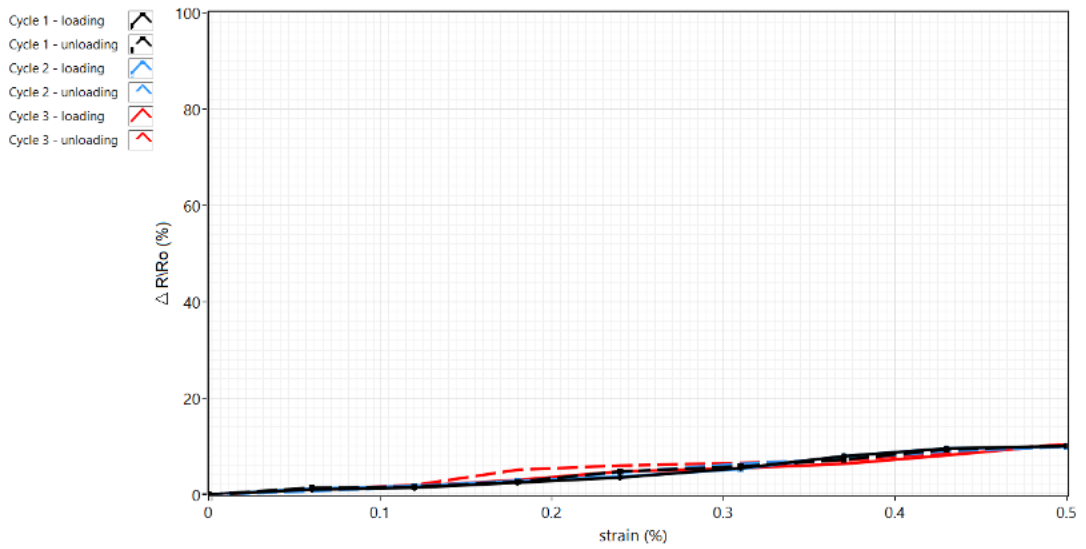


Figure B. 16: Three loading/unloading cycles of the sample (A100, B60, C10).

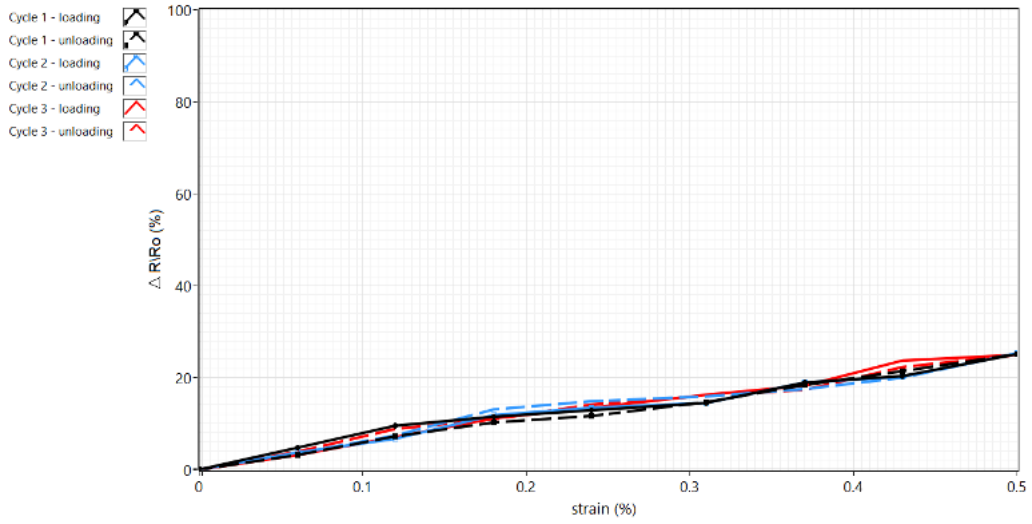


Figure B. 17: Three loading/unloading cycles of the sample (A200, B_, C_).

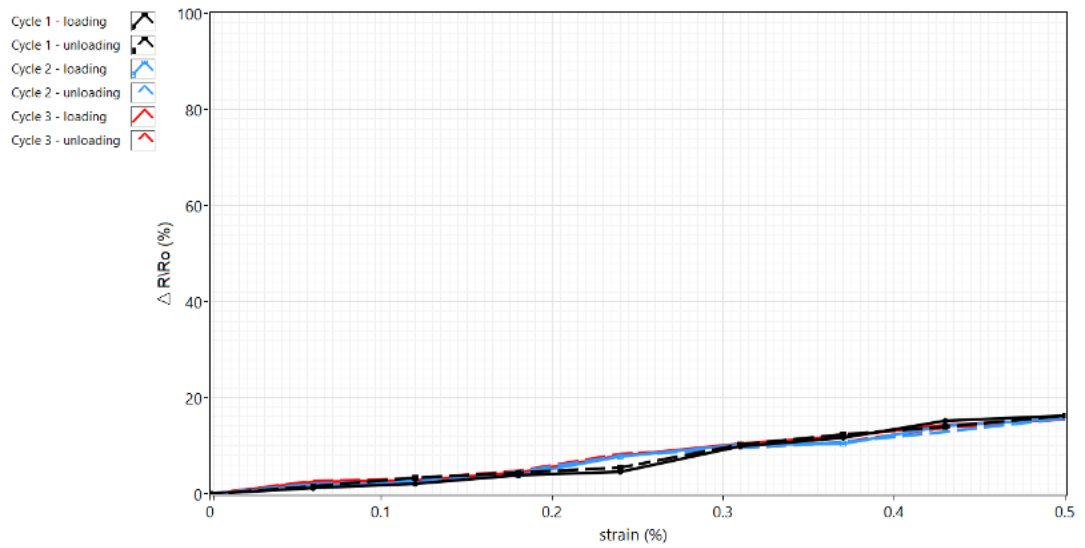


Figure B. 18: Three loading/unloading cycles of the sample (A200, B_, C5).

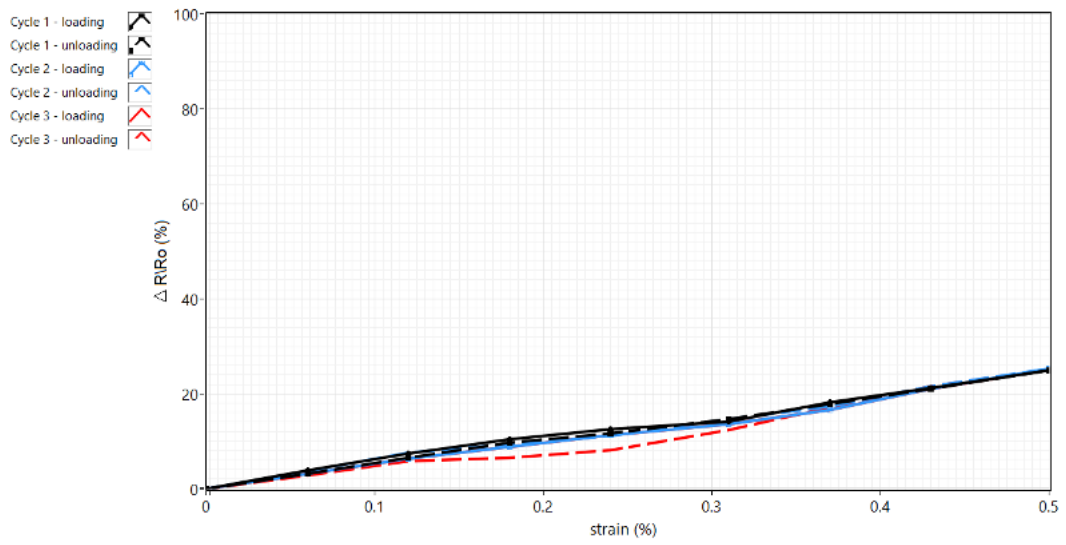


Figure B. 19: Three loading/unloading cycles of the sample (A200, B_, C10).

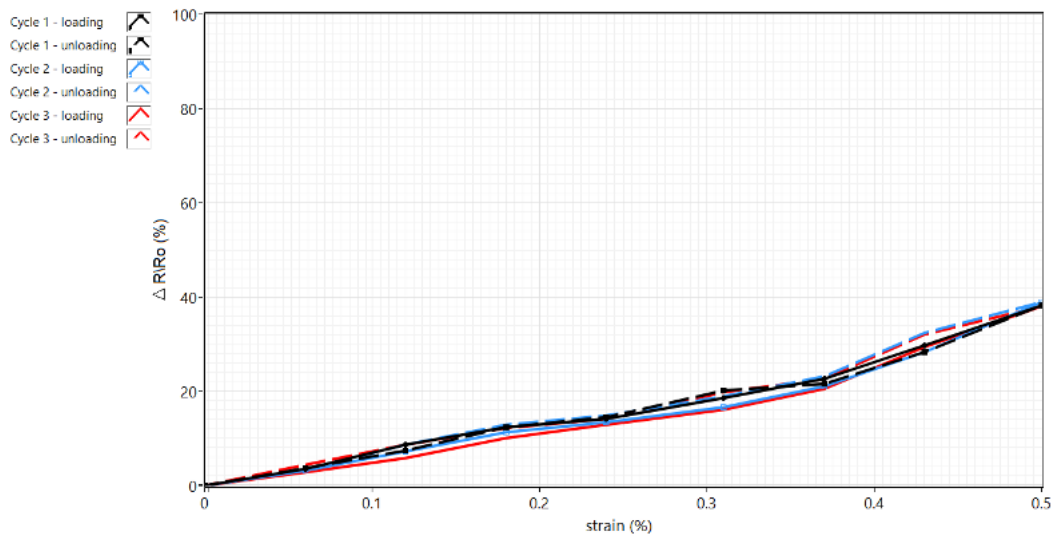


Figure B. 20: Three loading/unloading cycles of the sample (A200, B30, C_).

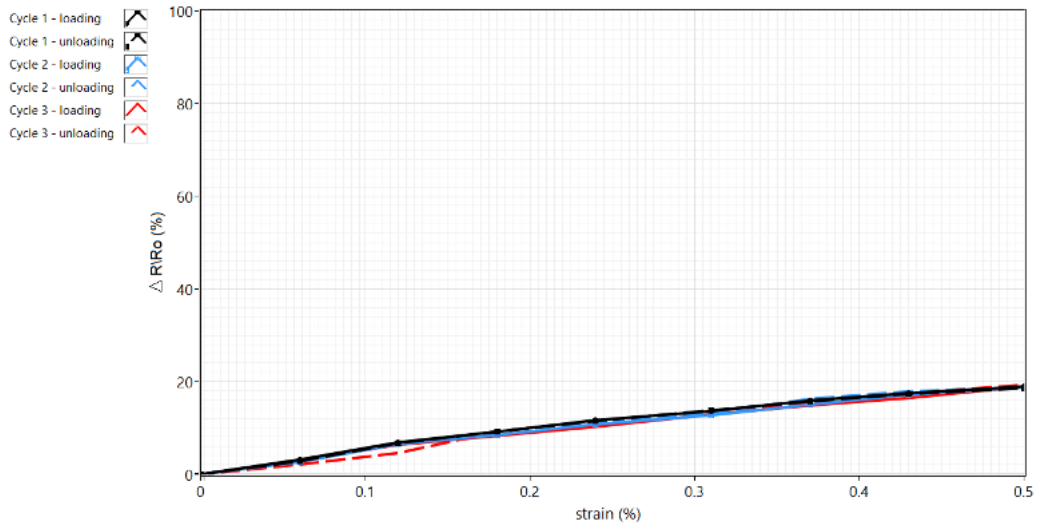


Figure B. 21: Three loading/unloading cycles of the sample (A200, B30, C5).

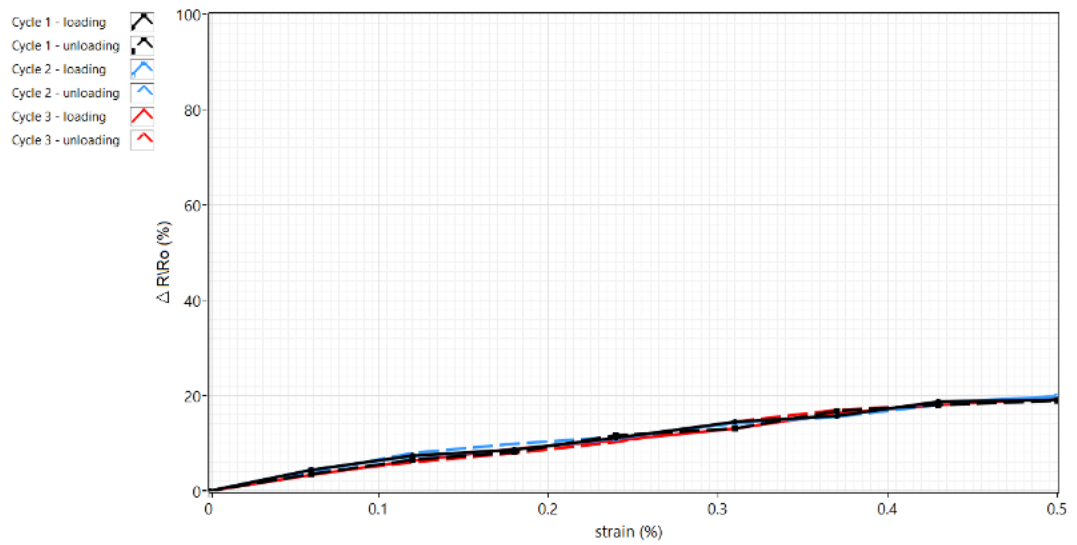


Figure B. 22: Three loading/unloading cycles of the sample (A200, B30, C10).

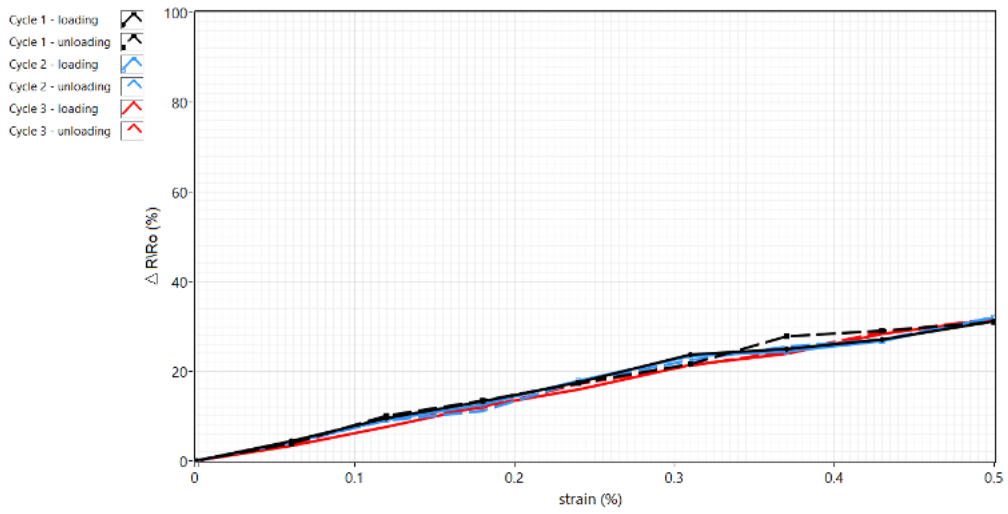


Figure B. 23: Three loading/unloading cycles of the sample (A200, B60, C_).

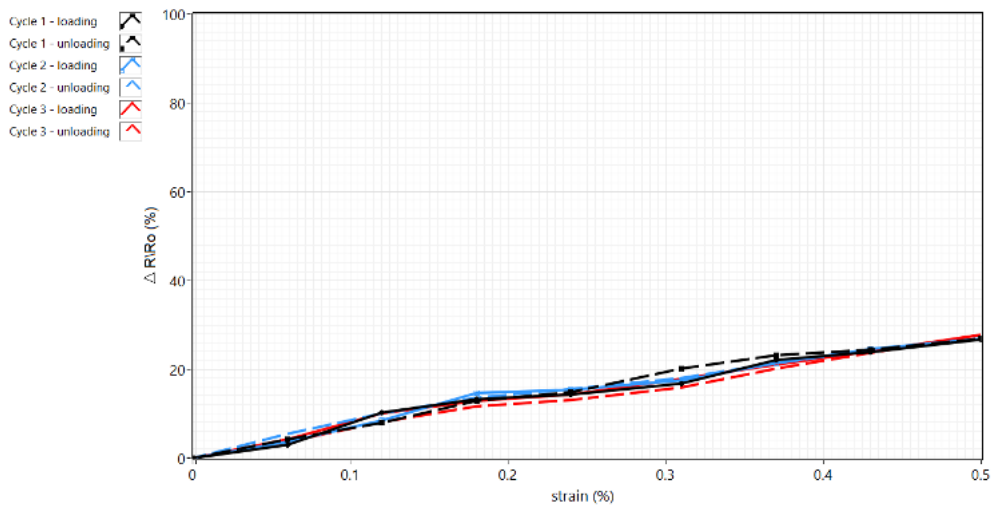


Figure B. 24: Three loading/unloading cycles of the sample (A200, B60, C5).

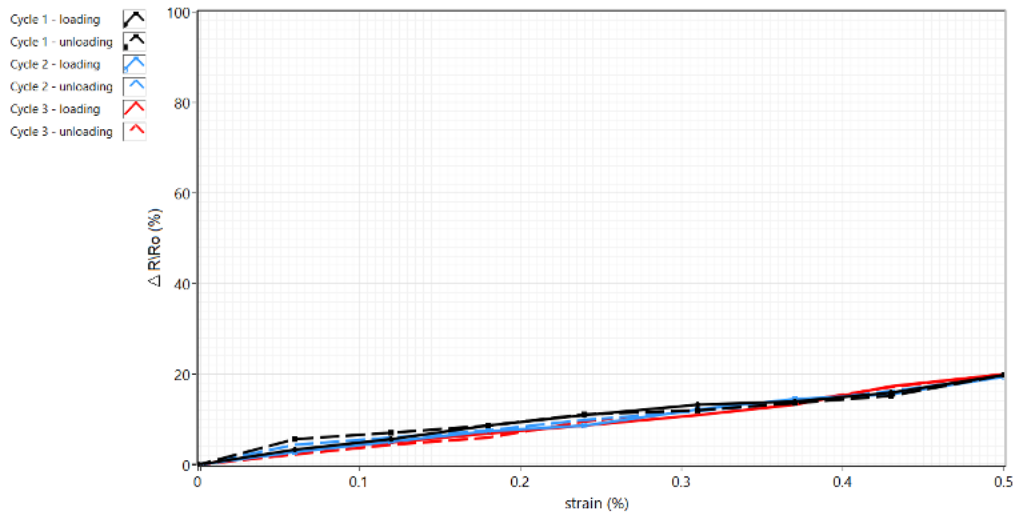


Figure B. 25: Three loading/unloading cycles of the sample (A200, B60, C10).

